Characterisation of semiconducting polymers and fabrication of OLEDs

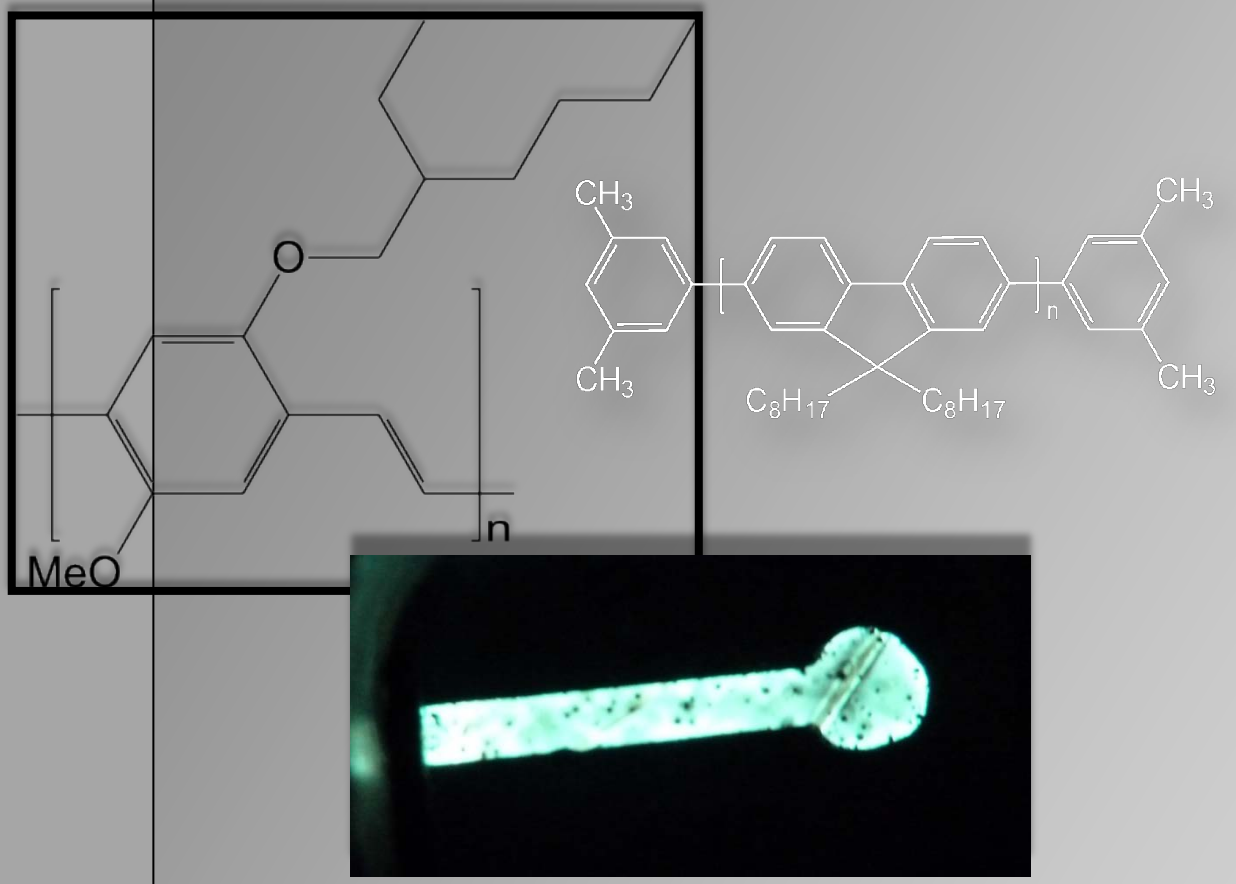

Master´s Thesis
Aalborg University 2012
Nanophysics and –materials
Morten Arnfeldt Hygum

AALBORG UNIVERSITY

Institute of Physics and Nanotechnology
Skjernvej 4A
9220 Aalborg E
Phone: +45 9940 9215
Fax: +45 9940 9235
http://www.nano.aau.dk

Title: Characterisation of semiconducting polymers and fabrication of OLEDs

Theme: Advanced nanotechnology

Project period
September 2st 2011 to June 14th 2012

Project group
5.219

Participant

Morten Arnfeldt Hygum

Supervisor
Kjeld Pedersen - Head of Department
at
Institute of Physics and Nanotechnology

Number printed: 5

Page count: 118 doublepaged

Synopsis:

The physics behind OLEDs are here explored and a DFT study of selected conjugated polymers is carried out, revealing a semiconducting nature of the polymers and low effective masses of the charge carriers.
It is also attempted to fabricate OLEDs of long lifetimes by a simple spincoating procedure but only a lifetime close to one hour has been achieved. The short lifetime is believed to be due to uneven layers in the OLEDs, as a result of the solvent used for the spincoating procedure.

Dansk synopsis

Denne kandidatafhandling behandler fysikken bag organiske lysdioder og endvidere er der udviklet en DFT model af udvalgte konjugerede polymerer. Denne model påviste, at polymererne er halvledende og gav anledning til lave effektive masser af ledningsbærerne.
I afhandlingen er det forsøgt at fabrikere organiske lysdioder med lang levetid ved hjælp af en simpel spincoating procedure. Dog lykkedes til kun at fabrikere en lysdiode med en levetid op imod en time. Den korte levetid forventes at være forårsaget af ujævne lag i lysdioden, hvilke er et resultat af det anvendte opløsningsmiddel til spincoating proceduren.

Preface

This master's thesis is written during the last year of the master's program Nanophysics and -materials at the Department of Physics and Nanotechnology at Aalborg University, running from September 2^{nd} 2011 to June 14^{th} 2012, amounting to 45 ECTS points. The subject of this project is *advanced nanotechnology*.
Part I contains the motivation for the subject of OLEDs plus the project goals. Part II presents the concept of conjugated polymers and a theoretical discussion about the OLED. Pat III regards all of the experimental work done during this project, the fabrication of OLEDs by the use of spincoating. The final concluding remarks and further perspectives are seen in Part IV.

I would like to thank the people who have helped me during this project.

- *Kim Houtved Jensen* and *Peter Kjær Kristensen* - for laboratory assistants.
- *Mads Lund Trolle*, *Mohtadin Hasemi* and *Christian Fisker* - for letting me do my calculations on their computers.
- *Jakob Bork* at Mekoprint A/S - for supplying various materials.

Contents

PART I

MOTIVATION

Introduction 1

The interest in organic electronics has increased substantially in recent years in both the academic and industrial society, due to a vast technological potential. The enormous attention to this field has, among other, been driven by the expectation to fabricate efficient, large-area, flexible displays and light sources, low-cost integrated circuits, and highly efficient low-cost plastic solar cells. One of the advantages of using organic light emitting diodes (OLEDs) in displays rather than e.g. liquid crystal displays (LCDs) is that OLEDs emit uniformly and require less power.

The field of polymer optoelectronics started in the 1970s where the first thin-film polymers were synthesised and the subsequent success in doping these polymers to create conducting polymers. In the early 1990s the field was established, when a synthesised phenyl-based polymer displayed electroluminescence under low operation voltage and in 2000 Alan J. Heeger, Alan G. MacDiarmid and Hideki Shirakawa were awarded the Nobel Prize in Chemistry for the discovery and development of conducting polymers.

It is the combination of their electronic, optical and mechanical properties that makes the conjugated polymers of such great interest[1]. The possibility of intrinsic processing by chemical modifications is also of interest, because one can then avoid disadvantages associated with doping, e.g. the enhanced screening of charge carriers by ionised impurities. This intrinsic processing is sometimes referred to as band gap tuning.

One of the difficulties of fabricating OLEDs is that contact materials with a low work function are needed, such as Ca or Mg, in order to get efficient devices. Therefore, it is of great importance to the keep the device clean and well-encapsulated because of the chemical instability of these low work function materials. As an example of this, the structure of the OLEDs Philips divested in 2009 is shown on figure 1.1. [Barford, 2005; Bruetting, 2006]

Though, organic electronics suffer from fabricational difficulties, companies like Sony and Samsung are still developing new technologies to fabricate displays and monitors ensuring a bright future for the OLED.

[1] Carbon-based conjugated polymers is characterised by valence π electrons that are delocalised along the polymer chain due to a general week interchain coupling.

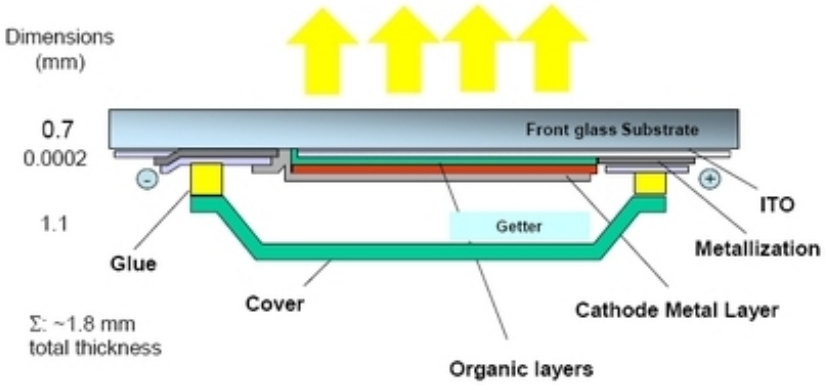

Figure 1.1: The structure of the OLEDs Philips divested in 2009. [Clausen, 2009]

1.1 Project goals

Throughout this project OLEDs will be fabricated, where the main interest will to make OLEDs with a long lifetime with the application as background light source. Furthermore, the polymers used for the fabrication of the OLEDs will be investigated theoretically in order to explain the given light emission spectra. This model will thus become a tool for band gap engineering of these conjugated polymers.

PART II

CHARACTERISATION OF SELECTED CONJUGATED POLYMERS AND THE ORGANIC LIGHT EMITTING DIODE

Conjugated polymers 2

A conjugated system is a compound that is covalently bound by alternating single and multiple bonds [Dewick, 2006]. Organic conjugated polymers are thus carbon-based macromolecules with delocalised valence electrons that dominate the electric and optical properties of the polymer [Barford, 2005]. For real polymers this conjugation length is often broken due to defects and it can be more convenient to describe the conjugation length as the average length between these defects. Furthermore, besides the example of an ideal linear polymer chain it is not always convenient to characterise the polymer size by the chain length but by the molecular weight[1].

2.1 Polyacetylene - The generic example

One of the simplest conjugated polymers is polyacetylene, which may take the *trans*- or *cis*-polyacetylene configuration, with the former being most thermodynamically stable [Su et al., 1979] and therefore the only one of interest here. The unit cell of both polymers is illustrated on figure 2.1.

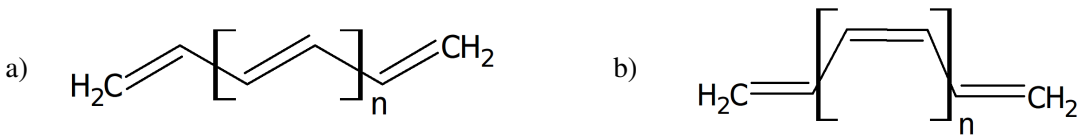

Figure 2.1: The unit cell of a) *trans*-polyacetylene (tPA) and b) *cis*-polyacetylene (cPA).

2.1.1 Electronic band structure

To evaluate the electronic dispersion of *trans*-polyacetylene (tPA) it is treated as an infinitely long planar molecule in the *xy* plane. The carbon atoms in organic conjugated polymers form the quite strong sp^2 hybridised bonds, whereas the fourth electron form the delocalised $2p_z$ symmetric π orbital, which is the main contributor to the optical and electrical properties of tPA. This sp^2 hybridisation is reviewed in appendix A. Because of the $2p_z$ symmetry the π orbitals only couple to other π orbitals, which enables a separate treatment of the π electrons. A detailed illustration of the bond lengths of the tPA chain is shown on figure 2.2.

Adapting the tight binding approach, reviewed in appendix B, the π states are expanded in a basis of

[1] Polymers can also have branched or network structures with an undefined length.

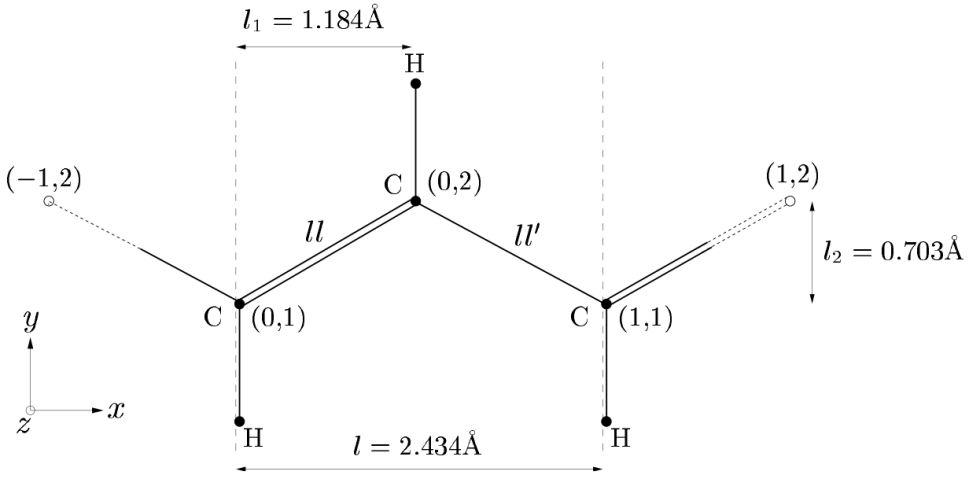

Figure 2.2: The (tPA) chain with the bond lengths $ll = 1.377$ Å and $ll = 1.434$ Å. The coordinate set (n, j) describes atom j in the n'th unit cell. [Lynge and Pedersen, 2003]

atomic $2p_z$ orbitals $\phi(\vec{r})$, leading to

$$\psi_{\vec{k},j}(\vec{r}) = N^{-1/2}\sum_{\vec{R}_j}^{N} e^{i(\vec{k}\cdot\vec{R}_j)}\phi_j(\vec{r}-\vec{R}_j), \quad j = 1,2,...,m \tag{2.1}$$

with $\vec{R}_j$ as the position vector for the j'th nucleus in the unit cell, N as the number unit cells and m is the number of atomic wave functions in the unit cell. The allowed states will thus be constructed by a linear combination of equation (2.1), which yields

$$\begin{aligned}\varphi_{\vec{k},n}(\vec{r}) &= \sum_{j}^{m} C_{n,j}\psi_{\vec{k},j}(\vec{r}) \\ &= C_{n,1}\psi_{\vec{k},1}(\vec{r}) + C_{n,2}\psi_{\vec{k},2}(\vec{r}).\end{aligned}$$

Restricting this analysis to orthogonal tight binding $\langle\varphi_n|\hat{H}|\varphi_{n'}\rangle = \delta_{n',n}$ and only consider the Hamiltonian matrix elements of nearest neighbours, then by setting the zero point energy to $\langle\varphi_n|\hat{H}|\varphi_n\rangle = 0$, the energy eigenvalue problem reads

$$\begin{bmatrix} -E(k) & e^{-ikl}\beta' + \beta \\ e^{ikl}\beta' + \beta & -E(k) \end{bmatrix} \cdot \begin{bmatrix} C_{n,1} \\ C_{n,2} \end{bmatrix} = \begin{bmatrix} 0 \\ 0 \end{bmatrix}, \tag{2.3}$$

where l is the lattice constant, β and β' are the Hamilton matrix elements along ll and ll', respectively. The non-trivial solution to equation (2.3) gives rise to

$$\begin{aligned} 0 &= \begin{vmatrix} -E(k) & e^{-ikl}\beta' + \beta \\ e^{ikl}\beta' + \beta & -E(k) \end{vmatrix} \\ &\Downarrow \\ E(k) &= \pm\sqrt{\beta^2 + \beta'^2 + 2\beta\beta'\cos(kl)}, \end{aligned}$$

where the negative solution denotes the bonding orbital and the positive solution denotes the anti-bonding. Hence, tPA is a semiconductor with a band gap of $E_g = 2|\beta - \beta'|$, which has been determined experimentally by photoelectron spectroscopy to E_g =1.8 eV, while the bandwith has been found to be 12.8 eV leading to β =-2.75 eV and β' =-3.65 eV[Heeger et al., 2010]. The π electron band structure can be seen on figure 2.3. [Lynge and Pedersen, 2003]

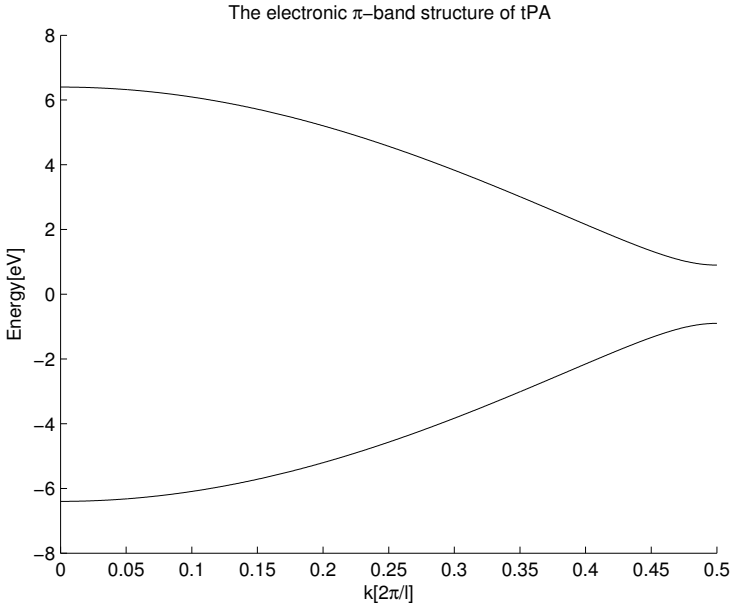

Figure 2.3: The π-band structure of tPA.

When estimating the electronic dispersions for polymers the infinite chain approximation might be too crude simply because the number of repeating unit cells can be small compared e.g. macro crystalline solids, all depending on which polymerisation technique that has been used to make the polymer. The number of repeating unit cells of commercial polymers usually span from 150 to 900. So in order to substantiate this approximation the energy eigenvalues of a finite tPA chain described by following $N \times N$ Hamiltonian matrix, are calculated:

$$\overleftrightarrow{H} = \begin{bmatrix} 0 & \beta & 0 & & \cdots & & 0 \\ \beta & 0 & \beta' & 0 & & & \\ 0 & \beta' & 0 & \beta & \ddots & & \vdots \\ & 0 & \beta & \ddots & \beta & 0 & \\ \vdots & & \ddots & \beta & 0 & \beta' & 0 \\ & & & 0 & \beta' & 0 & \beta \\ 0 & & \cdots & & 0 & \beta & 0 \end{bmatrix}.$$

Setting $N \leq 150$ yields the eigenvalues illustrated on figure 2.4a). A surface state whose energy lies in the band gap and a bulk state is illustrated on figure 2.4b). It is seen that the surface states emerges even

if no relaxation of the ends occurs. It is also noticed that the discrete states merge into a continuum of states giving rise to energy bands when the number of repeating unit cells increases, validating the infinitely long chain approximation for tPA chains longer than 150 repeating unit cells.

a) b)

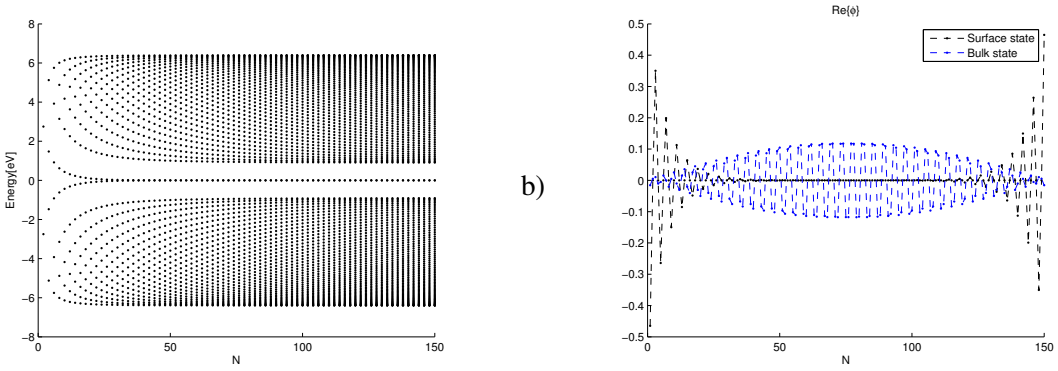

Figure 2.4: a) The energy eigenvalues of tPA chain versus the number of repeating unit cells., where the surface states are seen to lie in the band gap. b) A plot of a surface and a bulk state along the chain.

2.1.2 Solitons in tPA

The dimerised pattern of alternating single and double bonds gives rise to as degenerate ground state in tPA, which is achieved by interchange the double and single bonds. This degeneracy occasions a spinless conduction caused by so-called solitons[2].

A soliton, also referred to as a bond alternating defect or phase kink in the conjugation sequence, is a shift in the single and double bond alternation as illustrated on figure 2.5. The solitons are, due to the degenerate ground state of tPA, in principle free to move along the chain and thus enables photoconductivity. They also makes tPA non-luminescent because of an electronic state in the band gap, due to the structural distortion, as illustrated on figure 2.6, whereas the *cis*-configuration do display luminescent properties.

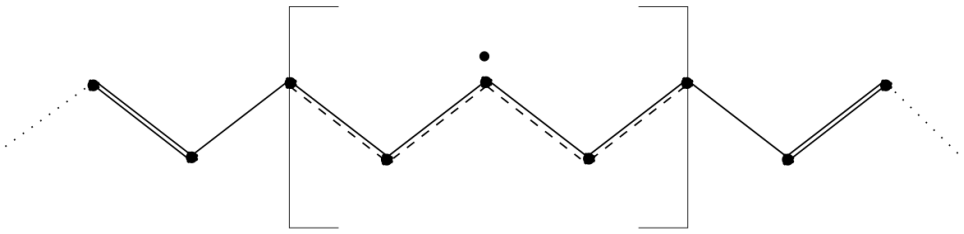

Figure 2.5: A neutral soliton in a tPA chain, where the dot marks the middle of the soliton and the brackets indicates the extents of the soliton, which in reality is about seven unit cells. [Lynge, 2004]

[2]The word solitons refers to localised travelling waves or wave packages, which do not change their shape.[Munteanu and Donescu, 2004]

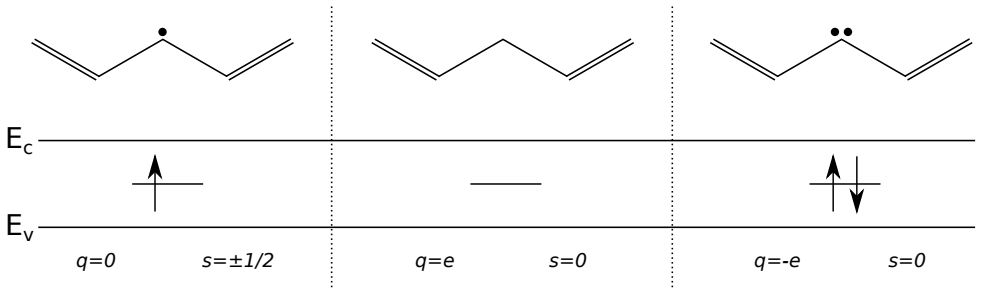

Figure 2.6: The occupation possibilities of a soliton level with q as the charge and s as the spin, whereas the dots here represent an amount of electrons.

[Yü, 1988; Barford, 2005]

2.2 Poly(para-phenylene)

Another example of a conjugated polymer is poly(para-phenylene) (PPP), which basically is a chain of benzene rings, but because this polymer is very hard to dissolve, side-groups can be added to the backbone of PPP giving rise to poly(9,9-di-n-octylfluorenyl-2,7-diyl) (PFO)[3]. The unit cells of PPP and PFO are shown on figure 2.7. This side-group addition changes the structural configuration of the polymer and therefore the electronic properties. To investigate these changes an ab initio density-functional theory model was created for both polymers. Density-functional theory (DFT) and a further theoretical foundation for the method used to solve the electronic problem is, here, presented in appendix C and D, respectively.

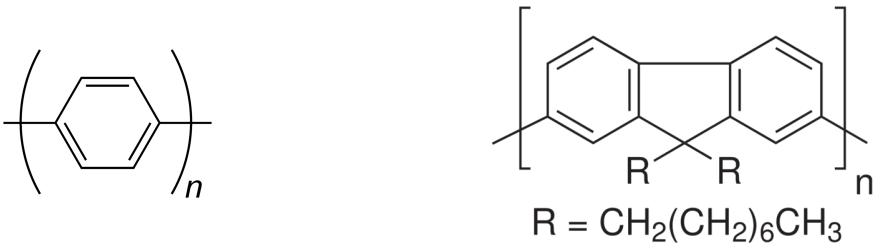

Figure 2.7: The unit cell of PPP (left) and PFO (right).

2.2.1 Electronic band structure

Since the side-group addition in PFO locks two benzene rings together the unit cell for PPP was set to contain two benzene rings. With the procedure presented in section E.1 in appendix E, the calculated structure of the unit cells for PPP and PFO are shown on figure 2.8 and 2.9, respectively, where the bond

[3]These modified polymers are also referred to as derivative polymers.

lengths along the backbones are labelled.

The side-group addition does not seem to affect the bond lengths much. It does, however, induce a

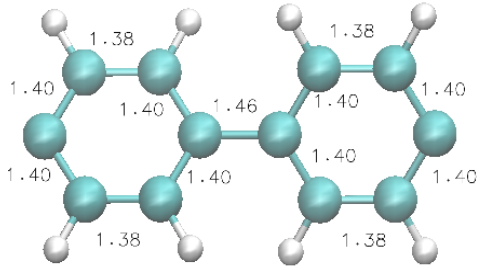

Figure 2.8: The calculated molecular structure of PPP. The lattice constant was found to be l=8.6 Å and the twisting angle between the planes formed by the benzene rings was found to be θ=26.23°. Blue balls are carbon and grey balls are hydrogen.

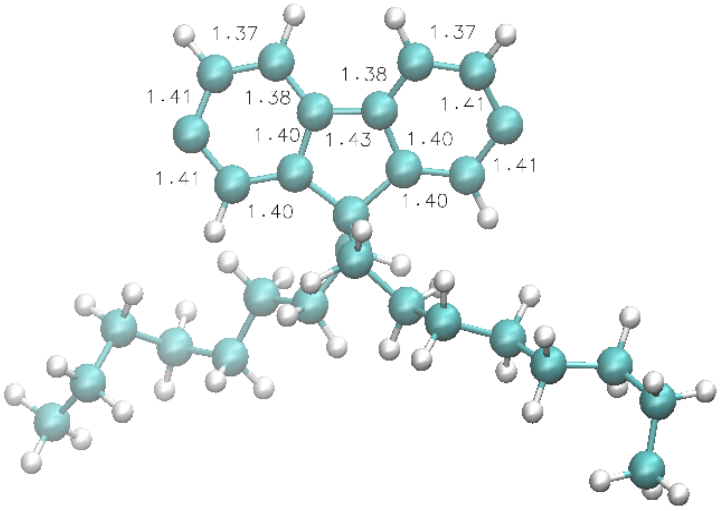

Figure 2.9: The calculated molecular structure of PFO. The lattice constant was found to be l=8.36 Å and the twisting angle between the planes formed by the benzene rings was found to be θ=34.37°.Blue balls are carbon and grey balls are hydrogen.

kink in the backbone at the bond between the two benzene rings and change the twisting angle between the rings. The kink also shortens the lattice constant from 8.6 Å at PPP to 8.36 Å at PFO. The lattice constant for PPP is similar to that found by De Carvalho et al. [2003]. With their similar approach they found a lattice constant of 8.62 Å. They also found an experimental value of 8.6 Å. No similar models could be found for PFO. Furthermore, Logdlund et al. [1993] showed that the energy gap relates to the torsion angle and that a larger torsion angle leads to a larger band gap.

Because of the heavy computational task of solving the electronic problem by e.g. the quite exact GW approximation, only the Kohn-Sham band structures are calculated and then shifted according to experimental values for the band gap. The Kohn-Sham band structure underestimates band gaps, but offers a reasonable estimate of the valence bands and also the curvature of the conduction bands. Despite the change in the torsion angle the observed band gaps of PPP and PFO are quite similar, 3.3 eV for PPP

[Yoder et al., 1999] and 3.4 eV for PFO [Lane et al., 2006].
The shifted Kohn-Sham band structure for PPP and PFO is shown on figure 2.10, obtained by the LDA approach, where the calculated band gaps are $E_{g,LDA} = 2.17$ eV for PPP and $E_{g,LDA} = 1.96$ eV for PFO. It appears that the structural change in the backbone does not change the electronic properties, significantly. Also the effective masses are found to be quite similar for both polymers. The effective mass[4] for a conduction electron was found to be $m_e = 0.021m_0$, for PPP and $m_e = 0.02m_0$ for PFO, where m_0 is the free electron mass. The effective mass for a hole in PPP was fond to be $m_h = 0.023m_0$ and $m_h = 0.02m_0$ in PFO. It is thus noticed that the conduction and valence bands are quite symmetric for both polymers and enables low effective masses.

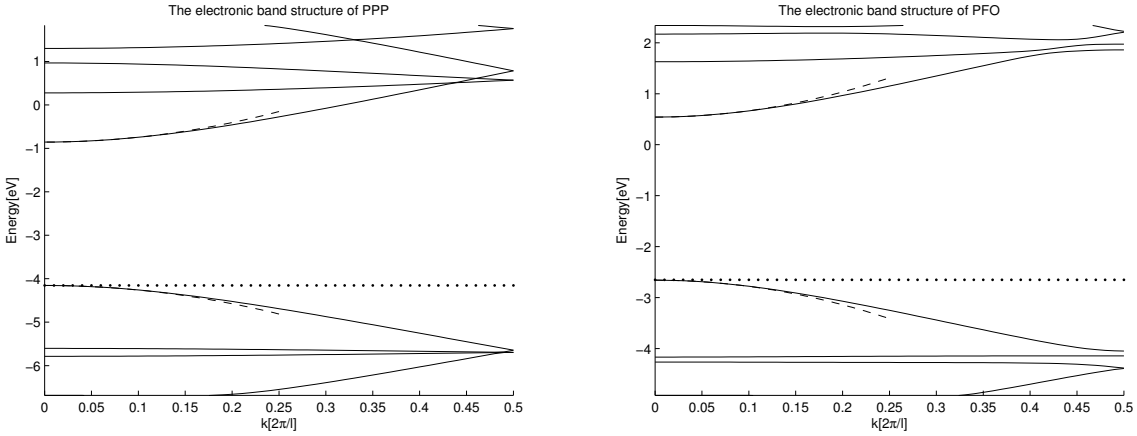

Figure 2.10: The electronic band structure of PPP (left) and PFO (right). The dotted horizontal lines represent the Fermi level, whereas the dashed lines are the polynomial fits of the conduction and valence bands for the determination of the effective masses.

One thing that has not been studied is the effect of excitons, which dominate the optical properties of conjugated polymers. Exciton binding energies of 0.4 eV for PPP is found [Knupfer, 2003] and 0.30 eV for PFO [Alvarado et al., 1998]. Hence, the emission and absorption spectra will be highly influenced by excitons.

2.3 Poly(para-phenylene vinylene)

A neat combination of PPP and PA is poly(para-phenylene vinylene) (PPV), which is a polymer consisting of a benzene ring and a carbon-carbon double bond, separated by a single bond. Again, because of the difficulties of dissolving PPV, a polymer with side-groups containing oxygen, is added to the benzene ring giving rise to poly[2-methoxy-5-(2-ethylhexyloxy)-1,4-phenylenevinylene] (MEH-PPV). The unit cells of PPV and MEH-PPV are shown on figure 2.11.

[4]The effective mass follows from considering the change in the momentum of the electron over time, for which is assumed that mass is constant: $\frac{d\vec{p}}{dt} = m^* \frac{d\vec{v}}{dt}$, where m^* is the effective mass and $\vec{v} = \nabla_{\vec{k}}\omega = \frac{1}{\hbar}\nabla_{\vec{k}}E$ is the velocity. With $\frac{\hbar}{m^*}\frac{d\vec{k}}{dt} = \frac{1}{\hbar} \cdot \frac{d}{dt}\nabla_{\vec{k}}E = \frac{1}{\hbar} \cdot \nabla^2_{\vec{k}}E\frac{d\vec{k}}{dt}$, one obtains the effective mass as $\frac{1}{m^*} = \frac{1}{\hbar^2}\nabla^2_{\vec{k}}E$. [Kittel, 2005]

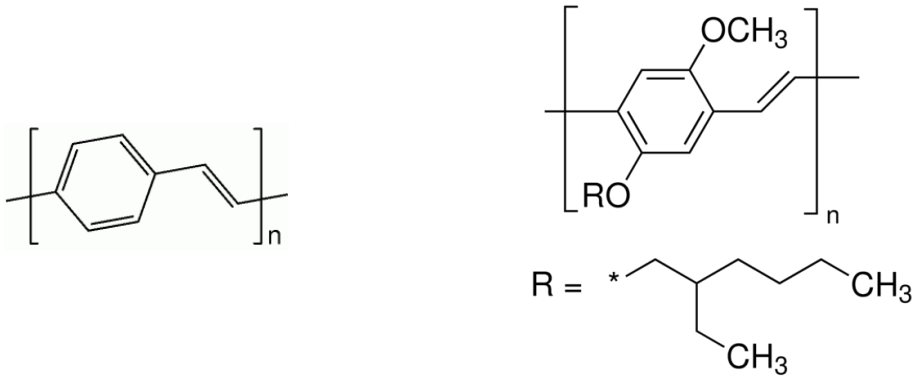

Figure 2.11: The unit cell of PPV (left) and MEH-PPV (right).

2.3.1 Electronic band structure

Though this side-group addition does not give rise to any structural change in the polymer, the oxygen is expected to change the electronic band structure, because it is more electronegative than carbon. With the procedure presented in section E.2 in appendix E the structure of the unit cells were calculated, where the unit cell for PPV is shown on figure 2.12 and the unit cell for MEH-PPV 2.13, both with labelled bond lengths in the backbone. No major difference in the backbones is seen with, very similar lattice constants l=6,62 Å for PPV and l=6,63 Å for MEH-PPV. The lattice constant for PPV is similar to that found by De Carvalho et al. [2003]. With a similar ab initio approach they found a lattice constant of 6.65 Å. They also found an experimental value of 6.54 Å. No similar models could be found for MEH-PPV.

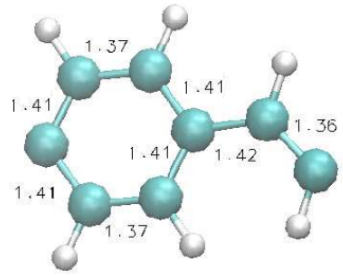

Figure 2.12: The calculated molecular structure of PPV. The lattice constant was found to be l=6,62 Å. Blue balls are carbon and grey balls are hydrogen.

A change in the band gap is observed, though. The band gap of PPV is 2.4 eV [Yoder et al., 1999] whereas for MEH-PPV it is 2.27 eV [Cernini et al., 1997]. The shifted Kohn-Sham band structure for PPV and MEH-PPV is shown on figure 2.14, obtained by the LDA approach, where the calculated band gaps are $E_{g,LDA} = 1.59$eV for PPV and $E_{g,LDA} = 0.99$eV for MEH-PPV. Furthermore, a slight change in the effective masses is also noticed. The effective mass for a conduction electron was found to be $m_e = 0.0117m_0$ for PPV and $m_e = 0.007m_0$ for MEH-PPV. The effective mass for a hole in PPV was fond to be $m_h = 0.0123m_0$ and $m_h = 0.0076m_0$ in MEH-PPV. Again, the first conduction band and highest valence band are quite symmetric for both polymers but the pull in the electrons from the added oxygen

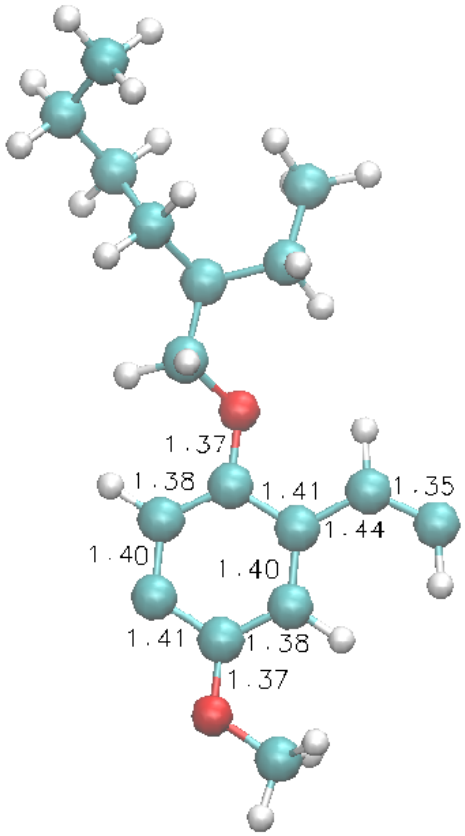

Figure 2.13: The calculated molecular structure of MEH-PPV. The lattice constant was found to be l=6,63 Å. Blue balls are carbon, red balls are oxygen and grey balls are hydrogen.

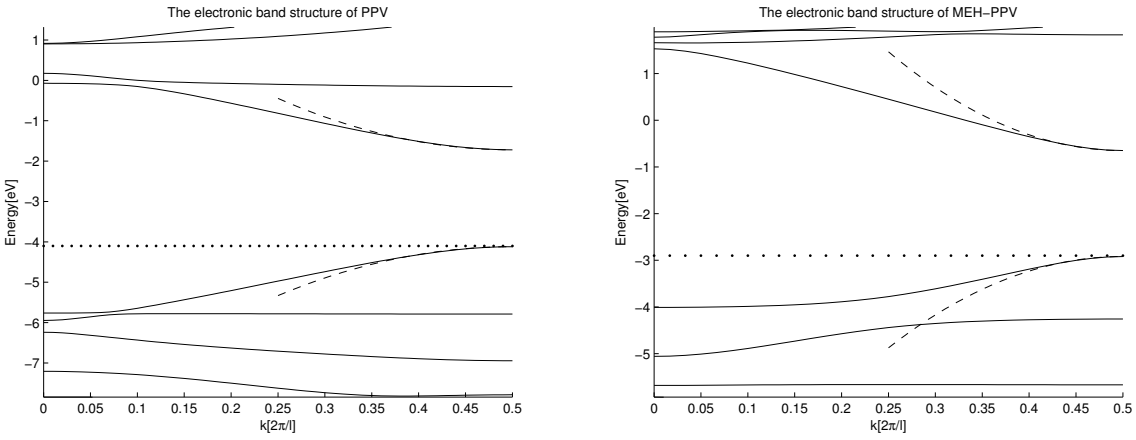

Figure 2.14: The electronic band structure of PPV (left) and MEH-PPV (right). The dotted horizontal lines represents the Fermi level, whereas the dashed lines are the polynomial fit of the of the conduction and valence bands for the determination of the effective masses for the charge carriers.

atom changes the electronic dispersion, giving rise to lower band gaps and effective masses. Finally, the excitonic effects are also changed quite a bit. The exciton binding energy for PPV has been observed to be as much as 1 eV [Chandross et al., 1994], where for MEH-PPV it is seen to be 0.35 eV [Alvarado et al., 1998] and still quite dominant for the optical properties.
From these analyses it appears that by adding side-groups, where the atoms connecting the side-groups to the backbone are more electronegative than the backbone atoms, one can red-shift the band gap and increase the charge carrier mobilities, if the side-group do not change the charge carrier scattering rate.

3 Physical properties of organic light emitting diodes

The structure of a light emitting diode (LED) is similar to the p-n junction diodes. Though, the essential part of LEDs is that they are not in thermal equilibrium. In an organic light emitting diode (OLED) the light emitting substrate is organic, hence the name. Whereas the light emitting properties at conventional LED originates from the junction of oppositely doped regions, the OLED is made by the use of intrinsic semiconducting polymers. The light emitting and rectifying properties are thus due to asymmetric work functions of the contacts.

The organic substrate, usually a layer of conjugated polymer with a thickness of about 100 nm, is sandwiched between an anode with a high work function, usually an indium tin oxide (ITO) substrate, and a cathode with a relatively low work function, such as Al, Mg or Ca. Electrons will then be injected from the cathode and recombine with electron holes injected from anode, emitting light. These single layer devices, however, are very inefficient because a lot of the current generates heat instead of light. In order to optimise these devices, the emitting layer can be sandwiched between a so-called hole blocking layer (HBL) or electron transporting layer at the cathode and an electron blocking layer (EBL) or a hole transporting layer by the anode, in order to equalise the charge balance. This structure is illustrated on figure 3.1.

Besides enhancing the efficiency of the OLED the transporting layers also offers chemical stability and some control over the position of the recombination zone, which for obvious reasons is wanted in the emitting layer. Due to a generally low charge carrier mobility in organic solids the recombination zone is usually located at one of the contacts, depending on which mobility is the limiting. This is not to favour because the emitted light will easier be quenched by the contacts. [Hadziioannou and Malliaras, 2007]

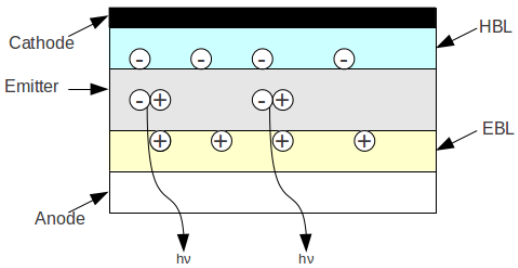

Figure 3.1: The structure of an OLED with an electron blocking layer (EBL) and a hole blocking layer (HBL).

3.1 Charge injection

Among the most essential processes in the OLED is the charge injection, which can be understood by the electronic band structure of the electroluminescent polymer and the contacts.
The energy band gab of the polymer is obtained by subtracting the energy required to remove an electron from the highest occupied state/molecular orbital (HOMO) to the vacuum level, also referred to as the ionisation potential, with the energy gained by adding an electron from vacuum to the lowest unoccupied state/molecular orbital (LUMO), the so-called electron affinity. Hence, to inject electrons from the cathode, the contact must be able to inject electrons to the lowest unoccupied state in the polymer, and likewise, the anode must be able to accept electrons from the highest occupied state. The asymmetric requirements to the work functions of the contacts will then lead to built-in potentials in the device, which form different Schottky barriers when in contact with the polymer, due to charge migration between the two materials caused by the different Fermi levels. These built-in potentials and energy barriers highly determine the electronic characteristics of the OLED. A schematic of the electronic energy diagrams of a single layer device in thermal equilibrium is shown on figure 3.2a), while the electronic energy diagrams of a single layer device with an applied forward bias equal to the built-in potential is shown on figure 3.2b).
The emission of light then happens, when an injected electron recombines with an injected hole, where

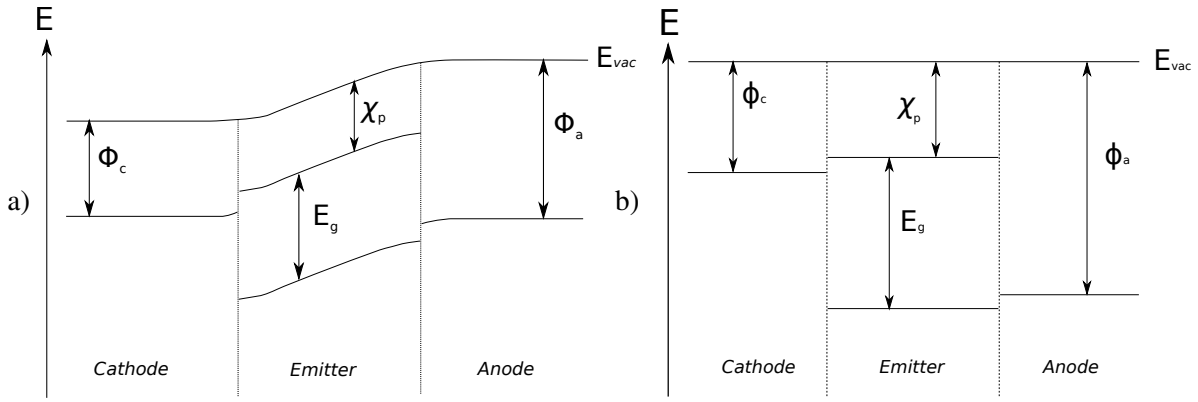

Figure 3.2: The energy levels of a single layers OLED a) in thermal equilibrium and b) with an applied forward bias equal to the built-in potential. Φ_c is the work function of the cathode, Φ_a is the work function of the anode, E_g is the band gap for the organic polymer and χ_p as the electron affinity of the polymer.

the barriers these charge carriers must overcome, by assuming no surface states that might pin the Fermi level, will then be given as

$$\begin{aligned} \Delta E_h &= I_p - \Phi_a = E_g + \chi_p - \Phi_a \\ \Delta E_e &= \Phi_c - \chi_p, \end{aligned}$$

where ΔE_h is the energy barrier for the hole, ΔE_e is the energy barrier for the electron, E_g is the band gap of the polymer, I_p is the ionisation potential of the polymer, χ_p is the electron affinity of the polymer, Φ_c is the work function of the cathode and Φ_a is the work function of the anode. If the anode is ITO, the barrier for the holes is quite small, but if the metal contacts block the charge carrier transport, the charges must overcome the barriers either by thermal emission governed by the Richardson equation, which holds for applied electric fields smaller than $5 \cdot 10^5 \frac{V}{m}$ [Kristensen, 2008], or through field emission governed by the Fowler-Nordheim model, which holds for applied electric fields larger than $5 \cdot 10^5 \frac{V}{m}$ [Kristensen, 2008], explained later in section 3.1.1 and section 3.1.2, respectively.
Chen and Meng [2002] found effective mobilities as high as $10^{-3} \frac{m^2}{Vs}$ for electric fields above $4 \cdot 10^7 \frac{V}{m}$ in conjugated systems. Furthermore, they discovered that structural and chemical defects in conjugated systems does not confine the charge carriers effectively, leaving the interchain charge hopping and the charge injection from the contacts as the limiting factors of the charge carrier transport.
If the lowering of the potential energy barrier, due to an electric field, is comparable with the barrier height itself and thus neglecting the tunnelling problematic and neglecting a possible continuum of unbound states into which the charge carriers can be emitted to, an alternative approach for prediction of current flow through the metal/semiconductor junction can be made. However, data fitting of the Richardson equation has been proven to be a quite successful approach.
[Hadziioannou and Malliaras, 2007]

3.1.1 Thermal emission

After the metal has made contact to the polymer, charge will diffuse between the semiconductor and the metal until the Fermi levels of the two materials equalise. It is assumed that the Fermi level of the semiconducting polymer is higher than the metal, hence electrons will diffuse from the polymer to the metal until the unbalanced charge distribution creates an electric field large enough with direction opposite to the electron migration the electron diffusion is stopped. This approach can easily be applied for the case, where the Fermi level of the semiconductor is lower than the metal.
For evaluation of the current after thermal equilibrium is established the metal/semiconductor interface is placed at $x = 0$, the metal at $x < 0$ and the semiconductor at $x > 0$, thus a current density from the semiconductor to the metal can be written as

$$j_{sm,x} = \frac{-2e}{\Omega} \sum_{\vec{k}} -v_x f(E_{\vec{k}}),$$

where e is the elementary charge, Ω is the volume, $-v_x$ is the velocity component of the electrons from the semiconductor towards the metal and $f(E_{\vec{k}})$ is the Fermi distribution, which can be approximated to a Boltzmann distribution if $E_{\vec{k}} - E_f \gg k_B T$, with E_f as the Fermi level or quasi-Fermi level, T is the temperature and k_B is the Boltzmann constant.
Assuming spherical parabolic electron energy dispersions in the semiconductor, the effective mass ap-

proximation enables the conduction band energy to be written as

$$E_{\vec{k}} = E_c + \frac{\hbar^2 k^2}{2m^*}, \tag{3.3}$$

where E_c is the bottom of the conduction band, m^* is the effective mass, $\hbar$ is the reduced Planck constant and $\vec{k}$ is the wavevector. The group velocity in the x-direction of a wave package at E_c is then

$$v_x = \frac{1}{\hbar}\frac{\partial E_{\vec{k}}}{\partial k_x} = \frac{\hbar k_x}{m^*}. \tag{3.4}$$

Combining equation (3.3) and (3.4) and converting the sum over $\vec{k}$ as $\sum_{\vec{k}} \to \frac{\Omega}{(2\pi)^3}\int d^3k$ yields

$$j_{sm,x} = \frac{\hbar e}{4\pi^3 m^*}\int k_x \mathrm{e}^{\frac{E_f - E_c - \frac{\hbar^2 k^2}{2m^*}}{k_B T}} d^3k.$$

Presuming, that $-\infty \leq k_{y,z} \leq \infty$ and that the restriction of k_x is given by the kinetic energy in the x-direction, which must be large enough to overcome the energy barrier $\Phi_m - \Phi_s = \frac{\hbar^2 k_{x0}^2}{2m^*} = \Delta$, where Φ_s is the work function of the semiconductor, $j_{sm,x}$ will be given as

$$\begin{aligned} j_{sm,x} =& \frac{e k_B T}{2\pi^2\hbar}\mathrm{e}^{\frac{E_f - E_c}{k_B T}}\int_{k_{x0}}^{\infty}\mathrm{e}^{\frac{-\frac{\hbar^2 k^2}{2m^*}}{k_B T}} k_x dk_x \\ =& \frac{e m^* (k_B T)^2}{2\pi^2\hbar^3}\mathrm{e}^{\frac{E_f - E_c - \Phi_m - \Phi_s}{k_B T}}. \end{aligned} \tag{3.5}$$

Utilising $\Phi_s = \chi_s + (E_c - E_f)$ equation (3.5) is rewritten to the Richardson equation:

$$j_{sm,x} = j_{th}\mathrm{e}^{\frac{\chi_s - \Phi_m}{k_B T}}, \quad j_{th} = \frac{e m^* (k_B T)^2}{2\pi^2\hbar^3}, \tag{3.6}$$

where j_{th} is referred to as the thermal current coefficient. Equation (3.6) can be modified to hold for an applied forward bias $V_a > 0$, if the size V_a is not too large. This is due to the screening of free electrons in the metal. Because of these free electrons it can be assumed that there will be no band bending in the metal and therefore no change in the energy barrier in that direction. The barrier the electrons will have to overcome will, by assuming a constant electric field in the semiconductor, thus be given as

$$\begin{aligned} V(x) &= V_0 - eV_a = \Phi_m - \chi_s - eV_a \\ &= V_0 - eFx = \Phi_m - \chi_s - eFx, \end{aligned}$$

where F is the amplitude of the local electric field in the semiconductor right after the junction and V_0 is the barrier height. Hence, when applying a forward bias equation (3.6) takes the form

$$j_{sm,x} = j_{th}\mathrm{e}^{\frac{\chi_s - \Phi_m + eV_a}{k_B T}}.$$

Another phenomenon, known as the image charge effect, can contribute to energy barrier lowering in the presence of an electric field. An electron at a distance x from the metal will induce a positive charge on the metal surface. Thereby, a force of attraction between the electron and the induced positive charge will emerge, equivalent to that of an electron and a positive charge placed at $-x$.[1] This image force is given by

$$F_{image,x} = \frac{-e^2}{4\pi\varepsilon_0\varepsilon(2x)^2} = \frac{-e^2}{16\pi\varepsilon_0\varepsilon x^2}. \tag{3.7}$$

where ε is the relative dielectric constant of the semiconductor. The work done to an electron transferred from infinity to the point x is thus found by integrating equation (3.7) from infinity to x giving rise to the modified barrier

$$V(x) = V_0(x) - eFx = \Phi_m - \chi_s - \frac{e^2}{16\pi\varepsilon_0\varepsilon x} - eFx.$$

The lowering of the energy barrier due to the image charge force ΔV_0 and the location of the lowering x_m are found by setting $\frac{dV}{dx} = 0$. Thus,

$$x_m = \sqrt{\frac{e^2}{16\pi\varepsilon_0\varepsilon F}}$$

and

$$\Delta V_0 = \sqrt{\frac{e^3 F}{16\pi\varepsilon_0\varepsilon}}.$$

Hence,

$$j_{sm,x} = j_{th}\mathrm{e}^{\frac{\chi_s - \Phi_m + \sqrt{\frac{e^3F}{16\pi\varepsilon_0\varepsilon}} + eV_a}{k_B T}}.$$

It should be noted that even without any applied bias the electric field is not zero due to the built-in potential. Typical values for the image force are in the range of 10^5V/cm leading to x_m in the order of 5 nm. The image charge effect thus lowers the energy barrier a bit and therefore enables charge emission at lower applied bias. A plot of the thermal electron emission, with and without the image charge effect, as a function of applied bias through a barrier, where V_0 =1 eV, at room temperature, with an electric field strength of $F = \frac{1V}{200\text{Å}}$ and a mass of $m = 0.2m_0$ is shown on figure 3.3.
[Balkanski and Wallis, 1992; Sze and Ng, 2007]

3.1.2 Field emission

Besides a thermal emission, where the electrons can overcome a potential barrier by the means of thermal energy, a current through the metal/semiconductor junction can be obtained by applying an electric field that is sufficiently large for electrons near the Fermi level to tunnel through the energy barrier.
Adapting the same assumptions for the junction as for thermal emission the current density, due to an

[1] This amounts to letting the relative dielectric constant of the metal go toward infinity, $\varepsilon_m \to \infty$

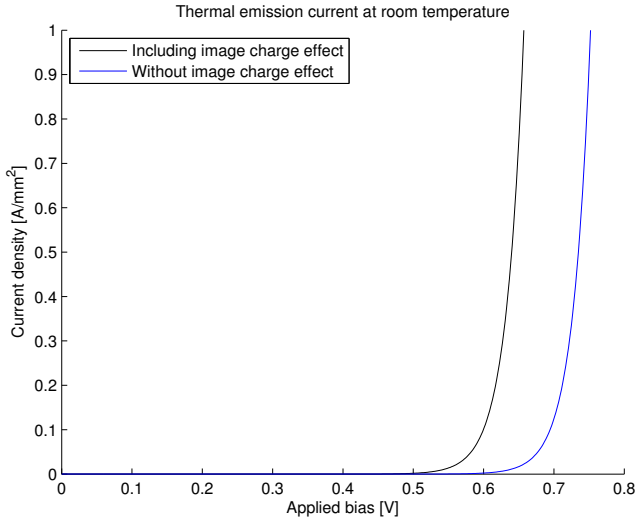

Figure 3.3: The thermal emission current as a function applied bias with a barrier height of 1 eV and a mass of 20 per cent of the free electron mass.

electric field is

$$J = \frac{2e}{(2\pi)^3} \int f(E_{\vec{k}}) T(E) v_x d^3k, \tag{3.8}$$

where $T(E)$ is the transmission probability of an electron through an assumed triangular barrier with the energy E. This assumption originates from the simple geometry of the junction and an assumed constant electric field in the semiconductor. Thus, by neglecting any image charge effects, the barrier is given by

$$V(x) = V_0 - eFx, \tag{3.9}$$

with V_0 as the barrier height. To evaluate the tunnelling probability the WKB approximation can be applied. Dividing the potential barrier into sufficiently small rectangular pieces gives rise to

$$T_{WKB}(E) = \mathrm{e}^{-2\sqrt{\frac{2m^*}{\hbar}} \int_{x_1}^{x_2} \sqrt{V(x)-E}dx}, \tag{3.10}$$

where $x_{1,2}$ are the endpoints of the potential barrier with the solutions of $V(x_{1,2}) - E = 0$[2]. This triangular potential barrier is illustrated on figure 3.4. Inserting equation (3.9) into (3.10) leads to

$$\begin{aligned} T_{WKB}(E) &= \mathrm{e}^{-2\sqrt{\frac{2m^*}{\hbar^2}} \int_0^{\frac{V_0-E}{eF}} \sqrt{V_0-eFx-E}dx} \\ &= \mathrm{e}^{-\sqrt{\frac{2m^*}{\hbar^2}} \frac{4}{3eF} (V_0-E)^{3/2}}. \end{aligned}$$

Another, more exact approach to evaluate the transmission probability is to divide this system into three regions, as indicated on figure 3.4. Now, consider an electron moving from left to right. The wave

[2]It can be noted, that within the WKB approximation the probability of reflection at each little barrier is neglected.

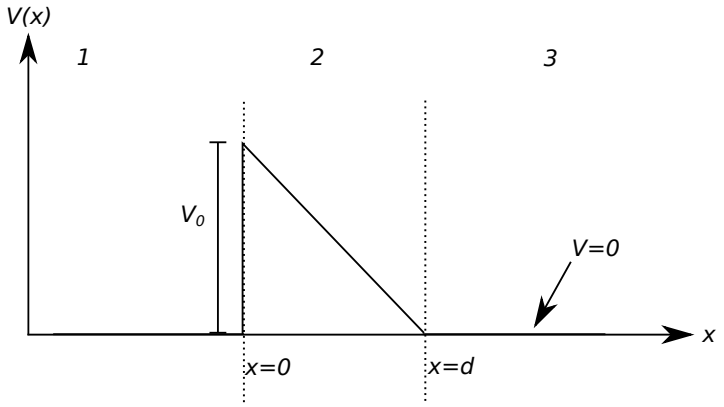

Figure 3.4: The potential energy barrier for a triangular barrier.

function for region 1 is

$$\psi_1(x) = \mathrm{e}^{ikx} + r\mathrm{e}^{-ikx}, \qquad k = \sqrt{\frac{2m^*}{\hbar^2}E_x},$$

where r is the reflection coefficient for the barrier. For region 3

$$\psi_3(x) = t\mathrm{e}^{ikx}, \qquad k = \sqrt{\frac{2m^*}{\hbar^2}E_x},$$

with t as the transmission coefficient.
For region 2, where the same mass is assumed[3], the Schrödinger equation reads

$$\begin{aligned} -\frac{\hbar^2}{2m^*}\frac{d^2\psi_2(x)}{dx^2} + (V_0 - Fx)\psi_2(x) &= E_x\psi_2(x) \\ &\Downarrow \\ \frac{d^2\psi_2(x)}{dx^2} = \frac{2m^*}{\hbar^2}(V_0 - Fx - E_x)\psi_2(x) &= \frac{2m^*F}{\hbar^2}\left(\frac{V_0 - E_x}{F} - x\right)\psi_2(x) = \frac{2m^*F}{\hbar^2}(x_0 - x)\psi_2(x), \end{aligned} \tag{3.12}$$

with $x_0 = \frac{V_0 - E_x}{F}$. By introducing $q = \left(\frac{2mF}{\hbar}\right)^{1/3}$ equation (3.12) is rewritten to Airy's equation[4] as follows

$$\frac{d^2\psi_2(x)}{dx^2} = q(x_0 - x)\psi_2(x),$$

where it can be shown, that $\psi_2 = \mathrm{A}\cdot\ \mathrm{Ai}(q(x_0 - x)) + \mathrm{B}\cdot\mathrm{Bi}(q(x_0 - x))$. Matching the wave functions and the derivatives of the wave functions at the boundaries $x = 0$ and $x = d$ combined with the Wronskian

[3]The analysis can easily be applied for different masses at the different regions. This just has to be taken into account when matching the wave functions and the derivatives of the wave functions at the boundaries.

[4]The Airy's equation is on the form $y''(z) - zy = 0$. Here $y = \mathrm{A}\cdot\ \mathrm{Ai}(q(x_0 - x)) + \mathrm{B}\cdot\mathrm{Bi}(q(x_0 - x))$. Introducing $z = p(x_0 - x)$ while applying the chain-rule yields $\frac{d^2y}{dz^2} = \frac{1}{p^2}\frac{d^2y}{dx^2}$. Thus $\frac{d^2y}{dx^2} = p^3(x_0 - x)y$.

being $W[\text{Ai,Bi}] = 1/\pi$, the coefficients A, B, r and t can be determined. This leads to

$$t = \frac{2ka/\pi}{(ika+qa')(k\tilde{b}+iq\tilde{b}') - (ikb+qb')(k\tilde{a}+iq\tilde{a}')},$$

where the $'$s denotes a differentiation with respect to x and $a = \text{Ai}(qx_0)$, $a' = \text{Ai}'(qx_0)$, $\tilde{a} = \text{Ai}(q(x_0-d))$, $\tilde{a}' = \text{Ai}'(q(x_0-d))$, $b = \text{Bi}(qx_0)$, $b' = \text{Bi}'(qx_0)$, $\tilde{b} = \text{Bi}(q(x_0-d))$ and $\tilde{b}' = \text{Bi}'(q(x_0-d))$.
The exact transmittance, the transmission coefficient squared, and WKB-approximation are plotted on figure 3.5 with $V_0 = 1\text{eV}$ and $F = \frac{1V}{200\text{Å}}$ as a function of energy. It is seen, that the WKB-approximation is fairly accurate where tunnelling is not very probable and will be applied here, because it allows the integral in equation (3.8) to be done analytically.

Simplifying things further by restricting this analysis for energies close to the Fermi level of the metal

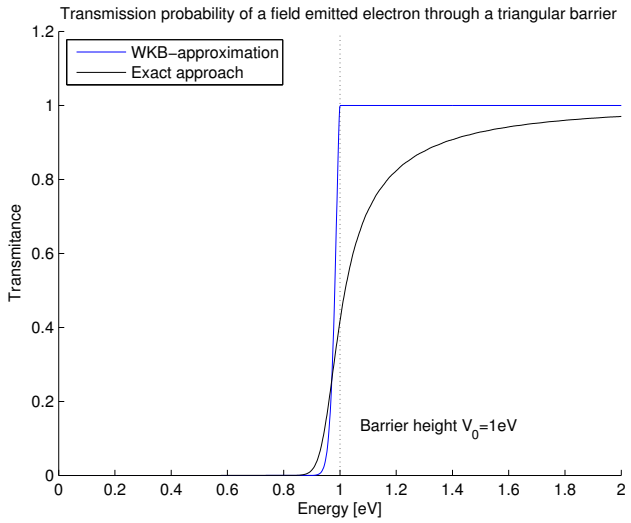

Figure 3.5: The transmittance as a function of energy of an electron tunnelling through the triangular barrier illustrated on figure 3.4 using the WKB-approximation and the exact approach.

allows the following Taylor expansion:

$$(E_c - E)^{3/2} \approx (E_c - E_f)^{3/2} - \frac{3(E_x - E_f)(E_c - E_f)^{1/2}}{2},$$

where E_c is the conduction band in the semiconductor. This gives rise to

$$T(E) = \mathrm{e}^{-\frac{4(\Phi_m-\chi_s)^{3/2}}{3eF}\sqrt{\frac{2m^*}{\hbar^2}}\,\mathrm{e}\sqrt{\frac{2m^*}{\hbar^2}}\frac{2\sqrt{(\Phi_m-\chi_s)}}{eF}(E-E_f)}.$$

To evaluate the integral in equation (3.8) the temperature is set to $T = 0K$, which then simplifies the expression to

$$J_{FN} = \frac{2e}{(2\pi)^3}\int_0^{\frac{\sqrt{2m^*E_f}}{\hbar}} T(E)\frac{\hbar k_x}{m^*}d^3k$$

$$= \frac{e}{16\pi^2\hbar(\Phi_m - \chi_s)} F^2 \mathrm{e}^{-\frac{4\sqrt{2m^*}(\Phi_m-\chi_s)^{3/2}}{3\hbar eF}}.$$

Including the image charges effect, reducing the effective potential barrier, equation (3.9) will be modified to

$$V(x) = V_0 - eFx - \frac{e^2}{16\pi\varepsilon\varepsilon_0 x},$$

where ε is the relative dielectric constant for the semiconductor. This yields the following transmission probability

$$T(E) = \mathrm{e}^{-\frac{4(\Phi_m-\chi_s)^{3/2}}{3eF}\sqrt{\frac{2m^*}{\hbar^2}}v(y)} \mathrm{e}^{\sqrt{\frac{2m^*}{\hbar^2}}\frac{2\sqrt{(\Phi_m-\chi_s)}t(y)}{eF}(E-E_f)},$$

where the functions $v(y)$ and $t(y)$ are related to elliptical functions from which y corresponds to the relative decrease of the potential barrier due to the image charge potential. The functions can be approximated to $t(y) \approx 1.049$ and $v(y) \approx 0.96 - y^2$, with

$$y = \frac{\Delta V_0(F)}{V_0} = \sqrt{\frac{e^3F}{4\pi\varepsilon\varepsilon_0}}\frac{1}{V_0}.$$

The modified Fowler-Nordheim tunneling current thus yields

$$J_{FN} = \frac{e}{16\pi^2\hbar(\Phi_m - \chi_s)t^2(y)} F^2 \mathrm{e}^{-\frac{4\sqrt{2m^*}v(y)(\Phi_m-\chi_s)^{3/2}}{3\hbar eF}}.$$

The modified and non-modified Fowler-Nordheim currents are both plotted on figure 3.6, with $V_0 = 1\mathrm{eV}$ and a mass of $m = 0.2m_0$ with m_0 as the free electron mass.

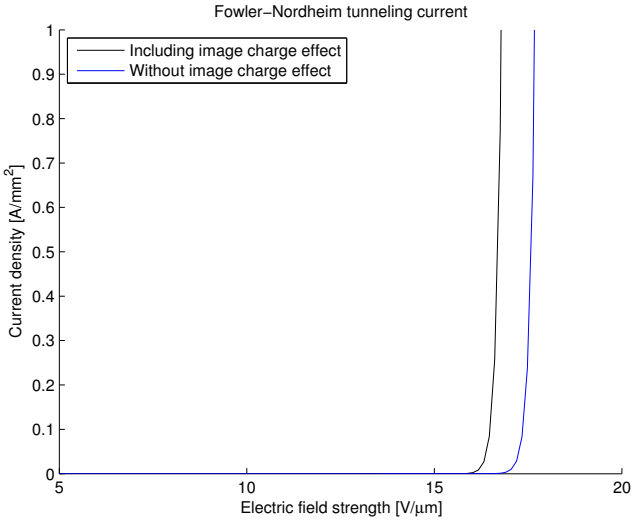

Figure 3.6: The modified and non-modified Fowler-Nordheim tunneling currents as a function of electric field strength with $V_0 = 1\mathrm{eV}$ and a mass of 20 per cent of the free electron mass.

[Loiseau, 2006; Pedersen and Diekhöner, 2011]

3.2 Trap and space charge limited transport

To investigate the charge carrier transport properties of OLEDs a one-carrier type device is first considered followed by a discussion of two-carrier devices.

3.2.1 One-carrier currents

As a starting point to this investigation it is assumed that the thermal spread in velocity profile of the emitted electrons can be neglected, combined with a flat potential minimum and a vanishing electric field at the contact. Again it is also assumed that the contact has infinitely many charge carriers for injection.
It has been shown by Malliaras and Scott [1999], that if the barrier height of the injected charge carrier is smaller than 0.3 eV the contact resistance is practically ohmic, so considering an electron current for the steady-state case with an ohmic contact resistance, and neglecting the diffusion contribution, the constant current is given as

$$J = e\mu nF, \tag{3.14}$$

where μ is the mobility of the electrons due to the electric field F and n is the concentration of conduction electrons. For a trap-free intrinsic semiconductor the Poisson equation, when placing the interface in the yz plane at $x = 0$, reads:

$$\frac{dF}{dx} = \frac{en}{\varepsilon_0\varepsilon}. \tag{3.15}$$

Substituting equation (3.14) into (3.15) yields

$$F\frac{dF}{dx} = \frac{J}{\varepsilon_0\varepsilon\mu}, \tag{3.16}$$

where the boundary condition $F(0) = 0$ is being applied. Separation of the variables thus gives rise to

$$\int_0^F F dF = \frac{J}{\varepsilon_0\varepsilon\mu}\int_0^x dx \quad \Rightarrow \quad F = \sqrt{\frac{2J}{\varepsilon_0\varepsilon\mu}x}.$$

The applied bias V_a can then be found to be

$$\int_0^L F dF = \sqrt{\frac{J}{\varepsilon_0\varepsilon\mu}}\int_0^L x^{1/2}dx \quad \Rightarrow \quad V_a = \frac{2}{3}\sqrt{\frac{2J}{\varepsilon_0\varepsilon\mu}}L^{3/2},$$

where L is the length of the semiconductor. The space-charge limited current-voltage characteristics can then be obtained:

$$J_{SCL} = \frac{9}{8}\varepsilon_0\varepsilon\mu\frac{V^2}{L^3}. \tag{3.17}$$

Equation (3.17) is also known as the Mott-Gurney square law or Child's law for solids. A perfect trap-free semiconductor is, however, a quite ideal case, so by taking electronic trap-state into account a more precise description of the current can be obtained.
The presence of electron traps will greatly reduce the current through the semiconductor at low injection energies, because most of these traps will initially be empty and thus capture the injected charge carriers and immobilise them. The concentration of filled electron traps at thermal equilibrium of the energy E_t is

$$\begin{aligned} n_{t,0} &= \frac{N_t}{1+(1/g)\mathrm{e}^{\frac{E_t-E_{f,i}}{k_BT}}} \\ &= \frac{N_t}{1+(1/g)(N/n_0)}, \qquad N = N_c\mathrm{e}^{\frac{E_t-E_c}{k_BT}}, \end{aligned} \tag{3.18}$$

where N_t is the concentration of traps, g is the degeneracy factor for the traps, $E_{f,i}$ is the intrinsic Fermi level and n_0 is the concentration of free conduction electrons in thermal equilibrium. If an electric field of moderate strength is applied, the balance between the free and trapped electrons is only changed by the injection of free electrons. Hence

$$n = n_i + n_0 = N_c\mathrm{e}^{\frac{E_f(x)-E_c(x)}{k_BT}}, \tag{3.19}$$

where n_i is the average excess concentration of injected free electrons. It is again noted that E_f in equation (3.19) is the quasi-Fermi level, whereas in equation (3.18) it is the intrinsic Fermi level. Keeping this terminology the concentration of the trapped electrons is given as

$$n_t = n_{t,i} + n_{t,0} = \frac{N_t}{1+(1/g)(N/n)},$$

where $n_{t,i}$ is the average excess concentration of injected trapped electrons.
Traps are usually divided into shallow or deep traps, where only shallow traps will be discussed. A shallow trap is characterised by an energy level E_t that lies above E_f and vice versa for deep traps. For shallow traps $(E_t - E_f)/k_BT \gg 1$. Hence,

$$\frac{n}{n_t} \approx \frac{N}{gN_t} = \frac{N_c}{gN_t}\mathrm{e}^{\frac{E_f-E_c}{k_BT}} \equiv \theta, \tag{3.20}$$

where it is noted that the constant θ is independent of injection level, as long as the traps are shallow. Utilising equation (3.20) Poisson's equation now reads

$$\frac{\varepsilon_0\varepsilon}{e}\frac{dF}{dx} = (n-n_0) + (n_t - n_{t,0}) = \left(\frac{1}{\theta}+1\right)(n-n_0) \approx 1/\theta(n-n_0), \tag{3.21}$$

which gives rise to the shallow-trap square law:

$$J = \frac{9}{8}\theta\varepsilon_0\varepsilon\mu\frac{V^2}{L^3}. \tag{3.22}$$

Equation (3.22) also holds if there are several sets of shallow traps of different energy levels. Then the j'th set of traps corresponding to the smallest θ_j will be used in equation (3.21) and (3.22).
[Lampert and Mark, 1970]

3.2.2 Two-carrier currents

Because the injected electrons and holes largely neutralise each other a two-carrier injection current will be larger than either of the one-carrier currents. Loss of charge carriers through recombination must be taken into account, where the net capture rates for the electrons and holes by each set of recombination centers must be equal for steady-state and if it is assumed that, as a starting point, trapping is not a limiting factor then changes in occupancy of recombination centers will be of no concern. At least it is of interest to only have radiative recombination, which mostly happens across the band gap.
Taken a similar approach as for the one-carrier currents, where the lifetime of the holes and electrons is set equal, denoted τ and assuming that most of the charge carrier is due to injection, hence $n \approx p \gg p_0, n_0$, where p is the concentration of holes, enables the Poisson equation as follows:

$$\frac{\varepsilon_0\varepsilon}{e}\frac{dF}{dx} = n - p = n_0 - p_0, \tag{3.23}$$

where the last part on the right-hand side states the assumption, that the injected charge carriers concentration is equal everywhere. The continuity equation for each charge carrier reads

$$\frac{1}{e}\frac{dJ_n}{dx} = \mu_n\frac{d}{dx}nF = n/\tau = p/\tau \tag{3.24}$$

and

$$-\frac{1}{e}\frac{dJ_p}{dx} = \mu_p\frac{d}{dx}pF = p/\tau = n/\tau. \tag{3.25}$$

From equation (3.24) and (3.25) it follows, that

$$J = J_n + J_p = e(b+1)\mu_p nF = \text{constant}, \qquad b = \mu_n/\mu_p.$$

Setting the hole-injection contact at $x = 0$ and electron-injection contact at $x = L$, where the electric field is taken to be $F = 0$ at the minority-carrier injection set to be $x = 0$, since only one boundary condition is needed in order to solve equation (3.23). Combining equation (3.25) with equation (3.24) and utilising

the last part of equation (3.23) gives rise to

$$F\frac{dF}{dx} = \frac{J}{e(n_0 - p_0)\mu_n\mu_p\tau},$$

which is quite similar to equation (3.16). The current density for two-carrier currents thus yields

$$J = \frac{9}{8}e(n_0 - p_0)\mu_n\mu_p\tau\frac{V^2}{L^3}.$$

Like for the one-carrier case a trap-limited current can be introduced by the factor θ. Hence

$$J = \frac{9}{8}\theta e(n_0 - p_0)\mu_n\mu_p\tau\frac{V^2}{L^3}.$$

[Lampert and Mark, 1970]

3.3 Luminescence

As mentioned the light emission of a LED is due to the recombination of a conduction electron with a hole and if the electron and hole couple to each other, the recombination of an exciton. The minimum photon energy is the energy gap and in the case of an exciton, the energy gap subtracted the binding energy of the exciton. However, neglecting excitons and selection rules of the relaxation process and if it is assumed that the probability of a radiative emission is independent of the initial and final energy of the electron, a quite simple model can be set up to obtain a qualitative emission spectrum of a given LED.
Setting the energy of an electron in the valence band to E, then the initial energy of the electron before emission of a photon must be $E + \hbar\omega$, where $\hbar\omega$ is the energy of the emitted photon. The amount of emitted photons is proportional to the number of recombined electron-hole pairs, hence the intensity $I(\omega)$ can be written as

$$I(\omega) \propto \hbar\omega \int_{U_c - \hbar\omega}^{U_v} p(E)n(E + \hbar\omega)dE, \qquad \text{with} \quad E \leq U_v$$

where U_c and U_v is the conduction and valence band, respectively, n is the concentration of conduction electron and p is the concentration of holes both in the interval dE.
These charge carrier concentrations can be found from the convolution of the Fermi function for the charge carrier and the density of states for the given charge carrier. At the LED regime, the position of the chemical potential μ_e for the conduction electrons ensures that $\frac{E+\hbar\omega-\mu_e}{k_B T} \gg 1$, enabling the Fermi function to be approximated to a Boltzmann distribution. Hence, for the charge carrier concentrations

yields

$$\begin{aligned} n(E+\hbar\omega) &\approx N_c\sqrt{E+\hbar\omega-U_c}\,\mathrm{e}^{-\frac{E+\hbar\omega-\mu_e}{k_BT}}, \\ p(E) &\approx N_v\sqrt{U_v-E}\,\mathrm{e}^{-\frac{\mu_h-E}{k_BT}}, \end{aligned}$$

where N_v is the effective density of states for the valence band, μ_h is the chemical potential both for the holes, N_c is the effective density of states for the conduction band and μ_e is the chemical potential both for the conduction electrons. Thus,

$$\begin{aligned} I(\omega) &\propto \hbar\omega\mathrm{e}^{-\frac{\hbar\omega}{k_BT}}\int_{U_c-\hbar\omega}^{U_v} p(E)\sqrt{U_v-E}\sqrt{E+\hbar\omega-U_c}dE \\ &= \frac{\hbar\omega\mathrm{e}^{-\frac{\hbar\omega}{k_BT}}\pi(\hbar\omega-E_g)^2\theta(\hbar\omega-E_g)}{8}, \end{aligned} \tag{3.28}$$

with $\theta(\hbar\omega-E_g)$ as a step function. Equation (3.28) is plotted on figure 3.7 with $k_BT = 25\text{meV}$.

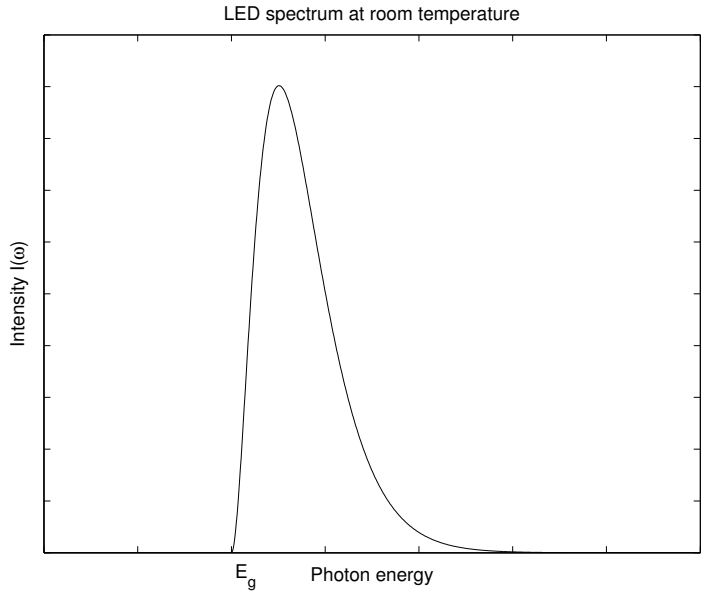

Figure 3.7: A LED spectrum versus photon energy $\hbar\omega$ with $k_BT = 25\text{meV}$.

[Pedersen and Diekhöner, 2011]

3.3.1 Decay types and pathways

Since the model presented above gives a quite qualitative description of the LED emission, a more detailed discussion of the excitation and recombination process in the organic molecule is needed.
For any recombination to occur an electron and a hole must be within a capture range of each other, often

assumed to be the Coulombic radius found by equating the thermal energy and the Coulomb potential:

$$r_c = \frac{e^2}{4\pi\varepsilon\varepsilon_0 k_B T}, \tag{3.29}$$

with ε as the dielectric constant for the polymer. A classical way of treating the carrier recombination is by the notion of the recombination time, which represents a combination of the carrier motion denoted τ_m, i.e. the time for the carriers to get within the capture radius, and the actual annihilation time of the carriers, denoted τ_c. The recombination time is thus $\tau_{rec}^{-1} = \tau_c^{-1} + \tau_m^{-1}$, which give rise to Langevin and Thomson recombination defined for $\tau_c \ll \tau_m$ and $\tau_c \gg \tau_m$, respectively. Due to a generally low carrier mobility in organic semiconductors the Langevin recombination is favoured.

The Pauli exclusion principle predicts that radiative decays will be from singlet to singlet states, though not all singlet decays will emit light, which is why e.g. photoluminescence will never be 100% efficient. Triplet to singlet decays are also possible through the process known as intersystem-crossing e.g. through spin-orbit coupling. This is a forbidden transition and therefore is associated with extremely long lifetimes[5]. The electronic energy of a triplet state is usually lower than the singlet state due to the exchange interaction between two parallel spins increases the distance between the electrons, leading to a lower Coloumb repulsion.

Most optical transitions occurs from the relaxed lowest excited singlet state due to a rapid internal conversion within this singlet manifold with respect to the rate of radiative decays and ionisation processes from other higher excited singlet states. An excitation of the molecule will be followed by a rapid vibrational relaxation to the vibrational ground state of the first excited singlet state below. This is known as Kasha's rule. The molecule can then deexcite radiatively or non-radiatively. Because the radiative decays usually ends up in a vibrational state, the fluorescent spectrum will be red-shifted with respect to the excitation spectrum. This is referred to as a Stokes shift. These excitation and relaxation processes are illustrated on figure 3.8. If both carriers are free, simple spin statistics dictates that the probability of forming a singlet state is $1/4$ and $3/4$ for triplet states.

The quantum efficiency φ_i is denoted as ratio of radiative decays k_r and the total decay rate. Thus

$$\varphi_i = \frac{k_r}{k_r + k_{nr}},$$

where k_{nr} is the non-radiative decay rate. It is of interest to achieve high quantum efficiencies but a lot of different phenomena can contribute the non-radiative decays. Furthermore, it is desired to have high electroluminescence quantum efficiencies, which is independent of temperature and electric field.

The deposition techniques used to fabricate OLED inevitably leads to either amorphous or polycrystalline emitting layers and is therefore a native complication. Defects, but also metal-polymer interfaces, can lead to non-radiative decays through e.g. traps or surface states. Therefore, it is of great importance, that

[5] In the order of miliseconds, whereas the lifetime of allowed radiative decays is in the order of nanoseconds.

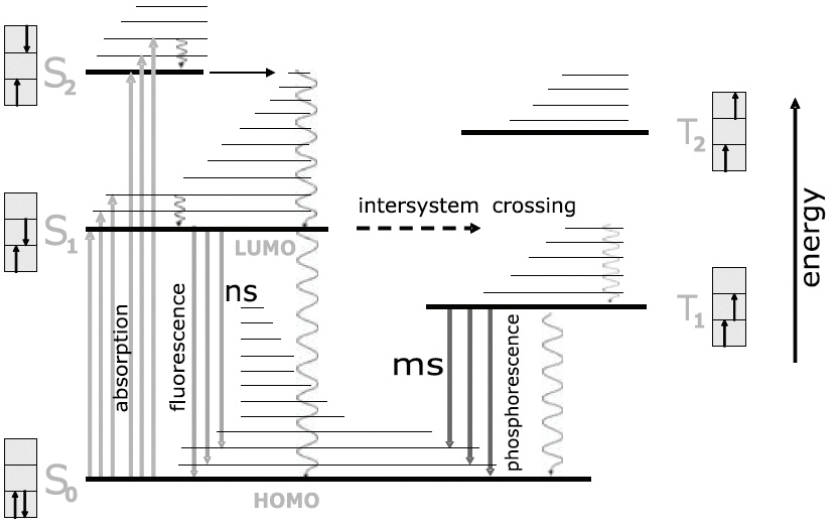

Figure 3.8: A schematic of the energy diagram of an organic molecule, where the singlet and trpliet states are complemented by a manifold of vibrational states. Radiative decays are illustrated by straight vertical lines, where as non-radiative decays, such as heat, are illustrated by wavy vertical lines. [Novotny and Hecht, 2006]

the recombination zones are not near the contacts because the metal quenches the light emission.[6]. By increasing the operation voltage the recombination zone can, however, be moved away from the cathode yielding a higher quantum efficiency.

Due to the quasi-1D nature of the polymers used in polymeric and organic LEDs the excess electron can cause a chain deformation, if there are no empty levels below the conduction level. Such deformations, which is usually about 20 sites long, are referred to as polarons. During this deformation process, an energy level is pulled up from the valence band with two electrons in it and a level is pulled down from conduction band. Hence, two levels will be created in the band gap, where the lower will be filled and the upper will contain the excess electron. The polaron, and thereby its lattice distortion, can move freely along the chain, even though its energy level lies in the band gap, enabling a contribution to the charge transport. An added electron and hole each creating a polaron, one negatively charged and one positive, respectively, may meet and recombine[7]. Finally, at higher charge carrier concentrations, where the polarons come close together, the charge carriers, donated to the chain, are kept in so-called bipolaron states. These different types of levels are illustrated in figure 3.9.

It may happen that the injected charge carriers, which travel as singly charged polarons or bipolarons can, when combined, form a singlet polaronic exciton. These decay radiatively with a photon energy smaller than band gap, but they cannot be distinguished from ordinary excitons experimentally.

An excited polymer can transfer energy to the surrounding polymers, also known as long-range energy transfer. This can be done in a number of ways. The term, energy transfer, will be used, when a process involves a donor and acceptor molecule, whereas the term, energy migration, will be used for migration

[6]The metal can have a quenching effect up to 60 nm away from the contact.

[7]An exception to this is tPA, in which solitons are formed.

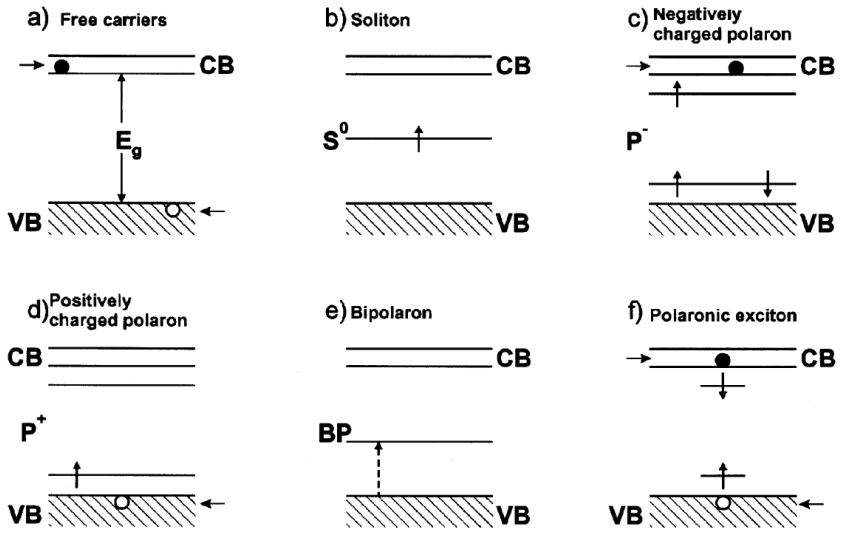

Figure 3.9: Various energy level types in conjugated polymers. [Kalinowski, 2005]

of excitons. Normally, a migration involves a series of energy transfers if no traps intervene the process. A cascade or trivial energy transfer involves a photon reabsorption by the acceptor molecule, emitted from the donor molecule, and is the most important process at long distances, typically around 100Å from the excitation site. This process lengthens the life time of the singlet states[8], again if defects no are involved, because the energy stored does not leave the crystal. The photoconductivity can also be highly influenced by this process. The energy transfer must also be taken into account, when studying the fluorescent spectrum of a given polymer. The directly transmitted light may be in error, because photons of short wavelengths tend to be reabsorped by the surrounding polymer, hence the transmitted light will contain "too much" light of longer wavelengths. In general, if an acceptor molecule does not decay radiatively< the energy transfer is termed quenching.

Föster resonant energy transfer is another energy transfer mechanism, which depends on an overlap between the absorption spectrum of the acceptors and the fluorescence spectrum for the donors. This energy transfer is due to a resonant dipole-dipole interaction. Once the donor molecule is excited it generates an oscillating dipole, which then generates an oscillating electric field. The donor molecule can then transfer the energy to the acceptor by resonantly exciting an oscillating dipole in the acceptor molecule and the probability for energy transfer is therefore highly dependent on the relative orientation of the two dipoles. It can be noted, that because the donor molecule decays to the ground state this energy transfer can only happen for singlet states. The energy transfer rate constant, due to Föster energy transfer, of randomly orientated dipoles separated by the distance r can be shown to be

$$k_{D\to A} = \frac{1}{\tau}\left(\frac{\overline{R_0}}{r}\right)^5 = \frac{1}{\tau_D}\left(\frac{R_0}{r}\right)^6, \tag{3.30}$$

[8]The lifetime can almost be doubled.

where τ is the observed lifetime of the excited state relative to the radiative lifetime of the donor, τ_D, through the fluorescence yield of the donor φ_{FL} in the absence of acceptors, where $\tau = \varphi_{FL}\tau_D$. and R_0 is the critical distance where the energy transfer rate equals the radiative decay rate. This distance is directly proportional to the overlap between the fluorescence spectrum of the donor and the absorption spectrum of the acceptor. $\overline{R_0}$ is the donor acceptor distance where the transfer competes equally with the total rate of removal of energy from the donor, such as radiative and non-radiative [9]. From equation (3.30) it follows that $\overline{R_0} = \varphi_{FL}^{1/6} R_0$.

Energy transfer can also happen for triplet states, which thus involves a tunnelling process of the excited donor electron to the acceptor and a tunnelling process of an electron in the ground state from the acceptor to the donor. This non-radiative energy transfer is also known as the Dexter transfer mechanism and can be shown to be given as

$$k_{D\to A} = \frac{2\pi}{\hbar}|\beta_{DA}|^2 \int F_D(E)F_A(E)dE,$$

where β_{DA} is the exchange energy interaction between the molecules, $F_D(E)$ and $F_A(E)$ is the normalised phosphorescence spectrum of the donor and the normalised absorption spectrum of the acceptor, respectively, in the energy interval dE. It can be noted that because the Dexter transfer has to do with tunnelling, the range of this transfer mechanism is small compared to the other two transfer mechanisms.

The transfer mechanisms described above can be used to improve the electroluminescent efficiency by e.g. a triplet-singlet transition enabling radiative decays. A further improvement could be reached if an quite effective triplet-singlet transfer happened from a phosphorescent donor to a fluorescent acceptor. [Kalinowski, 2005; Novotny and Hecht, 2006; Pope and Swenberg, 1999; Kristensen, 2008]

The quantum electroluminescent efficiency

The quantum electroluminescent efficiency φ_{EL} is one of the most important features, when dealing with OLEDs and by definition relates photon flux per unit area Φ_{EL} and carrier stream per unit area. Hence,

$$\varphi_{EL} \equiv \frac{e\Phi_{EL}}{J},$$

where a monochromatic emission for a constant photon energy is assumed. φ_{EL} clearly must depend on the operation voltage. The internal electric field is associated with electron-hole and very high fields can therefore lead to a drop in the electroluminescent efficiency, the so-called high field drop. The energy conversion efficiency is also a parameter used to describe the device performance and is given as

$$\eta = \frac{E_{EL}}{U},$$

[9] A typical value for $\overline{R_0}$ for organic solids is in the order of 3nm.

where E_{EL} is the light-energy flux and U is the electrical power consumed by the device. Because not all emitted light escapes the device, in fact this is usually a small fraction of the overall generated light, the external quantum electroluminescent efficiency is introduced as

$$\varphi_{EL}^{ext} = \xi\varphi_{EL} = \frac{e\Phi_{EL}^{ext}}{J} = \xi P\varphi_r,$$

where ξ is denoted as the light out-coupling efficiency, P is probability of creating a singlet or triplet state and φ_r is the efficiency of their radiative decay. It can be noted, that the probability of recombination $P_r = 1$ is assumed. If, however, this is not the case, the recombination probability is defined by

$$P_r = \frac{\tau_t}{\tau_t + \tau_{rec}} = \frac{1}{1 + \tau_{rec}/\tau_t} < 1,$$

with τ_t as the charge carrier transit time and τ_{rec} as the recombination time. The recombination time of a charge carrier can be expressed as $\tau_{rec}^{e,h} = (\gamma n, p)^{-1}$, with γ as the recombination coefficient, while the transit time must be $\tau_t = \frac{d}{\mu F} = \frac{d^2}{\mu V}$, where d is the sample thickness, μ is the charge mobility and V is the applied voltage. For comparable charge carrier concentrations, $n \approx p$, the following can be applied:

$$\frac{\tau_{rec}}{\tau_t} = \frac{e\mu_{e,h}(\mu_e + \mu_h)F^2}{\gamma jd} = \frac{8}{9}\frac{e}{\varepsilon_0\varepsilon}\frac{\mu_{e,h}\mu_t}{\gamma\mu_{eff}}\frac{J_{SCL}}{J}, \tag{3.31}$$

where the ratio $\frac{J}{J_{SCL}}$ defines the injection efficiency, μ_{eff} is the effective mobility of the carriers under the double injection current J and $\mu_t = \mu_e + \mu_h$.

As mentioned earlier, the recombination process in most organic solids can be assumed to be of the Langevin type in which the mean free path is smaller than the capture radius given by equation (3.29). By assuming, for convenience, stationary conduction electrons the average hole current density due to the attraction of an electron is given by

$$J_h = ep_g\mu_t F = ep_g\mu_t\frac{e}{4\pi\varepsilon\varepsilon_0 r_0^2},$$

where p_g is the concentration of generated holes. The total current entering the sphere is then

$$I = p_g\mu_t\frac{e^2}{\varepsilon\varepsilon_0},$$

which all recombines with the negative charge with a rate of $\gamma p_g e$. Thus,

$$\frac{\gamma}{\mu_t} = \frac{e}{\varepsilon\varepsilon_0} = constant.$$

Equation (3.31) then simplifies to

$$\frac{\tau_{rec}}{\tau_t} = \frac{8}{9}\frac{\mu_{e,h}}{\mu_{eff}}\frac{J_{SCL}}{J}.$$

and thereby enables the probability of recombination to be written as

$$P_r = \frac{1}{1+\frac{8}{9}\frac{\mu_{e,h}}{\mu_{eff}}\frac{J_{SCL}}{J}}.$$

[Kalinowski, 2005; Pope and Swenberg, 1999]

3.4 Degradation

A critical issue for the commercialisation of OLEDs is the operation and storage stability. A lifetime of tens of thousands of hours is reported, but the operation stability for a variety of different devices is still needed to be improved before OLED displays truly become a pervasive technology.
Different degradation mechanisms are observed, some caused by chemical reactions, which can reduce charge injection, mobility and luminescence efficiency, others due to heat, where the polymer simply melts. It has been observed that PPV and its derivatives can have a gradual loss in the luminescent efficiency caused by a cleavage in the conjugated chain by the vinylene linkage. Another issue, especially regarding MEH-PPV, is singlet oxygen, which can implicate the reactive intermediates. Singlet oxygen is quite stable and is most dominant in electrically excited polymers. Oxidation of the polymer by the oxygen and moisture in the air happen more readily than when not operating and it is therefore quite essential to encapsulate the device and fabricate it under protected atmosphere. If the anode is ITO, it has been shown, that the anode itself acts as an oxygen source for this chemical degradation, but this process can be greatly reduced by having a conductive layer on top the ITO, acting as a hole injecting or transporting layer.
The phenomenon known as blackspots, is widely used within the terminology of OLED degradation and has mostly been studied in Alq_3 and MEH-PPV devices. A blackspot is a region, often circular, which is non-emmissive in electroluminescent and randomly grows over the area of the device, as illustrated on figure 3.10. It has been revealed that very often there is a defect at the center of the spot formation, which penetrates the cathode to form what is called a pin-hole. The origin of black spots was studied by McElvain et al. [1996], where it was shown that the number of black spots is predetermined, most likely by defects introduced during device fabrication. Moreover, different chemical reactions at these defect spots create different products that might act as injection barriers.
It has been shown that the presence of even quite small amounts of water vapour leads to a much more rapid growth of blackspots. In fact a study done by Schaer et al. [2001] showed that water has a larger degrading effect than pure oxygen, because when a water molecule comes in contact with free charge

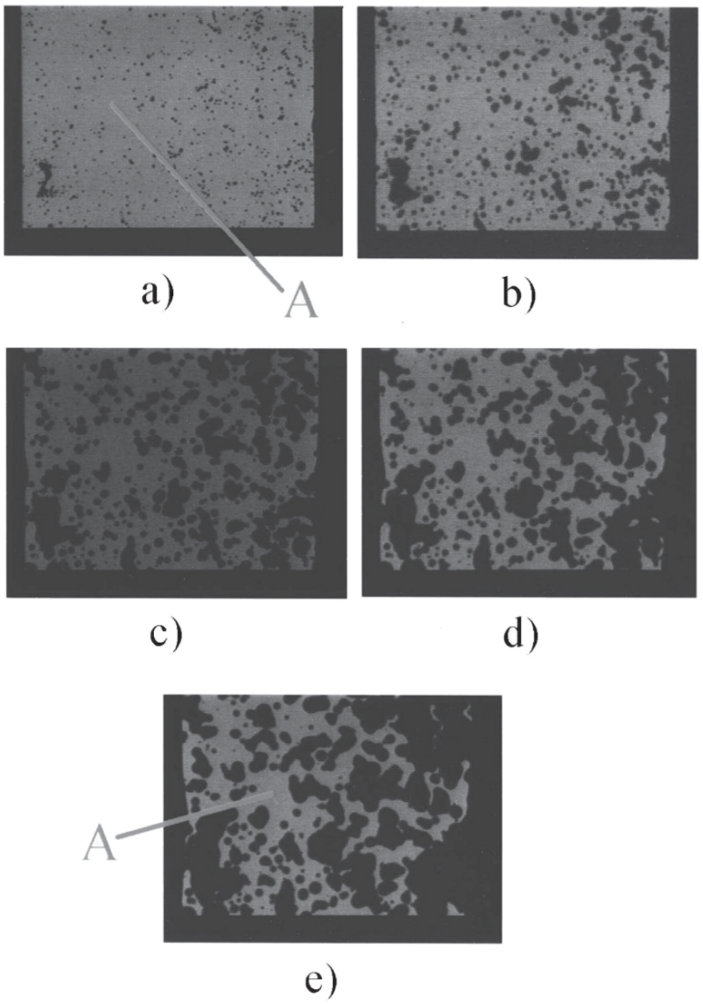

Figure 3.10: An evolution of black spot formation in air for an ITO/TPD/Alq3/Mg/Ag-device with an emissive area of 2 mm $\times$ 1.6 mm. The device was stressed by a constant voltage of 4.5 V and degradation time spanned over 40 hours. [McElvain et al., 1996]

carriers the molecule will be cleaved, as follows

$$2H_2O + 2e^- \rightarrow 2OH^- + 2H_2,$$

leaving the both the reactive compound OH^- and hydrogen gas formation.
Some OLED devices may exhibit, what is referred to as a burn-in. The first couple of minutes to hours of operation the device may change rapidly in the emission spectrum e.g. an increase in brightness, which has been suggested to be caused by an oxidation of the cathode by residual oxygen in the polymer, creating a barrier layer and the possibility of a more balanced charge injection. However, at most devices both the current and brightness are decreased for a constant voltage, but the mechanism termed juvenile aging, is not fully determined. It is believed that ion migration is involved. The time scale of ion migration and voltage dependence of these charges is consistent with that of the ion mobilities in organics, but the

ultimate effect of the mobile ions is not known. In the simplest cases they produce a bipolar layer which creates a counteracting field, which reduces the current. They may also act as charge carrier traps leading to a reduction in the charge carrier mobility around electrodes. Finally, two modes of electrochemistry may occur. Ions may retain charge at the electrodes, while the polymer may be reduced at the cathode or oxidised at the anode. Furthermore, the ions may be oxidised or reduced themselves leaving a probability of producing a neutral metal atom, which deposits on the cathode, discussed below, or a gaseous species may be produced, building up pressure deforming or delaminating the device.

Another failure of OLEDs is electrical shorting that can happen throughout the entire lifetime of the device for various reasons. This implies a short growing mechanism bridging the electrodes but yet again this mechanism is not fully understood. It has been suggested, that an In cation can migration to the cathode followed by a reduction of the ion, forming a metallic wire short-circuiting the device. This has been suggested, because it has been observed that devices with conducting polymer sandwiched between the emitter and ITO anode are found the be much less prone to shorting.

It has been found that using a stable dopant, such as rubrene, in the hole or electron transporting layer greatly enhance the lifetime of the small molecule OLEDs. The mechanism responsible for this is believed to be that the dopants act as traps for excitons or charge carriers. Hence, the molecules in the host matrix will be in their excited state for a small fraction of time and therefore has a lower probability of participating in a chemical reaction.

[Hadziioannou and Malliaras, 2007]

PART III

OLED FABRICATION

Materials and methods 4

Throughout this chapter the procedure for fabrication of OLEDs by the use of spincoating, is presented. Table F.1 on page 106 displays an overview of the fabricated OLEDs.

4.1 Spincoated OLEDs with PEDOT:PSS as hole transporting layer

As a starting point 0.5 cm of a 2.5×2.5 cm^2 ITO coated glass substrate with a sheet resistance of 4-8 Ω/□ was etched with 38% HCl. These ITO substrates were carved from a 5×7.5 cm^2 ITO coated glass plate with a diamond cutter. The etching was done to avoid a short-circuit in the final OLED when contacting the final device. The ITO substrates were cleaned in an ultrasonic bath with acetone and rinsed with ethanol followed by plasma cleansing in a RIE. This plasma treatment was carried out in an O_2 atmosphere at a pressure of 150 mTorr with a power of 100 W for 3 min.
The next step was to add an electron blocking layer[1], which was done with a 2.8 wt% PEDOT:PSS (Poly(3,4-ethylenedioxythiophene):Poly(styrenesulfonate)) dispersion in water with a PEDOT content of 0.14% and a PSS content of 2.66%. It has been found by, among other Jukes et al. [2004], that the PSS and PEDOT has an optimum mixture ratio at about 15:1 for the purpose of hole transporting layer. The molecular structure of PEDOT and PSS is shown on figure 4.1.

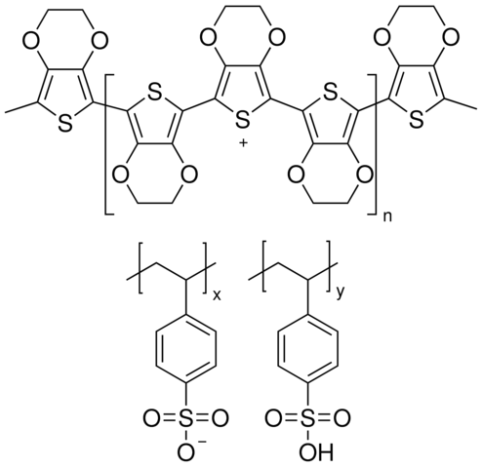

Figure 4.1: The molecular structure of PEDOT at the top and PSS at the bottom.

This dispersion was spincoated on the ITO-substrate at 1300 RPM for 50 s followed by a heating on a

[1] It was also attempted to fabricate OLEDs, purely with Al as cathode but without this layer no light was emitted from these devices.

80°C warm hotplate for about an hour to evaporate the water after which the additional layers could be applied.

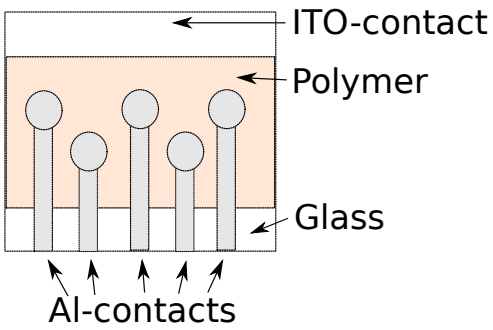

Figure 4.2: A schematic of the final OLED.

4.1.1 The ITO/PEDOT:PSS/PFO/Al-device

A solution of PFO in anisole with a concentration of 4mg/ml was made and added to the substrate and spun at 800 RPM for 50 s. This procedure was then repeated two times more yielding an emitting layer thickness of approximately 200 nm. It was found that when a specific layer was spincoated using repeating procedure, the resulting layer ended up with no holes, avoiding any short-circuits.
Five 250 nm thick Al contacts were then deposited using a DC sputter coater after which the polymer was removed with a Q-tip wetted with DCM at the opposite end of the etched ITO. A schematic of the final device is shown on figure 4.2 and a schematic of the aligned energy levels of the device is shown on figure 4.3.
To study the photoluminescence of PFO a glass substrate was spun with the same polymeric solution, as for the OLED, at 800 RPM for 50 s, where a 400 nm laser was used as pump. The measurements performed on sample 1 can be seen in section 5.1.1.

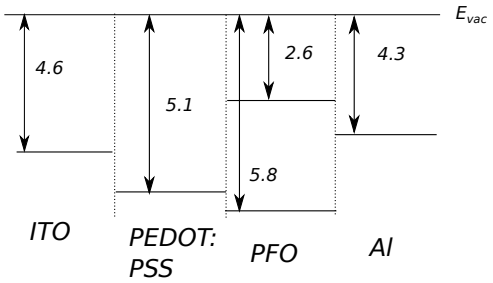

Figure 4.3: A schematic of the aligned energy levels of an ITO/PEDOT:PSS/PFO/Al-device in units of eV. The parameters for Al have been taken from Hung et al. [1997], ITO and PEDOT:PSS from Wang et al. [2011] and PFO from Lane et al. [2006].

4.1.2 The ITO/PEDOT:PSS/MEH-PPV/Al-device

A solution of MEH-PPV in anisole with a concentration of 4mg/ml was made and added onto the PEDOT:PSS layer and spun at 800 RPM for 50 s. This procedure was then repeated one more time, yielding an emitting layer thickness of approximately 180 nm. The contacts were deposited in the same way as described in the section above. A schematic of the aligned energy levels of the device is shown on figure 4.4.

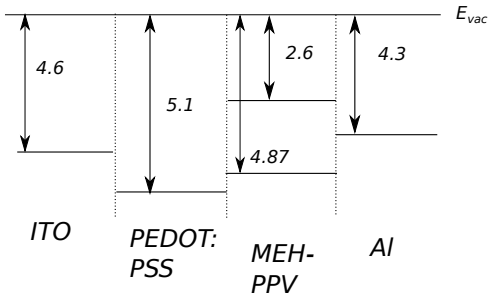

Figure 4.4: A schematic of the aligned energy levels of an ITO/PEDOT:PSS/MEH-PPV/Al-device in units of eV. The parameters for MEH-PPV has been taken from Cernini et al. [1997].

The photoluminescent properties of MEH-PPV was also measured by the means of a spincoated glass substrate with the same polymeric solution spun at 800 RPM for 50 s, where a 400 nm laser was used as pump. The measurements performed on sample 2 can be seen in section 5.1.2.

4.1.3 The ITO/PEDOT:PSS/PFO/Alq_3/LiF/Mg/Al-device

To achieve a longer lifetime and higher efficiencies of the devices the electron injection was optimised by using Mg as cathode and Tris-(8-hydroxyquinoline)aluminum, known as Alq_3, as an hole blocking layer. The molecular structure of Alq_3 is shown on figure 4.5.

It has been observed by Hung et al. [1997] that thin layers of LiF has band bending effect on Alq_3, which

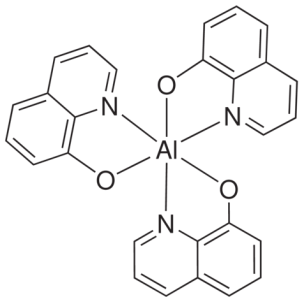

Figure 4.5: The molecular structure of Alq_3.

is why, it also was chosen to be sandwiched between the Mg contact and the Alq_3 layer because it was believed that the LiF would also have chemically stabilising effect. Alq_3 is known to display luminescent properties. The photoluminescent properties of Alq_3 was measured on a spincoated glass substrate with

a 400 nm laser as pump.
The PFO layer was made in the same way as described above. Afterwards 1.3 mg/ml Alq_3 in anisole was spun at 500 RPM. Then 1 nm of LiF, 40 nm of Mg and 150 nm of Al was deposited by e-beam sputtering. A schematic of the aligned energy levels of the device is shown on figure 4.6. The measurements done on sample 3 can be seen in section 5.1.3.

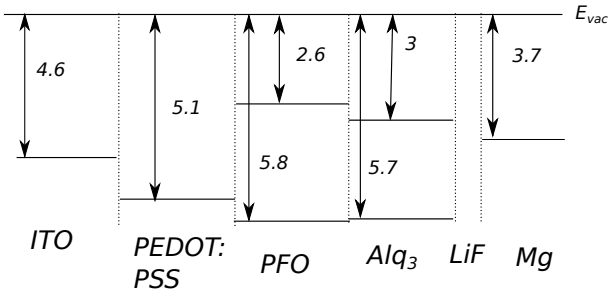

Figure 4.6: A schematic of the aligned energy levels of an ITO/PEDOT:PSS/PFO/Alq_3/LiF/Mg/Al-device in units of eV. The parameters for Mg has been taken from Hung et al. [1997] and Alq_3 from Kalinowski et al. [2001].

4.1.4 The ITO/PEDOT:PSS/MEH-PPV/Alq_3/LiF/Mg/Al-device

A device with MEH-PPV as the emitting polymer and Alq_3 as hole blocking material was also fabricated with Mg as electron injector. It was made in the same way as described in section 4.1.2, but after the polymer was adhered a solution of 1.3 mg/ml Alq_3 in anisole was added to the substrate and spun at 500 RPM, followed by the deposition of the LiF/Mg/Al contact. A schematic of the aligned energy levels of the device is shown on figure 4.7. The measurements performed on sample 4 can be seen in section 5.1.4.

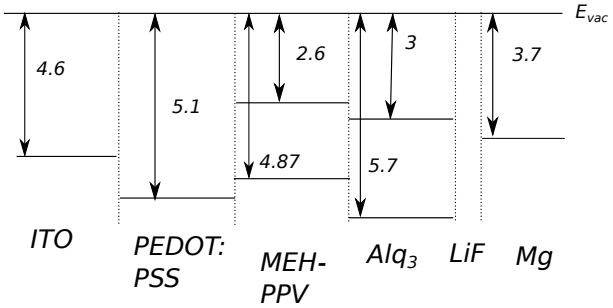

Figure 4.7: A schematic of the aligned energy levels of an ITO/PEDOT:PSS/MEH-PPV/Alq_3/LiF/Mg/Al-device in units of eV.

4.1.5 Additional experiments

In order to verify that the adhesion of the cathodes was the reason for device failure when a device was left to air exposure for about 24 hours without been turned on, a device similar to sample 4, where the

contacts were deposited after 48 hours was made. The measurements done on sample 5 can be seen in section 5.1.5.
Furthermore, a device similar to sample 4 was made with an additional 75 nm thick LiF encapsulating layer, referred to as sample 6. The measurements done on this sample is displayed in section 5.1.5.

4.2 Spincoated OLEDs with TPD as hole transporting layer

Because of a non-uniform layer thickness of the PEDOT:PSS layer and therefore a non-uniform current distribution throughout the device, another hole transporting layer was tried in order to obtain light emission from the entire area beneath the cathode. N,N'-Bis(3-methylphenyl)-N,N'-diphenylbenzidine, also know as TPD, was chosen, because it was believed that the clustering of the PEDOT:PSS was due to a hydrophobic ITO surface. Therefore spincoating with an organic solvent would eliminate this problem. The molecular structure of TPD is shown on figure 4.8.

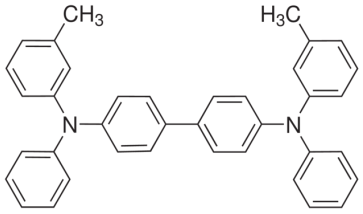

Figure 4.8: The molecular structure of TPD.

4.2.1 The ITO/TPD/PFO/Alq_3/LiF/Mg/Al-device

As mentioned TPD was now used as the hole transporting layer, so as a starting point a solution with 1.3 mg/ml TPD in anisole was spun on an ITO substrate at 500 RPM. This procedure was repeated twice after which the PFO solution was spun at 600 RPM. This procedure was repeated three times. Finally, a solution of Alq_3 in anisole also with a concentration 1.3 mg/ml was spun at 500 RPM. This procedure was repeated twice. The deposition of LiF, Mg, and Al was done in the same way as described above. The measurements done on sample 7 is shown in section 5.2 from which it appears that the device only emits light from the bottom of the contact. This was believed to be due to curved layers, because the devices were spun too slow. Therefore, a series of tests was done to find the best production parameters. Another sample, sample 8, was made by spincoating the substrate one time with a 4mg/ml TPD solution in anisole at 1000 RPM. Then the PFO was spincoated onto the substrate three times with a solution of PFO in anisole in the concentration 4mg/ml at 1000 RPM. A solution of 4mg/ml Alq_3 in anisole was then added and spun at 500 RPM, twice. Finally, the contacts were deposited in the same way as sample 7.
The most optimal procedure was found to be to spincoat the substrate four times with a 4mg/ml TPD

solution in anisole at 2000 RPM. The PFO layer was then added by spincoating the substrate four times with a solution of PFO in anisole in the concentration 4mg/ml at 2000 RPM and finally the electron transporting layer was added by spincoating the sample three times with a solution of 4mg/ml Alq_3 in anisole, also at 2000 RPM.
A schematic of the aligned energy levels of the device is shown on figure 4.9. The measurements done on sample 9 can be seen in section 5.2.

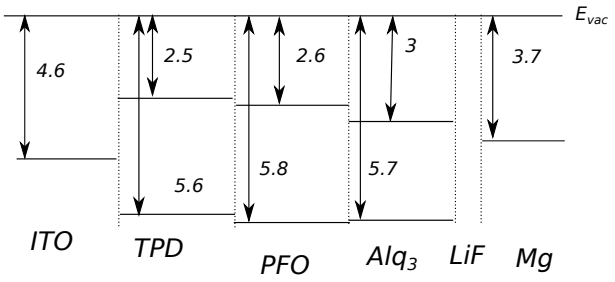

Figure 4.9: A schematic of the aligned energy levels of an ITO/TPD/PFO/Alq_3/LiF/Mg/Al-device in units of eV. The parameters for TPD has been taken from Kalinowski et al. [2001].

4.2.2 Degradation of encapsulated PFO devices

Without any encapsulating layer to protect the device when operating the lifetime was in the matter of minutes. Therefore, 75 nm LiF was deposited on to the OLED to cover the device after the deposition of the contacts. It should be noted that in order to do this, the sample had to be removed from the e-beam sputter and therefore exposed to air, though under clean room conditions.
It was expected that the rapid degradation mainly was due to the humidity in the air so in order to verify this, devices similar to sample 9 was made, though before the spincoating procedure the ITO substrate was heated to 150°C to ensure no water on the ITO substrate and 75 nm LiF was deposited after applying the contact as encapsulating layer. Devices with LiF as encapsulating layers with a thickness of 150 nm and 250 nm were also made. Furthermore, a transparent protecting laminating film[2] was glued on top of the LiF on all of the encapsulated devices. Lifetimes were also measured for a device in a protected N_2 atmosphere and for another in air. For the experiment with the protecting N_2 atmosphere the device was placed in a glove bag right after the fabrication. The glove bag was then purged 24 hours before doing any measurements. After the purge, the glove bag was inflated with N_2 after which the lifetime was measured. Finally, a device was spun under clean room conditions to investigated if that would extend the lifetime.
The lifetimes were investigated by fixing a culminating lens right on top of the OLED after which the emission spectra were logged at an operating voltage of 10 V.
The measurements done on these samples can be seen in section 5.2.2.

[2]This film was fabricated by Amcor. It lets 0.1 g/day/m^2 H_2O and 0.01 cm^3/day/atm O_2 through.

4.2.3 The ITO/TPD/MEH-PPV/Alq_3/LiF/Mg/Al-device

To investigate if the rapid degradation is correlated to the polymer, devices with MEH-PPV as emitting layer were made.
Except for the emitting layer, the device was made in the same way as sample 9. The concentration of the MEH-PPV solution was also 4mg/ml, in anisole. It was, however, found that this procedure yielded a clustered emitting layer leading to an uneven emission of light. This device is referred to as sample 15 and is displayed in section 5.2.3. Therefore, a series of devices were made in order to solve this.
It was found that spinning the substrates faster yielded a more even emission layer, but also thinner emitting layers. The emitting layer of sample 16 was then spun at 3000 RPM. This procedure was repeated six times but the device did still not emit light from the entire cathode. Sample 17 was then spun six times at 4000 RPM, which was enough to obtain light emission from the entire cathode.
The adhesion of the Alq_3 layer was also done in another way than the PFO-devices. Because the Alq_3 solution dissolved the MEH-PPV layer, the spincoating procedure was only done one time.
A schematic of the aligned energy levels of the device is shown on figure 4.10. The measurements performed on sample 9 can be seen in section 5.2.3.

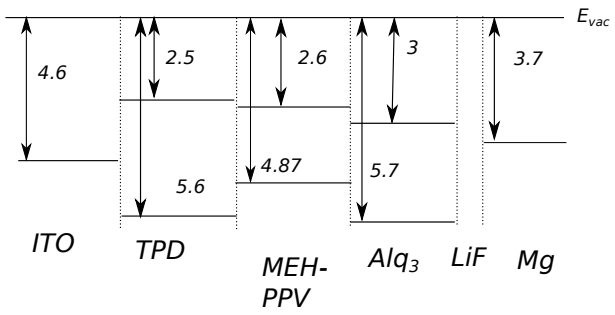

Figure 4.10: A schematic of the aligned energy levels of an ITO/TPD/MEH-PPV/Alq_3/LiF/Mg/Al-device in units of eV.

4.2.4 Degradation of encapsulated MEH-PPV devices

Devices with encapsulating LiF layers was also made with thickness's of 75nm, 150nm and 250 nm, also with the same protecting film. Also, a device was spun under clean room conditions.
The lifetime was investigated in the same way as the PFO devices but with an operating voltage of 6.5 V. The measurements done on these samples can be seen in 5.2.4.

Results

5

5.1 Spincoated OLEDs with PEDOT:PSS as hole transporting layer

5.1.1 The ITO/PEDOT:PSS/PFO/Al-device

The emission spectrum of the ITO/PEDOT:PSS/PFO/Al-device is shown on figure 5.1a), whereas the I/V characteristics of the device is shown on figure 5.1b). It is seen that the electroluminescent spectrum is with an emission peak at a wavelength around 500 nm and a small peak around 440 nm, whereas the photoluminescent spectrum has a dominant emission peak at 440 nm and one phonon transition at about 465 nm, 500 nm, and 540nm. The emission spectra have been shifted to the same peak value.

a)

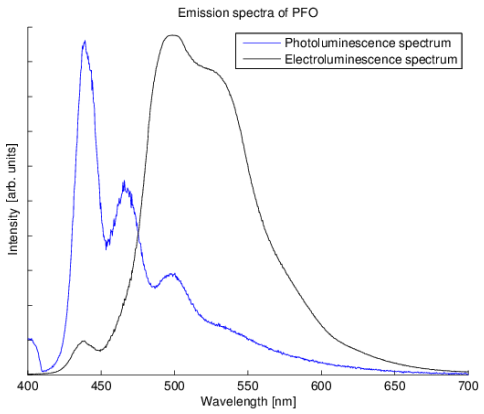

b)

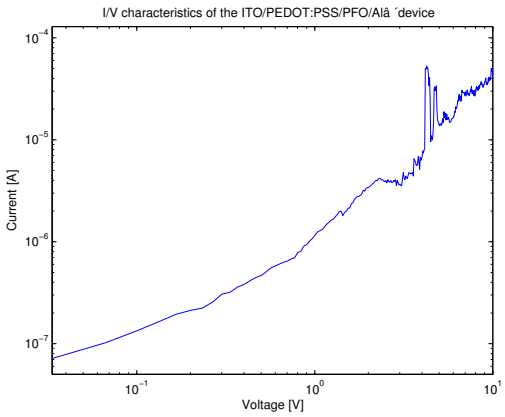

Figure 5.1: a) The photoluminescent and electroluminescent spectrum of a spin-coated ITO/PEDOT:PSS/PFO/Al-device. b) The I/V characteristics of the ITO/PEDOT:PSS/PFO/Al-device.

5.1.2 The ITO/PEDOT:PSS/MEH-PPV/Al-device

The emission spectrum of the ITO/PEDOT:PSS/PFO/Al-device is shown on figure 5.2a), whereas the photoluminescent spectrum is shown on figure 5.2b). It is seen that the device emits with an emission peak at a wavelength around 590 nm. It shall also be noted that the intensity from this device was quite low. No I/V characteristics were measured on this sample because the device degraded too fast when contacting it.

a)

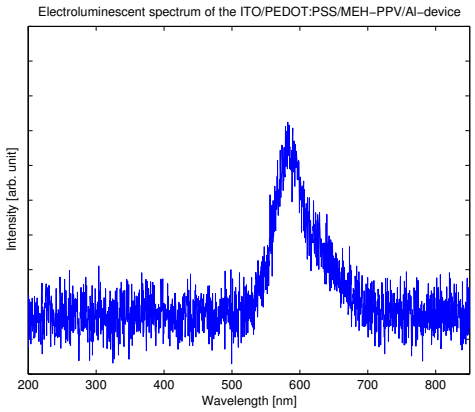

b)

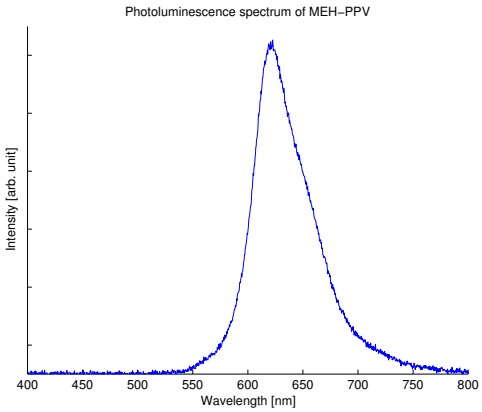

Figure 5.2: a) The emission spectrum of a spincoated ITO/PEDOT:PSS/MEH-PPV/Al-device. b) The photoluminescence spectrum of MEH-PPV.

5.1.3 The ITO/PEDOT:PSS/PFO/Alq_3/LiF/Mg/Al-device

The emission spectrum measured on this device is shown on figure 5.3a) with intensity peaks similar to those found by Kristensen [2008]. The first one being a purely electron transition and the two others being electron-phonon transitions. The outermost peak around wavelength of 540 nm is believed to be emission from the Alq_3. The measurement is shown on the same plot where the peaks have been shifted to the same intensities.

I/V measurements were also done on this sample which reveals a clear indication of the trap and space charge limited currents, as illustrated on figure 5.3b). A set of I/V measurements done right after each other is shown on figure 5.4, where it is seen that the device conductivity decreases after each measurement. This is taken to be a sign of degradation. A picture of a device similar to this while emitting light, is shown on figure 5.7a).

a)

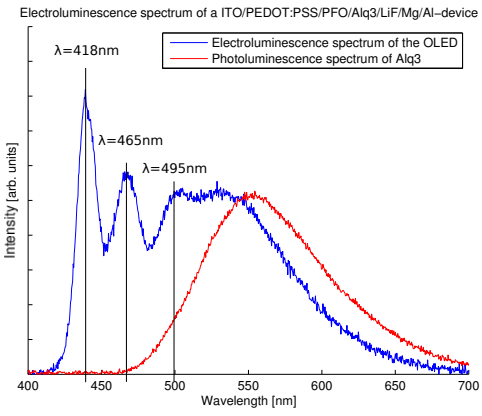

b)

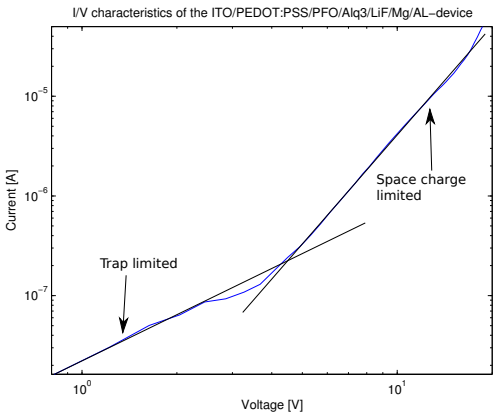

Figure 5.3: a) The electroluminescent spectrum of a spincoated ITO/PEDOT:PSS/PFO/Alq_3/LiF/Mg/Al-device. b) The I/V characteristics of the same device.

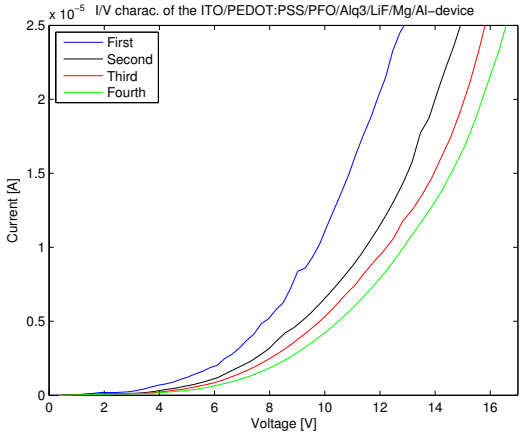

Figure 5.4: The I/V characteristics of the device done right after each other.

5.1.4 The ITO/PEDOT:PSS/MEH-PPV/LiF/Alq_3/Mg/Al-device

The emission spectrum of the ITO/PEDOT:PSS/PFO/Alq_3/Al-device and the measured I/V characteristics are shown on figure 5.5, whereas a set of I/V measurements done right after each other are shown on figure 5.6, which also reveals degradation. It is seen that the device emits similarly as the device without Alq_3 and that there where no noticeable difference in intensity compared to the device without Alq_3, LiF, and Mg. A picture of the diode while emitting light is shown on figure 5.7b).

a)

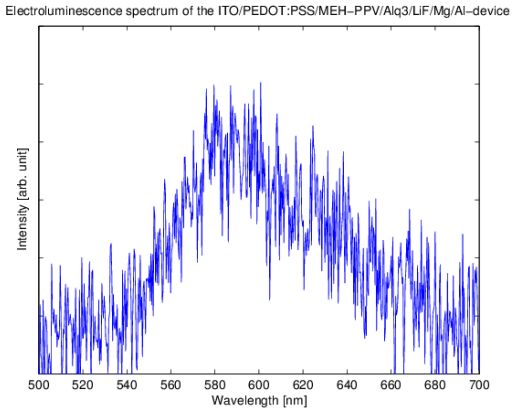

b)

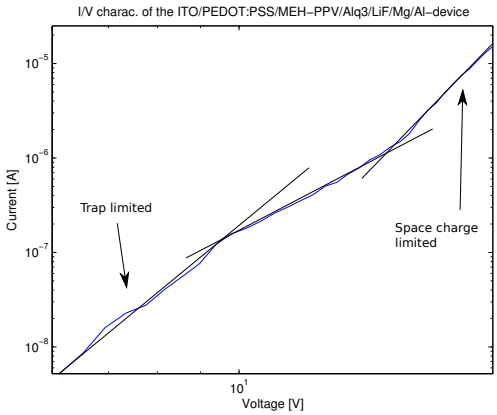

Figure 5.5: a) The electroluminescent spectrum of a spincoated ITO/PEDOT:PSS/MEH-PPV/Alq_3/LiF/Mg/Al-device. b) The I/V characteristics of the same device.

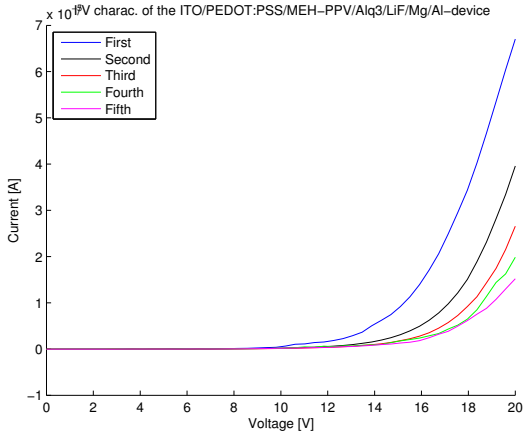

Figure 5.6: The I/V characteristics of the device done right after each other.

5.1.5 Additional eksperiments

A picture of the diode with PFO as emitting layer, which has been left for 48 hours before depositing the cathode is shown on figure 5.7a), from which it is seen that there is not emission of light from the entire cathode. Therefore the device failure must follow from the deposition of the cathode and without any encapsulating layers the devices could not emit light after 24 hours air exposure.
The uneven light emission was observed on all of the devices made with PEDOT:PSS. This was expected to be due to a non-uniform PEDOT:PSS-layer, which originated from the spin coating when the water evaporated and the PEDOT:PSS clustered. A picture of a device with MEH-PPV as emitting layer is shown on figure 5.7b).

a)  b) 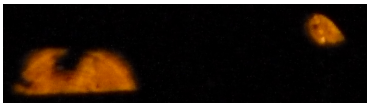

Figure 5.7: a) An image of a device of with PFO as emitting layer. b) An image of a device of with MEH-PPV as emitting layer. It can be noted that the devices do not emit light from the entire cathode.

A picture of a PFO device with a 75 nm thick LiF encapsulating layer is shown on figure 5.8a) and a picture of the same device after four days of exposure to air is shown on figure 5.8b). It shall be noted that this device was not turned on, the time in between the pictures were taken.

a)  b) 

Figure 5.8: a) A picture of PFO-device with a 75 nm thick LiF encapsulating layer. b) A picture of the same device after four days.

5.2 Spincoated OLEDs with TPD as hole transporting layer

5.2.1 The ITO/TPD/PFO/LiF/Alq_3/Mg/Al-device

A picture of sample 7, 8, and 9, is shown on figure 5.9. It is seen that even though the devices emit light from the entire contact blackspots still occur. This was seen on every device made. The electronlumi-

Figure 5.9: a) A picture of sample 7, b) sample 8, and c) sample 9 while emitting light.

nescence spectrum of sample 9 is shown on figure 5.10a), whereas the I/V characteristics are shown on figure 5.10b). It is clear that these devices has a much higher conductivity than the devices with PEDOT:PSS. The reason for the I/V measurements was not done at a larger voltage span was because of limitations of the measuring instruments. Because of the low voltage span, no limited currents could be identified.

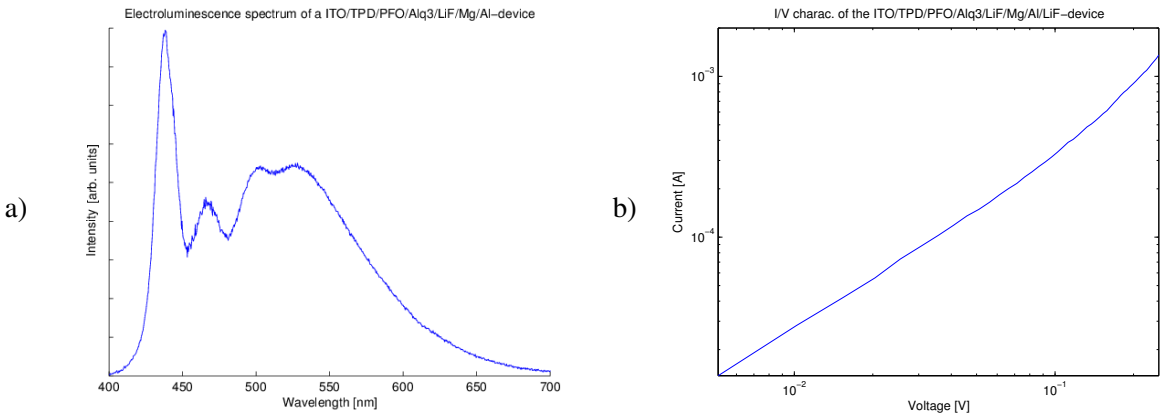

Figure 5.10: a) The electroluminescent spectrum of a spincoated ITO/TPD/PFO/Alq_3/LiF/Mg/Al-device. b) The I/V characteristics of the same device.

5.2.2 Degradation of ITO/TPD/PFO/Alq_3/LiF/Mg/Al/LiF devices

Emission spectra measured over time for the device with a 75 nm thick LiF encapsulating layer degrading in air are shown on figure 5.12a) and the emission spectra for the device degrading in a N_2-atmosphere are shown on figure 5.12b). Also, the time evolution of the emission spectrum for a device with a 150 nm LiF thick encapsulating layer and a device with a 250 nm LiF thick encapsulating layer is shown on figure 5.13a) and 5.13b), respectively. Because the background signal also drops over time the peaks must be set relative to the signal from the surroundings. The emission drop thereby corresponds to the

flattening of the intensity curves.

Furthermore, six I/V characteristics measured right after each other in air on a device with a 150 nm

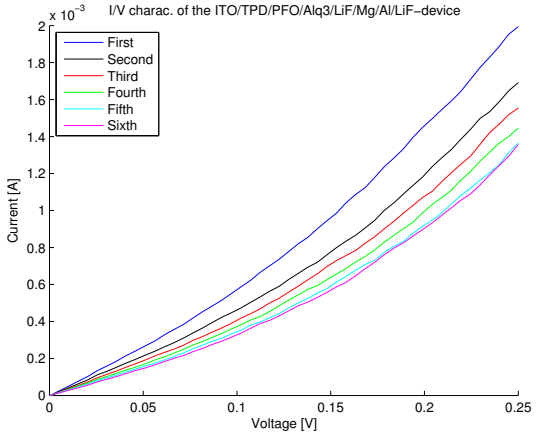

Figure 5.11: The I/V characteristics of the device done right after each other.

thick LiF encapsulating layer, are shown on figure 5.11, from which it is seen that the current drops after each measurement. This indicates degradation occurs when contacting the device.

It shall be noticed that the protecting atmosphere only lengthened the lifetime of the device from 30 minutes to 40 minutes, indicating that the humidity and oxygen in the air is not the main reason for degradation of these devices.

A further indication of this is that a variation in the thickness of the encapsulating layer does no affect

a)

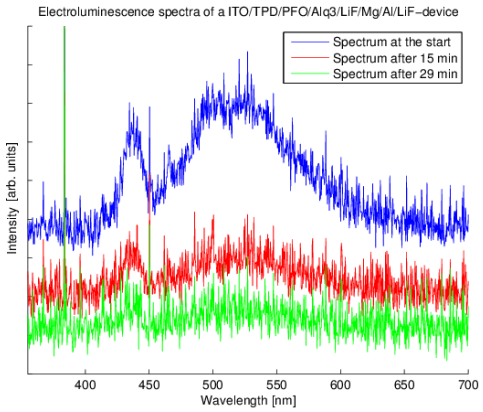

b)

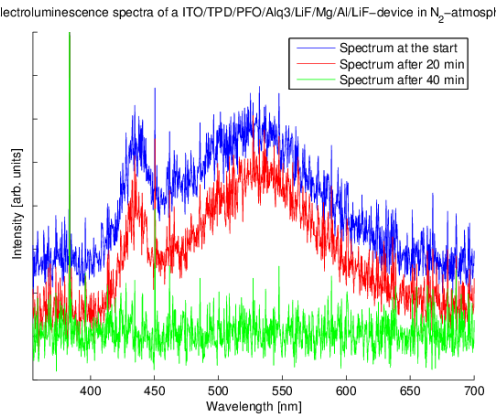

Figure 5.12: a) The time evolution of the electroluminescent spectrum of a spincoated ITO/TPD/PFO/Alq_3/LiF/Mg/Al-device with 75 nm thick LiF encapsulating layer. b) The time evolution of the electroluminescent spectrum of a spincoated ITO/TPD/PFO/Alq_3/LiF/Mg/Al-device with 75 nm thick LiF encapsulating layer in an N_2-atmosphere.

the lifetime of the OLEDs. Therefore, the device was made under clean room conditions and with a 150 thick LiF encapsulating layer in order to investigate if blackspots still would occur under these fabrication conditions. It is seen from figure 5.14 that they do. In fact, this device failed before any measurements of the emission spectrum could be done.

a)

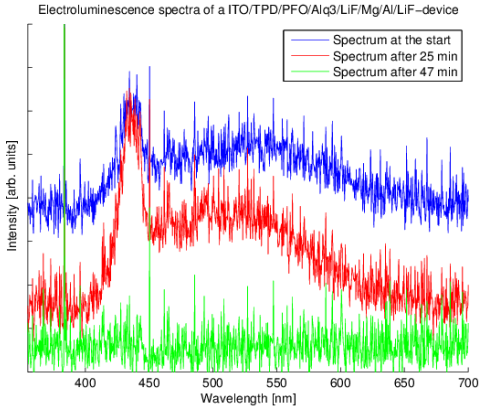

b)

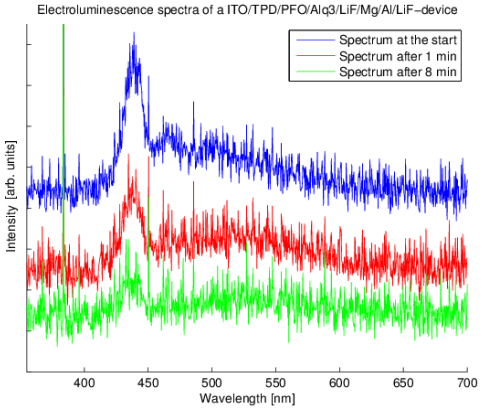

Figure 5.13: a) The time evolution of the electroluminescent spectrum of a spincoated ITO/TPD/PFO/Alq_3/LiF/Mg/Al-device with 150 nm thick LiF encapsulating layer. b) The time evolution of the electroluminescent spectrum of a spincoated ITO/TPD/PFO/Alq_3/LiF/Mg/Al-device with 250 nm thick LiF encapsulating layer.

To determine if the blackspots somehow was related to ITO substrate, e.g. glass dust from the cutting

Figure 5.14: A picture of a device with 150 nm thick LiF encapsulating spincoating under clean room conditions. It is seen that blackspots is not avoided by spincoating under clean rooms conditions.

of the ITO substrate, which has survived the cleaning process, a substrate was examined with a SEM. These scans can be seen on figure 5.15, from which it is seen that the ITO substrates are quite clean.

5.2.3 The ITO/TPD/MEH-PPV/Alq_3/LiF/Mg/Al-device

Pictures of sample 15, 16 and 17 are shown on figure 5.16. It is seen that blackspots still occur.

These devices did, however, emit more light than those devices with PEDOT:PSS as hole transport layer. The emission spectrum and I/V characteristics of sample 17 are shown on figure 5.17a) and figure 5.17b), respectively. This spectrum is very similar to the photoluminescent spectrum seen on figure 5.2b), though the intensity peaks are blue-shifted by 10 nm compared to the study done by Kristensen [2008], where the pure electron transition was found at a wavelength of 587 nm and one electron-phonon transition at 640 nm. Here the electron transition is at 577 nm and the electron-phonon transition is at 630 nm. It is also seen that these devices conduct a lot more current at low voltages than those with PEDOT:PSS. Again the I/V measurements could only be done within a short voltage span and it is therefore not possible to identify any limited currents.

a) b)

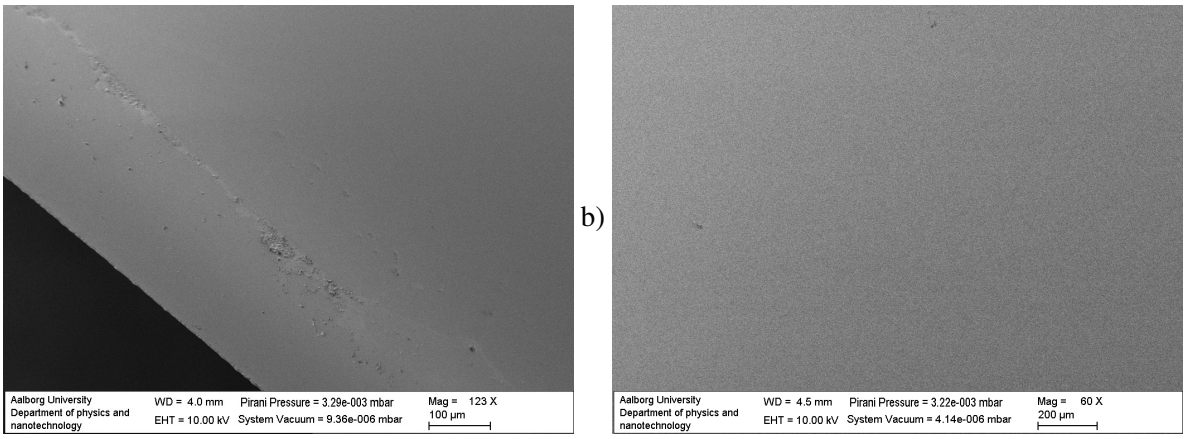

Figure 5.15: a) A SEM picture of the side of an ITO substrate revealing a scratch from the cutting. b) A SEM picture of the middle of the ITO substrate.

a) b) c)

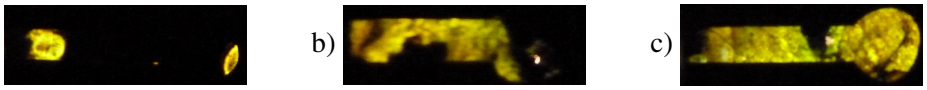

Figure 5.16: a) A picture of sample 15, b) sample 16, and c) sample 17 while emitting light.

a) b)

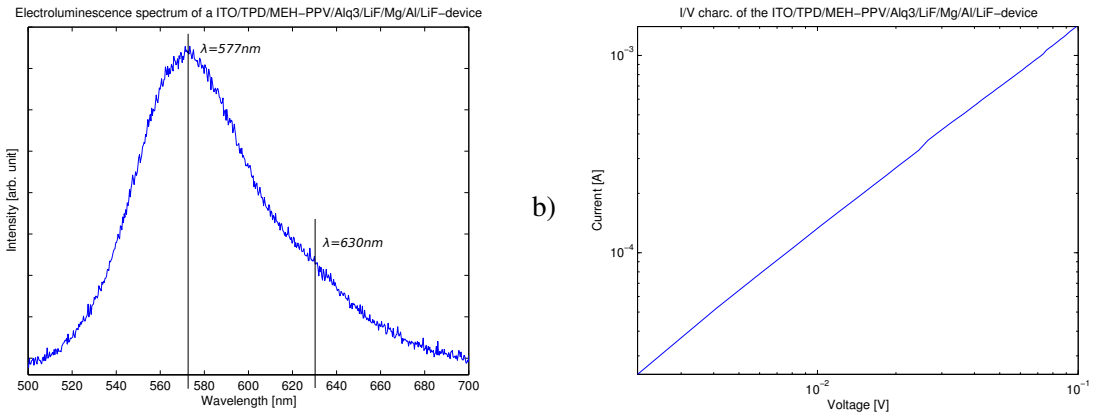

Figure 5.17: a) The electroluminescent spectrum of a spincoated ITO/TPD/MEH-PPV/Alq_3/LiF/Mg/Al/LiF-device. b) The I/V characteristics of the same device.

5.2.4 Degradation of ITO/TPD/MEH-PPV/Alq_3/LiF/Mg/Al/LiF devices

As for the PFO devices, six I/V characteristics measured right after each other on a device with a 150 nm thick LiF encapsulating layer were performed. These measurements are shown on figure 5.18a), where it is seen that this device also degrades, when contacting the device, but the short voltage span makes it hard to say how much.

The time evolution of emission spectra for devices with encapsulating LiF layers with thicknesses of 75 nm (sample 18), 150 nm (sample 19) and 250 nm (sample 20), is shown figure 5.18b), 5.19a) and 5.19b), respectively. It is seen that the lifetime of sample 18 only was 4 minutes and the lifetime of sample 19 and 20 were about ten minutes. Also a device was spun under clean room conditions, sample 21. A picture of sample 21 emitting light is seen on figure 5.20, revealing blackspots. Again no spectrum was measured from this device, because it failed before the measurement could be done.

a) b)

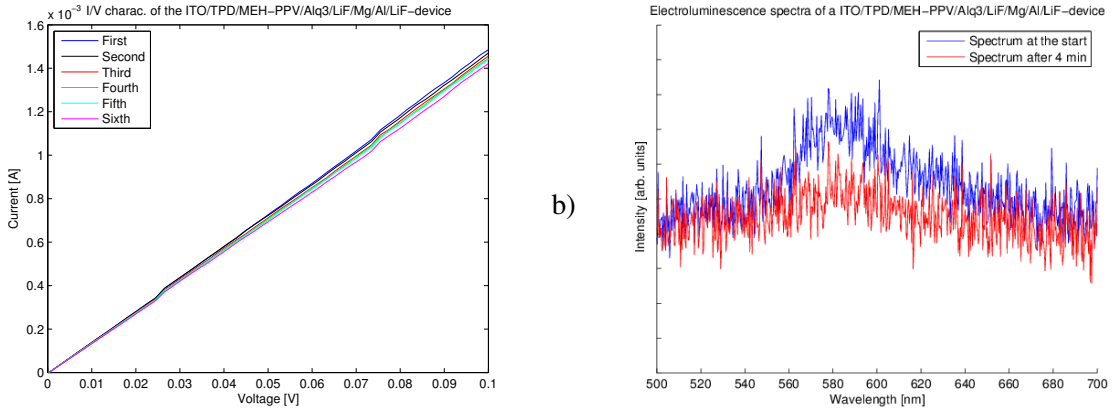

Figure 5.18: a) The I/V characteristics of the device done right after each other. b) The time evolution of the electroluminescent spectrum of a spincoated ITO/TPD/MEH-PPV/Alq_3/LiF/Mg/Al-device with 75 nm thick LiF encapsulating layer.

a) b)

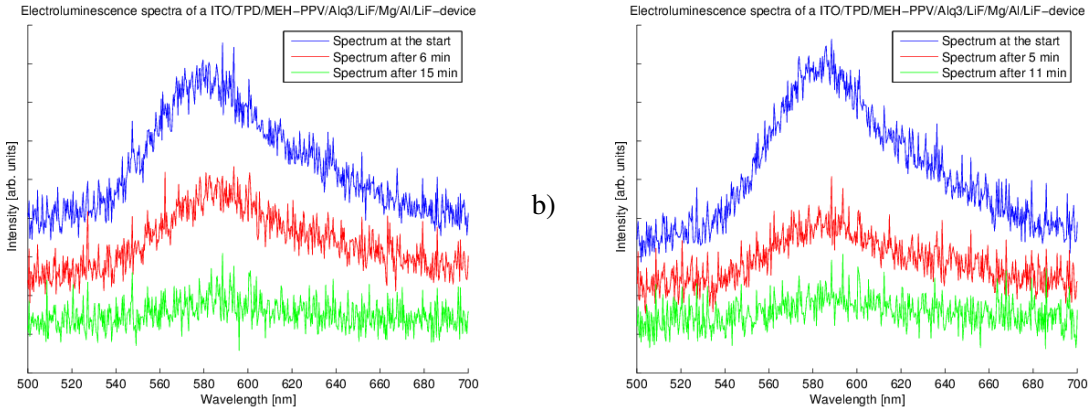

Figure 5.19: a) The time evolution of the electroluminescent spectrum of a spincoated ITO/TPD/MEH-PPV/Alq_3/LiF/Mg/Al-device with 150 nm thick LiF encapsulating layers. b) The time evolution of the electroluminescent spectrum of a spincoated ITO/TPD/MEH-PPV/Alq_3/LiF/Mg/Al-device with 250 nm thick LiF encapsulating layer.

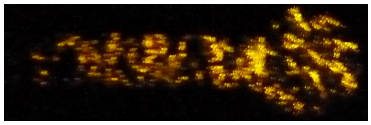

Figure 5.20: A picture of a MEH-PPV device with 150 thick LiF encapsulating spincoated under clean room conditions. It is seen that blackspots still occur.

Discussion 6

The fast degradation of the devices with only Al-contacts is expected mainly to be due to a poorly balanced charge injection. Electrons have to overcome a relatively high barrier to enter the polymer and when the applied voltage is sufficient for the injection to happen, the hole current will be so high, that the emitting layer is damaged, due to the generated heat. Some samples became so warm, that the glass splintered. This barrier height can also explain the potential independence seen at the I/V characteristics. Because of the barrier the cathode contact is not ohmic, whereas the LiF/Mg-contact seems to form a rather ohmic contact to the organic layers. This can be seen on the I/V characteristics, which seem to be divided into a trap-limited current and space-charge limited current for the devices with PEDOT:PSS as the hole-transporting layer. Because of the short voltage span at the devices with TPD as the hole-transporting layer it is hard to say any if the current, somehow, is limited. However, within the short voltage span the current seems to have a potentially dependence on the voltage. The model for the trap and space charge limited currents thus seem to fit the I/V characteristics.

The difference in the relative peaks seen at the electro- and photoluminescence can be due to different locations of recombination zones [Kristensen, 2008]. At photoluminescence the recombination zone extends throughout, where the laser excites the polymer, but at electroluminescence the low charge carrier mobilities place the recombination zone close to one of the contacts. The metal can, due to the short distance, affect the electron-phonon coupling and thus change the relative intensities of the the transitions. Hence, when using an electron transporting layer, the recombination zone is moved away from the cathode. A combination of this and a more efficient electron injection explains the difference in the two emissions spectra seen at the PFO devices with only Al as contact and the devices with the LiF/Mg/Al contact.

It can concluded that the humidity and oxygen in the air is not the main reason for the device failure at the encapsulated device with layer thickness of 150 nm and above, because the lifetime is not affected, when making the encapsulating layers thicker. The main reason for device failure is then expected to be caused by the defects that gives rise to the blackspots. These defects can originate from a number of things. These defects can emerge from tiny lumps of undissolved polymer which e.g. could be formed when the solvent evaporates. However, this problem could not necessary be solved by changing the solvent because the underlying polymer layer would then be dissolved, when spincoating an additional layer. In fact, it was attempted to fabricate OLED with chlorobenzene as a solvent in stead of anisole but no functional devices could be made with this procedure. Different kinds of contamination from the air when spincoating or preparing the the solutions could also give rise to the defects, but because the devices spun in a clean room still displayed blackspots, makes contamination of the solution most likely of those two options.

Another, likely, possibility is that the solution will patchy dissolve the underlying layer during the spincoating, leaving uneven layers and thereby uneven current distribution through the device. The areas for which the current is large can decompose due to the heat generated by the current. This problem, regarding the solvent, could be avoided by an alternating spincoating procedure of water soluble and water insoluble layers. It will thus be possible to use organic solvents with a higher dissolving power. Finally, the blackspots could also be caused by water and oxygen from air in the clean room after the deposition of the contacts, before the deposition of the encapsulating LiF, and the devices were taken out of the E-beam sputter to change masks. But because the blackspots did not mostly occur at the sides of the contacts, where the diffusion path would be shortest, this is not believed to be the main reasons for the occurrence of the blackspots.

Uneven layers are expected to be the reason for the device failure at the well-encapsuleted devices, because the MEH-PPV devices did not display a long lifetime compared to the PFO devices and it was observed that the MEH-PPV had a tendency to cluster whereas the PFO did not.

The devices spun in the clean room both failed rapidly. The reason for this is not quite clear, but one possibility is that the spincoater used in the clean room somehow spins differently than the one used outside the clean room. If it accelerates and/or decelerates faster and/or slower than the one outside the clean room, the resulting layer could be of another uniformity and thickness. This dependency could obviously be investigated further.

It was not possible to investigate the efficiencies of the fabricated OLEDs. Such experiments might give insight to whether the device failure could be due to some current generated heat caused by e.g. a poor charge injection or inefficient charge carrier blocking layers.

PFO displays more noticeably phonon transitions than MEH-PPV. Even though this was not investigated throughout this project, this can qualitatively be explained by the backbones of the polymers. The side groups of PFO locks the two benzene rings together making a rather rigid backbone compared to MEH-PPV. Due to this, phonons are more easily excited in the PFO backbone compared to the MEH-PPV. Furthermore, because of the rigid backbone in PFO, phonons will not be as damped as in the MEH-PPV backbone.

PART IV

CONCLUSION & PERSPECTIVES

Conclusion 7

The electronic properties of selected conjugated polymers has been investigated by combining a DFT approach with experimental data. These conjugated polymers displayed semiconducting nature, where it seems that the band gaps can be red-shifted by making polymer derivatives with the interconnecting atoms being more electronegative, than the backbone atoms. Also, high exciton binding energies is found for these conjugated polymers, dominating the optical properties.

It was attempted to fabricated long lifetime OLEDs by a simple spincoating procedure, where the longest lifetime measured was close to one hour. The reason for relative rapid device failure is estimated to be due to uneven layers and defects, observed as blackspots. The native issue regarding the chemical instability of low work functions necessary for efficient OLEDs seems, however, solved by encapsulating the devices with 150 nm of LiF combined with a laminating protecting film. A suggested procedure for further development of the OLED fabrication is a spincoating procedure with alternating water insoluble and water soluble layers.

Perspectives

8

A crucial factor for the breakthrough of organic electronics, such as organic solar cells, thin-film transistors and light emitting diodes, is an offer of cheap production processes. However, due to a demand of low work function materials, like Mg, Ca or Cs, for contacts, different encapsulating techniques are used to ensure no oxygen or water reaches the low functions contact leading to an absolute device failure because of the chemical instability of the low work function materials. These encapsulating techniques, among other, complicates the production processes, significantly.

Zhou et al. [2012] found a way to reduce the work function of selected metals, such Al, Ag and Au, and metal oxides, such as ITO and ZnO, by a so-called surface modification. This idea is not new but what makes their approach attractive is that their approach offers a cheap way of obtaining air-stable substrates of low work function, enabling e.g. roll-to-roll production. They demonstrate that an ultra-thin layer, in the order of 10 nm, of polyethylenimine ethoxylated (PEIE) will reduced the work function for e.g. ITO from 4.4 eV to 3.3 eV and Au from 5.1 eV to 3.9 eV. The molecular structure of PEIE is shown on figure 8.1. PEIE contains aliphatic amine groups, which physisorps onto the conductor surface because of the associated dipole moment of the amine groups.

The commercially available polymer can easily be processed under ambient conditions and is soluble in

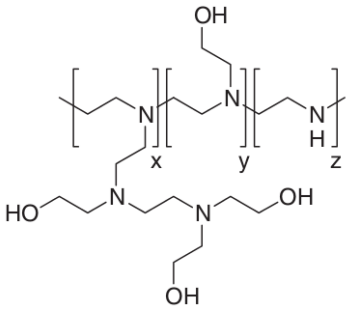

Figure 8.1: The molecular structure of polyethylenimine ethoxylated (PEIE). [Zhou et al., 2012]

environmentally friendly solvents like water and ethanol. Also the thermal stability in air of PEIE coated ITO was investigated, where it was shown that ITO/PEIE substrate did not suffer any changes until a temperature of 190°C. Furthermore, aqueous solutions are stable for more than a year and PEIE-coated ITO substrates also remain fairly stable under normal ambient conditions for more than four weeks[1].

The reason for this procedure appears universal is that the polymer physisorps to a conductor surface, which enables work function reduction of a diverse group of conducting materials. According to their study the neutral amine groups are primarily involved in the surface interactions, giving rise to interface dipoles and the reduction in the work function.

[1] They did, however, report a slight variation in the work function for the devices. In the order of 0.2 eV

They tested the ability to inject electrons from PEIE coated ITO into the organic semiconductor copper(II) phthalocyanine (CuPc) with a Mg/Ag top electrode compared to a device a without PEIE treatment. The device structures, measurements and a schematic of the aligned energy levels are shown on figure 8.2. With the PEIE treated ITO they reduced the barrier for injecting electron through the ITO from 1.3 eV to 0.36 eV. This yielded nearly symmetric J/V characteristics for PEIE coated ITO, where ITO electrode injected electrons slightly more effective. Thereby, despite of the insulating nature of PEIE, PEIE coated ITO acts as an efficient electron injector.

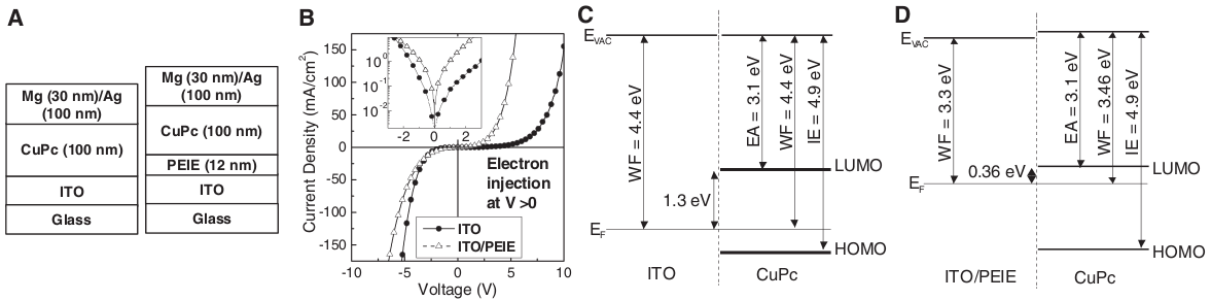

Figure 8.2: A) The structure of the OLED device with and without PEIE as bottom electrode and CuPc as the light emitting molecule. B) The measured J/V characteristics of the devices, where it is seen that with PEIE on ITO the charge injection is symmetric. The energy level alignment of CuPc on top of C) ITO and D) ITO/PEIE. [Zhou et al., 2012]

PART V

REFERENCES

References

9

Alvarado, Seidler, Lidzey, and Bradley, **1998**. SF Alvarado, PF Seidler, DG Lidzey, and DDC Bradley. *Direct determination of the exciton binding energy of conjugated polymers using a scanning tunneling microscope*. Physical review letters, 81(5), 1082, 1998.

Balkanski and Wallis, **1992**. M. Balkanski and R. F. Wallis. *Semiconductor Physics and Applications*. Oxford University Press, 1992. ISBN 978-0-19-851740-5.

Barford, **2005**. W. Barford. *Electronic and optical properties of conjugated polymers*. International series of monographs on physics. Clarendon Press, 2005. ISBN 9780198526803.

Bruetting, **2006**. W. Bruetting. *Physics of Organic Semiconductors*. John Wiley & Sons, 2006. ISBN 9783527606795.

Bruus and Flensberg, **2004**. Henrik Bruus and Karsten Flensberg. *Many-body quantum theory in condensed matter physics: an introduction*. 978-0-19-856633-6. Oxford University Press, first edition, 2004.

Cernini, Li, Spencer, Holmes, Moratti, and Friend, **1997**. R. Cernini, XC Li, GWC Spencer, AB Holmes, SC Moratti, and RH Friend. *Electrochemical and optical studies of PPV derivatives and poly (aromatic oxadiazoles)*. Synthetic metals, 84(1-3), 359–360, 1997.

Chandross, Mazumdar, Jeglinski, Wei, Vardeny, Kwock, and Miller, **1994**. M. Chandross, S. Mazumdar, S. Jeglinski, X. Wei, ZV Vardeny, EW Kwock, and TM Miller. *Excitons in poly (para-phenylenevinylene)*. Physical Review B, 50(19), 14702, 1994.

Chen and Meng, **Jul 2002**. Yi-Shiou Chen and Hsin-Fei Meng. *Intrachain carrier transport in conjugated polymer with structural and chemical defects*. Phys. Rev. B, 66, 035202, 2002. doi: 10.1103/PhysRevB.66.035202. URL `http://link.aps.org/doi/10.1103/PhysRevB.66.035202`.

Clausen, **2009**. Rolf Ask Clausen. *Philips: Nu sender vi OLED-lys på markedet*, 2009. URL `http://ing.dk/artikel/98599-philips-nu-sender-vi-oled-lys-paa-markedet`.

Dahl, **2001**. J.P. Dahl. *Introduction to the quantum world of atoms and molecules*. Introduction to the Quantum World of Atoms and Molecules. World Scientific, 2001. ISBN 9789810245658.

De Carvalho, Dos Santos, Alves, and Alves, **2003**. LC De Carvalho, CN Dos Santos, HWL Alves, and JLA Alves. *Theoretical studies of poly (para-phenylene vinylene)(PPV) and poly (para-phenylene)(PPP)*. Microelectronics journal, 34(5-8), 623–625, 2003.

Dewick, **2006**. P.M. Dewick. *Essentials of organic chemistry: for students of pharmacy, medicinal chemistry and biological chemistry*. J. Wiley, 2006. ISBN 9780470016657.

Friedrich and Schindlmayr, **2006**. C. Friedrich and A. Schindlmayr. *Many-Body Perturbation Theory: The GW Approximation*. NIC Series, 31, 335, 2006.

Hadziioannou and Malliaras, **2007**. G. Hadziioannou and G.G. Malliaras. *Semiconducting poly-*

mers: chemistry, physics and engineering. v. 1, Semiconducting Polymers: Chemistry, Physics and Engineering. Wiley-VCH, 2007. ISBN 9783527312719.

Heeger, Sariciftci, and Namdas, **2010**. A.J. Heeger, N.S. Sariciftci, and E.B. Namdas. *Semiconducting and metallic polymers*. Oxford graduate texts. Oxford University Press, 2010. ISBN 9780198528647.

Hung, Tang, and Mason, **1997**. LS Hung, CW Tang, and MG Mason. *Enhanced electron injection in organic electroluminescence devices using an Al/LiF electrode*. Applied Physics Letters, 70, 152, 1997.

Jukes, Martin, Higgins, Geoghegan, Jones, Langridge, Wehrum, and Kirchmeyer, **2004**. P.C. Jukes, S.J. Martin, A.M. Higgins, M. Geoghegan, R.A.L. Jones, S. Langridge, A. Wehrum, and S. Kirchmeyer. *Controlling the Surface Composition of Poly (3, 4-ethylene dioxythiophene)–Poly (styrene sulfonate) Blends by Heat Treatment*. Advanced Materials, 16(9-10), 807–811, 2004.

Kalinowski, **2005**. J. Kalinowski. *Organic light-emitting diodes: principles, characteristics, and processes*. Optical engineering. Marcel Dekker, 2005. ISBN 9780824759476.

Kalinowski, Picciolo, Murata, and Kafafi, **2001**. J. Kalinowski, LC Picciolo, H. Murata, and ZH Kafafi. *Effect of emitter disorder on the recombination zone and the quantum yield of organic electroluminescent diodes*. Journal of Applied Physics, 89, 1866, 2001.

Kittel, **2005**. Charles Kittel. *Introduction to Solid State Physics*. 978-0-471-41526-8. Wiley, 8^{th} edition, 2005.

Knupfer, **2003**. M. Knupfer. *Exciton binding energies in organic semiconductors*. Applied Physics A: Materials Science & Processing, 77(5), 623–626, 2003.

Kohanoff, **2006**. J. Kohanoff. *Electronic structure calculations for solids and molecules: theory and computational methods*. Condensed matter physics, nanoscience and mesoscopic physics. Cambridge University Press, 2006. ISBN 9780521815918.

Kristensen, **2008**. P.K. Kristensen. *Characterization of polymers and contacts in polymer light emitting diodes*. Department of Physics and Nanotechnology, Aalborg University, 2008. ISBN 87-89195-26-4.

Lampert and Mark, **1970**. M.A. Lampert and P. Mark. *Current injection in solids*. (Electrical science series). Academic Press, 1970. ISBN 12-435350-9.

Lane, Brewer, Huang, Bradley, et al., **2006**. P.A. Lane, P.J. Brewer, J. Huang, D.D.C. Bradley, et al. *Elimination of hole injection barriers by conducting polymer anodes in polyfluorene light-emitting diodes*. Physical Review B, 74(12), 125320, 2006.

Logdlund, Salaneck, Meyers, Brédas, Arbuckle, Friend, Holmes, and Froyer, **1993**. M. Logdlund, WR Salaneck, F. Meyers, JL Brédas, GA Arbuckle, RH Friend, AB Holmes, and G. Froyer. *Evolution of the electronic structure in a conjugated polymer series: polyacetylene, poly (p-phenylene), and poly (p-phenylenevinylene)*. Macromolecules, 26(15), 3815–3820, 1993.

Loiseau, **2006**. A. Loiseau. *Understanding carbon nanotubes: from basics to applications*. Lecture notes in physics. Springer, 2006. ISBN 9783540269229.

Lynge, **2004**. T.B. Lynge. *Tight-binding treatment of conjugated polymers*. Institute of Physics and Nanotechnology, Aalborg University, 2004. ISBN 87-89195-24-8.

Lynge and Pedersen, **Feb 2003**. Thomas Bastholm Lynge and Thomas Garm Pedersen. *Analytic expressions for linear optical susceptibilities of conjugated polymers*. Phys. Rev. B, 67, 075206, 2003. doi: 10.1103/PhysRevB.67.075206.

Malliaras and Scott, **1999**. GG Malliaras and JC Scott. *Numerical simulations of the electrical characteristics and the efficiencies of single-layer organic light emitting diodes*. Journal of applied physics, 85, 7426, 1999.

McElvain, Antoniadis, Hueschen, Miller, Roitman, Sheats, and Moon, **1996**. J. McElvain, H. Antoniadis, MR Hueschen, JN Miller, DM Roitman, JR Sheats, and RL Moon. *Formation and growth of black spots in organic light-emitting diodes*. Journal of applied physics, 80(10), 6002–6007, 1996.

Munteanu and Donescu, **2004**. L. Munteanu and S. Donescu. *Introduction to soliton theory: applications to mechanics*. Fundamental theories of physics. Kluwer Academic Publishers, 2004. ISBN 9781402025761.

Novotny and Hecht, **2006**. L. Novotny and B. Hecht. *Principles of nano-optics*. Cambridge University Press, 2006. ISBN 9780521832243.

Pedersen and Diekhöner, **2011**. Thomas Garm Pedersen and Lars Diekhöner. *Electric, Optical & Magnetic Properties Of Nanostructures*. Aalborg University, 2011.

Pope and Swenberg, **1999**. M. Pope and C.E. Swenberg. *Electronic processes in organic crystals and polymers*. Monographs on the physics and chemistry of materials. Oxford University Press, 1999. ISBN 9780195129632.

R. Saito and Dresselehaus, **1998**. G. Dresseelhaus R. Saito and M. S. Dresselehaus. *Physical Properties of Carbon Nanotubes*. 1-86094-093-5. Imperial College Press, 1998.

Schaer, Nuesch, Berner, Leo, and Zuppiroli, **2001**. M. Schaer, F. Nuesch, D. Berner, W. Leo, and L. Zuppiroli. *Water vapor and oxygen degradation mechanisms in organic light emitting diodes*. Advanced Functional Materials, 11(2), 116–121, 2001.

Su, Schrieffer, and Heeger, **Jun 1979**. W. P. Su, J. R. Schrieffer, and A. J. Heeger. *Solitons in Polyacetylene*. Phys. Rev. Lett., 42, 1698–1701, 1979. doi: 10.1103/PhysRevLett.42.1698.

Sze and Ng, **2007**. S.M. Sze and K.K. Ng. *Physics of Semiconductor Devices*. Wiley-Interscience publication. Wiley-Interscience, 2007. ISBN 9780471143239.

Wang, Puls, Staley, Zhang, Todd, Xu, Howsare, Hollander, Robinson, and Liu, **2011**. Z. Wang, C.P. Puls, N.E. Staley, Y. Zhang, A. Todd, J. Xu, C.A. Howsare, M.J. Hollander, J.A. Robinson, and Y. Liu. *Technology ready use of single layer graphene as a transparent electrode for hybrid photovoltaic devices*. Physica E: Low-dimensional Systems and Nanostructures, 2011.

Yoder, Dickerson, and Chen, **1999**. G. Yoder, BK Dickerson, and A.B. Chen. *Semiempirical method for calculating structure and band gap of semiconducting polymers*. The Journal of Chemical Physics, 111, 10347, 1999.

Yü, **1988**. L. Yü. *Solitons & polarons in conducting polymers*. World Scientific, 1988. ISBN 9789971500542.

Zhou, Fuentes-Hernandez, Shim, Meyer, Giordano, Li, Winget, Papadopoulos, Cheun, Kim,

et al., **2012**. Y. Zhou, C. Fuentes-Hernandez, J. Shim, J. Meyer, A.J. Giordano, H. Li, P. Winget, T. Papadopoulos, H. Cheun, J. Kim, et al. *A Universal Method to Produce Low–Work Function Electrodes for Organic Electronics*. Science, 336(6079), 327–332, 2012.

PART VI

APPENDICES

The sp^2 hybridisation

A

The optical and electronic properties of carbon structures are obviously connected to the electronic configuration of the carbon atoms, also known as the hybridisation of the atomic orbitals.
Carbon has electrons in the $1s^2 2s^2 2p^2$ configuration, where the inner $1s^2$ electrons are strongly bound, hence the $2s^2 2p^2$ valence electrons are important for forming chemical bonds. Due to the low energy difference between the $2p$ and the $2s$ orbitals compared to the binding energy of a covalent bond, these orbitals are readily mixed leading to a hybridisation formation of the $2s$ and the $2p$ orbitals. If a single $2s$ electron is mixed with n $2p$ electrons, where $n = 1,2,3$, a sp^n hybridisation is obtained.
tPA is sp^2 hybridised, hence the $2s$ is mixed with e.g. the $2p_x$ and $2p_y$, thus three σ-bonds are formed, each separated by an angle of 120°, leaving a weak π-bond by the $2p_z$ electron perpendicular on the tPA. The σ-bond directions of the central carbon atom in figure 2.2 are

$$(0;1;0),(\sqrt{3}/2;-1/2;0),(-\sqrt{3}/2;-1/2;0),$$

yielding the sp^2 hybridised $\left|sp^2_{a,b,c}\right\rangle$ orbital for the atom:

$$\begin{aligned}
\left|sp^2_a\right\rangle &= C_1\left|2s\right\rangle + \sqrt{1-C_1^2}\left|2p_y\right\rangle \\
\left|sp^2_b\right\rangle &= C_2\left|2s\right\rangle + \sqrt{1-C_2^2}\left(\sqrt{3}/2\left|2p_x\right\rangle - 1/2\left|2p_y\right\rangle\right) \\
\left|sp^2_c\right\rangle &= C_3\left|2s\right\rangle - \sqrt{1-C_3^2}\left(\sqrt{3}/2\left|2p_x\right\rangle + 1/2\left|2p_y\right\rangle\right).
\end{aligned}$$

The coefficients are then to be determined by the required orthonormality of the $\left|sp^2_{a,b,c}\right\rangle$, $\left|2s\right\rangle$ and $\left|2p_{x,y}\right\rangle$ wavefunctions. From the $\left|2s\right\rangle$'s part it is required that

$$C_1^2 + C_2^2 + C_3^2 = 1.$$

The orthonormality also requires, that

$$\begin{aligned}
\left\langle sp^2_a | sp^2_b \right\rangle = 0 \Rightarrow C_1 C_2 - \frac{1}{2}\sqrt{1-C_1^2}\sqrt{1-C_2^2} = 0 \\
\left\langle sp^2_a | sp^2_c \right\rangle = 0 \Rightarrow C_1 C_3 - \frac{1}{2}\sqrt{1-C_1^2}\sqrt{1-C_3^2} = 0.
\end{aligned}$$

It is thus obtained that

$$1/\sqrt{3} = C_1 = C_3 \quad \text{and} \quad -1/\sqrt{3} = C_2.$$

This linear combination reveals that the largest probability amplitude is along the direction of the nearest neighbours, describing the trigonal bindings. [R. Saito and Dresselehaus, 1998]

Tight binding approach B

In order to calculate the band structure of a conjugated polymer the tight binding approach can be used. With the tight binding approach, the inner tightly bound electrons of an atom or molecule can be modelled. The starting point is a superposition of wave functions from isolated atoms at each atomic site, from which the electronic band structure can be achieved.

Due to the lattice periodicity in crystalline solids, the electrons experience a periodic potential from the nuclei, which is assumed to be the only potential the electrons experience within the tight binding approach. The eigenfunctions $\Phi_{\vec{k}}(\vec{r})$ to the time-independent Schrödinger equation can therefore be written as single-electron orbitals on the Bloch form:

$$\Phi_{\vec{k}}(\vec{r}) = e^{i(\vec{k}\cdot\vec{r})} u_{\vec{k}}(\vec{r}), \tag{B.1}$$

where $u_{\vec{k}}(\vec{r})$ is invariant under a lattice translation and $\vec{k}$ is a reciprocal vector. An extension of equation (B.1) will then be a linear combination of atomic orbitals, $\phi_j(\vec{r})$, which satisfies the Bloch theorem and then summed over N unit cells in the lattice

$$\psi_{\vec{k},j}(\vec{r}) = N^{-1/2} \sum_{\vec{R}_j}^{N} e^{i(\vec{k}\cdot\vec{R}_j)} \phi_j(\vec{r} - \vec{R}_j), \quad j = 1, 2, ..., m \tag{B.2}$$

with $\vec{R}_j$ as the position vector for the j'th nucleus in the unit cell and m is the number of atomic wave functions in the unit cell. In principle the sum over the unit cells in equation (B.2) should be infinite but is restricted to N.

Equation (B.2) is thus a basis consisting of tight binding orbitals, where each basis function is a linear combination of atomic wave functions at the atomic sites in the lattice. Hence, any allowed quantum state of the system can be constructed by a linear combination of equation (B.2), as follows

$$\varphi_{\vec{k},n}(\vec{r}) = \sum_{j}^{m} C_{nj} \psi_{\vec{k},j}(\vec{r}).$$

The coefficients can be determined by minimising the energy. First, the energy eigenvalue of the n'th eigenstate, with $\hat{H}$ as the Hamiltonian of the system, is given as

$$E_n(\vec{k}) = \frac{\langle \varphi_n | \hat{H} | \varphi_n \rangle}{\langle \varphi_n | \varphi_n \rangle} = \frac{\sum_{j,j'}^{m} H_{j,j'}(\vec{k}) C_{nj}^* C_{nj'}}{\sum_{j,j'}^{m} S_{j,j'}(\vec{k}) C_{nj}^* C_{nj'}}, \tag{B.3}$$

where $H_{j,j'}(\vec{k}) = \langle \varphi_j | \hat{H} | \varphi_{j'} \rangle$ and $S_{j,j'}(\vec{k}) = \langle \varphi_j | \varphi_{j'} \rangle$. The minimum of $E_n(\vec{k})$ is now found:

$$\frac{\partial E_n(\vec{k})}{\partial C_{nj}^*} = \frac{\sum_{j,j'}^{m} H_{j,j'}(\vec{k}) C_{nj'}}{\sum_{j,j'}^{m} S_{j,j'}(\vec{k}) C_{nj}^* C_{nj'}} - \frac{\sum_{j,j'}^{m} H_{j,j'}(\vec{k}) C_{nj}^* C_{nj'}}{\left(\sum_{j,j'}^{m} S_{j,j'}(\vec{k}) C_{nj}^* C_{nj'} \right)^2} \sum_{j,j'}^{m} S_{j,j'}(\vec{k}) C_{nj'} = 0, \tag{B.4}$$

where by substituting equation (B.3) into equation (B.4) and rearranging, the following expression can be obtained:

$$\sum_{j,j'}^{m} H_{j,j'}(\vec{k}) C_{nj'} = E_n(\vec{k}) \sum_{j,j'}^{m} S_{j,j'}(\vec{k}) C_{nj'}. \tag{B.5}$$

Then by defining

$$\vec{C}_n = \begin{bmatrix} C_{n1} \\ \vdots \\ C_{nm} \end{bmatrix}$$

equation (B.5) gives rise to

$$\begin{aligned} \overleftrightarrow{H} \vec{C}_n &= E_n(\vec{k}) \overleftrightarrow{S} \vec{C}_n \\ &\Updownarrow \\ 0 &= \left[\overleftrightarrow{H} - E_n(\vec{k}) \overleftrightarrow{S} \right] \vec{C}_n. \end{aligned} \tag{B.6}$$

The only solution of interest to equation (B.6) is the non-trivial because otherwise there will exist an inverse matrix, which multiplied to equation (B.6) leads to $C_n = 0$. Therefore in order to determine the coefficients C_n, the secular equation must be solved:

$$\det \left| \overleftrightarrow{H} - E \overleftrightarrow{S} \right| = 0, \tag{B.7}$$

which is a polynomial of the m'th order. By solving equation (B.7) the lowest energy is found, which can then be substituted into equation (B.6) to find the coefficients C_n, corresponding to the ground state of the system. [R. Saito and Dresselehaus, 1998]

Density-functional theory

C

To describe the electronic structure of a given many-body system density-functional theory (DFT) focusses on the electron density rather than the wave function. This approach is essentially a ground-state approach because it relies on the variational theorem. However, with the so-called GW-approximation[1] it is possible to modulate the excited state of a system with fairly good accuracy, all described later in this appendix.

C.1 Reduced density matrices

Within the Adiabatic approximation the Haliltonian for the electronic wave equation can, in atomic units, for an N electron and P atom system be written as

$$\hat{H} = -\sum_{i=1}^{N} \frac{\nabla_i^2}{2} + \frac{1}{2}\sum_{i=1}^{N}\sum_{j=1}^{N} \frac{1}{|\vec{r}_i - \vec{r}_j|} - \sum_{I=1}^{P}\sum_{i=1}^{N} \frac{Z_I}{|\vec{R}_I - \vec{r}_i|},$$

where $\vec{R} = \{\vec{R}_i, i = 1,..,P\}$ are nuclear coordinates, $\vec{r} = \{\vec{r}_i, i = 1,..,N\}$ are electronic coordinates and Z_I is the nuclear charge of atom I.
By introducing a single-particle spin-free wave function as $\varphi(\vec{r})$ the probability density in position space may be written as

$$\rho(\vec{r}) = \varphi(\vec{r})\varphi^*(\vec{r}),$$

which will be referred to as the electron density. In order to determine the expectation value of the electrostatic potential due to the nuclei it is sufficient to know the electron density, but due to the Laplace operator in the momentum operator it is not enough to know the electron density to evaluate the kinetic energy. Therefore the so-called density matrix is introduced as

$$\rho(\vec{r},\vec{r}') = \varphi(\vec{r})\varphi^*(\vec{r}'),$$

which is equivalent to the wave function itself. The electron density is now defined through the diagonal elements of the density matrix.
Now, consider a system of N electrons in a state described by the wave function $\Psi(x_1, x_2, ..., x_N)$, with

[1] The GW-approximation is not a DFT approach but uses an initial guess to the excited states obtained by DFT.

$x = (\vec{r}, \varsigma)$ where the spin dependence lies in ς, and the operators

$$\hat{F} = \sum_{i=1}^{N} \hat{f}(x_i)$$

and

$$\hat{G} = \frac{1}{2} \sum_{i=1}^{N} \sum_{j=1}^{N} {}' \hat{g}(x_i, x_j)$$

are the sums of one- and two-electron operators, respectively. The expectation values of $\hat{F}$ for a general N-electron wave function is now derived by noting that each $\hat{f}(x_i)$ contributes equally to $\langle \Psi | \hat{F} | \Psi \rangle$. It is given that

$$\begin{aligned}
&\int \Psi^*(x_1, x_2, ..., x_N) \hat{f}(x_2) \Psi(x_1, x_2, ..., x_N) dx_1 dx_2 ... dx_N = \\
&\int \Psi^*(x_2, x_1, ..., x_N) \hat{f}(x_1) \Psi(x_2, x_1, ..., x_N) dx_1 dx_2 ... dx_N = \\
&\int \Psi^*(x_1, x_2, ..., x_N) \hat{f}(x_1) \Psi(x_1, x_2, ..., x_N) dx_1 dx_2 ... dx_N
\end{aligned}$$

because both Ψ and Ψ^* changes sign by interchange the particles 1 and 2. Therefore

$$\langle \Psi | \hat{F} | \Psi \rangle = N \int \Psi^*(x_1, x_2, ..., x_N) \hat{f}(x_1) \Psi(x_1, x_2, ..., x_N) dx_1 dx_2 ... dx_N.$$

Then, by defining the reduced one-electron density matrix as

$$\gamma(x, x') = N \int \Psi(x, x_2, ..., x_N) \Psi^*(x', x_2, ..., x_N) dx_1 dx_2 ... dx_N,$$

enables

$$\langle \Psi | \hat{F} | \Psi \rangle = \int [\hat{f}(\vec{r}) \gamma(x, x')]_{x'=x} dx.$$

Furthermore, if $\hat{f}$ is independent of spin, an integration over the spin variable can be conducted to get

$$\langle \Psi | \hat{F} | \Psi \rangle = \int [\hat{f}(x) \rho(\vec{r}, \vec{r}')]_{\vec{r}'=\vec{r}} dv,$$

where

$$\rho(\vec{r}, \vec{r}') = \int [\gamma(x, x')]_{\varsigma'=\varsigma} d\varsigma$$

is the so-called spinless one-electron density matrix, whose diagonal elements yields the electron density $\rho(\vec{r})$. Following the same procedure as for the $\hat{F}$ operator the expectation value for the $\hat{G}$ operator can be written as

$$\langle \Psi | \hat{G} | \Psi \rangle = \int [\hat{g}(x_1, x_2) \Gamma(x_1, x_2, x_1', x_2'),]_{x_1'=x_1, x_2'=x_2} dx_1 dx_2. \tag{C.1}$$

with

$$\Gamma(x_1,x_2,x_1',x_2') = \frac{N(N-1)}{2}\int \Psi(x_1,x_2,...,x_N)\Psi^*(x_1',x_2',x_3,...,x_N)dx_3dx_4...dx_N$$

as the reduced two-electron density matrix. The only expression needed for equation (C.1) is when $\hat{g}(x_1,x_2) = \frac{1}{r_{12}}$, where r_{12} is the distance between the two electrons. $\hat{G}$ is then the operator for the electron-electron repulsion energy given as

$$\hat{G} = \frac{1}{2}\sum_{i=1}^{N}\sum_{j=1}^{N}{}' \frac{1}{r_{12}}.$$

For spin independence equation (C.1) simplifies to

$$\langle\Psi|\hat{G}|\Psi\rangle = \int \frac{1}{r_{12}}\rho_2(\vec{r}_1,\vec{r}_2)dv_1dv_2$$

with

$$\rho_2(\vec{r}_1,\vec{r}_2) = \int \Gamma(x_1,x_2,x_1,x_2)d\varsigma_1d\varsigma_2$$

as the two-electron density, which is normalised to the number of electron pairs $\frac{N(N-1)}{2}$, and is the diagonal elements of the spinless two-electron density matrix.
[Dahl, 2001]

C.2 The Hohenberg-Kohn theorems

Within the Born-Oppenheimer approximation the Hamiltonian of the electronic wave function is given by

$$\hat{H} = \hat{T} + \hat{V}_{ext} + \hat{U}_{ee},$$

where $\hat{T}$ and $\hat{U}_{ee}$ is the kinetic energy operator for the electrons and the operator for the electron-electron interaction, respectively, whereas $\hat{V}_{ext}$ is the operator of an external potential, which could represent electron-nuclear interaction.

C.2.1 The first theorem

The external potential is, besides a trivial additive constant, univocally determined by the ground-state electron density $\rho_0(\vec{r})$.

This theorem is fundamental for DFT. That $\rho_0(\vec{r})$ can be determined from the external potential by solving the many-body Schrödinger equation is quite obvious, whereas the other way around is an important building block for using the DFT approach.

To prove this theorem, two N-electron Hamiltonians with two different external potentials, which differ by more than just a zero-point displacement, is constructed. These shall be denoted as $\hat{H}$ and $\hat{H}'$ for which the following applies:

$$\hat{H} - \hat{H}' = \sum_{i=1}^{N} [\hat{V}_{ext}(\vec{r}_i) - \hat{V}'_{ext}(\vec{r}_i)]$$

Assuming non-degenerate ground states corresponding to $\hat{H}$ and $\hat{H}'$ given by the normalised ground-state wave functions denoted Φ and Φ' with the ground-state energies E_0 and E'_0[2], the variational theorem leads to

$$E_0 < \langle \Phi' | \hat{H} | \Phi' \rangle = \langle \Phi' | \hat{H} | \Phi' \rangle + \langle \Phi' | \hat{H} - \hat{H}' | \Phi' \rangle = E'_0 + \int \rho_0(\vec{r}) [\hat{V}_{ext}(\vec{r}) - \hat{V}'_{ext}(\vec{r})] d\vec{r} \tag{C.2}$$

and

$$E'_0 < \langle \Phi | \hat{H}' | \Phi \rangle = \langle \Phi | \hat{H}' | \Phi \rangle - \langle \Phi | \hat{H} - \hat{H}' | \Phi \rangle = E_0 - \int \rho_0(\vec{r}) [\hat{V}_{ext}(\vec{r}) - \hat{V}'_{ext}(\vec{r})] d\vec{r}. \tag{C.3}$$

Adding equation (C.2) and (C.3) leads to the contradiction $E_0 + E'_0 < E_0 + E'_0$. Therefore, it is not possible to have $v_{ext}(\vec{r}) \neq v'_{ext}(\vec{r})$ that correspond to the same electron density for the ground state, unless they differ by an trivial additive constant.
[Kohanoff, 2006]

C.2.2 The second theorem

With the ground state electron density $\rho_0(\vec{r}) \geq 0$ and normalised to N, it is possible to find the ground state electron density by applying the variational theorem on the energy functional $E[\rho]$. [3]

Introducing the variational energy $E_v[\rho]$ as

$$E_v[\rho] = F[\rho] + \int \rho(\vec{r}) \hat{V}_{ext}(\vec{r}) d\vec{r}, \quad F[\rho] = \langle \Phi[\rho] | \hat{T} + \hat{U}_{ee} | \Phi[\rho] \rangle, \tag{C.4}$$

where $\Phi[\rho_0]$ is the ground-state many-body wave equation of a potential with ρ_0 as the ground-state density, so according to the variational principle it follows that the ground-state energy

$$E_0 = E[\rho_0] \leq E[\rho].$$

The starting point for this proof is that

$$\langle \Phi[\rho] | \hat{H} | \Phi[\rho] \rangle = F[\rho] + \int \rho(\vec{r}) \hat{V}_{ext}(\vec{r}) d\vec{r} = E_v[\rho] \geq E_v[\rho_0] = \langle \Phi[\rho_0] | \hat{H} | \Phi, [\rho_0] \rangle$$

[2] The theorem can be generalised to degenerate ground-states.

[3] A functional can loosely be said to be a function of a function but in principle a functional is a way to map a number into a function. The differential of a functional e.g. $E[\rho]$ can be written as $\delta E[\rho] = \int \frac{\delta E[\rho]}{\delta \rho(\vec{r})} \delta\rho(\vec{r}) d\vec{r}$, where $\delta E[\rho]/\delta\rho(\vec{r})$ is called the functional derivative of $E[\rho]$. [Dahl, 2001]

which can be recognised as the variational principle applied on the electron density. Furthermore, varying $E[\rho]$ with respect to ρ leads to

$$\begin{aligned}\delta\left(E_v[\rho]-\mu\left(\int\rho(\vec{r})d\vec{r}-N\right)\right)=&\delta\left(\int\rho(\vec{r})\hat{V}_{ext}(\vec{r})d\vec{r}\right)+\delta\left(F[\rho]\right)-\mu\delta\left(\int\rho(\vec{r})d\vec{r}\right)=0\\ &\Downarrow\\ 0=&\int\left(\hat{V}_{ext}(\vec{r})+\frac{\delta F[\rho]}{\delta\rho(\vec{r})}-\mu\right)\delta\rho(\vec{r})d\vec{r}.\end{aligned}\tag{C.5}$$

For equation (C.5) to be true for all $\delta\rho(\vec{r})$ the following must apply:

$$\mu=\frac{\delta E_v[\rho]}{\delta\rho(\vec{r})}=\hat{V}_{ext}(\vec{r})+\frac{\delta F[\rho]}{\delta\rho(\vec{r})},$$

where the Lagrange multiplier, by inspiration from thermodynamic terminology, μ is called the chemical potential. Thus, if the functional $E[\rho]$ is know it is possible to find ρ_0. Because $F[\rho]$ do not explicit depend on the external potential it is a so-called universal functional, that only depends on the electron density.

The two Hohenberg-Kohn theorems thus form the mathematical basis for DFT but they do, however not, give a prescription for evaluating $E[\rho_0]$.

[Kohanoff, 2006]

C.3 The Kohn-Sham equations

The main difficulty of solving the many-body Schrödinger equation lies within the electron-electron interaction, where a decent approach has been to divide these interactions into a Coulomb interaction, the so-called Hartree term, which has the largest contribution to the exchange interaction and a correlation term, which by far is the biggest difficulty and is therefore often ignored because it displays a quite small contribution.

The evaluation of the kinetic energy then holds the next challenge because the Laplacian requires a one-body matrix. However, as suggested by Kohn and Sham (1965), using a Slater determinant constructed by one-electron orbitals for the many-body wave function offered a way around this problem. The ground-state electron density matrix will then be given by

$$\rho_0(\vec{r},\vec{r}')=\sum_{i=1}^{N}f_i\varphi_i(\vec{r})\varphi_i^*(\vec{r}'),$$

where f_i is the occupation number of the i'th one-electron orbital $\varphi_i(\vec{r})$ and N is the number of electrons. The kinetic energy of a Slater determinant is

$$T = -\frac{\hbar^2}{2m}\sum_{i=1}^{N} f_i \left\langle \varphi_i(\vec{r})|\nabla^2|\varphi_i(\vec{r})\right\rangle .$$

So, by assuming, that a system of non-interacting electrons whose ground-state density coincides with that of an interacting system do exist, a non-interacting reference system with a density $\rho(\vec{r})$ can be described by following Hamiltonian:

$$\hat{H}_R = \sum_{i=1}^{N}\left[-\frac{\hbar^2}{2m}\nabla_i^2 + v_R(\vec{r}_i)\right],$$

where the reference potential $v_R(\vec{r})$ is given in such a way, that ground-state of $\hat{H}_R$ equals $\rho(\vec{r})$, because then, according to the Hohenberg-Kohn theorems, the energy of the non-interacting system is the same as for the interacting system. With this Hamiltonian the eigenstates can be given as the Slater determinant

$$\Phi(\vec{r}) = \sqrt{\frac{1}{N!}}\begin{vmatrix} \varphi_1(\vec{r}_1) & \varphi_1(\vec{r}_2) & \dots & \varphi_1(\vec{r}_N) \\ \varphi_2(\vec{r}_1) & \varphi_2(\vec{r}_2) & \dots & \varphi_2(\vec{r}_N) \\ \vdots & \vdots & \ddots & \vdots \\ \varphi_N(\vec{r}_1) & \varphi_N(\vec{r}_2) & \dots & \varphi_N(\vec{r}_N) \end{vmatrix},$$

with $\varphi_i(\vec{r}_j)$ as spin-orbitals [4]. To keep the notation intuitive the spin variable will not be written explicit. Within this approximation the exact one electron density can be obtained from the diagonal elements of the matrix right above. Hence,

$$\rho(\vec{r}) = \sum_{i=1}^{N}|\varphi_i(\vec{r})|^2. \tag{C.6}$$

The orbitals $\varphi_i(\vec{r})$, also known as the Kohn-Sham orbitals, are the N lowest-energy eigenfunctions to the one-electron Hamiltonian $\hat{H}_{KS}$ and found by solving the following one-electron Schrödinger equation:

$$\hat{H}_{KS}\varphi_i(\vec{r}) = \varepsilon_i\varphi_i(\vec{r}), \quad \hat{H}_{KS} = \left[-\frac{\hbar^2}{2m}\nabla_i^2 + v_R(\vec{r}_i)\right]. \tag{C.7}$$

These sets of equations are known as the Kohn-Sham equations and by introducing the universal density functional as

$$F[\rho] = \underbrace{-\frac{\hbar^2}{2m}\sum_{i=1}^{N}\left\langle \varphi_i(\vec{r})|\nabla^2|\varphi_i(\vec{r}\right\rangle}_{T_R[\rho]} + \underbrace{\frac{1}{2}\int\int\frac{\rho(\vec{r})\rho(\vec{r}')}{|\vec{r}-\vec{r}'|}d\vec{r}d\vec{r}'}_{V_H[\rho]} + \tilde{E}_{XC}[\rho],$$

[4] A spin-orbital $\varphi(x)$, where $x = (\vec{r},\varsigma)$ has the spin dependence in ς with the orthogonal spin functions $\alpha(\varsigma)$ and $\beta(\varsigma)$ as a basis. Hence $\varphi(\vec{r},\varsigma) = \psi_1(\vec{r})\alpha(\varsigma) + \psi_2(\vec{r})\beta(\varsigma)$, where $|\psi_1|^2dv$ is the probability of finding the electron in the volume element dv at $\vec{r}$, with the z-projection of the spin as $\hbar/2$ and $|\psi_2|^2dv$ is the probability of finding the electron in the volume element dv at $\vec{r}$, with the z-projection of the spin as $-\hbar/2$. [Dahl, 2001]

with $\tilde{E}_{XC}$ as the exchange-correlation energy, the Kohn-Sham functional, obtained from equation (C.4), reads[5]

$$\begin{aligned} E_{KS}[\rho] &= T_R[\rho] + V_R[\rho] \\ &= -\frac{\hbar^2}{2m}\sum_{i=1}^{N}\left\langle \varphi_i(\vec{r})|\nabla^2|\varphi_i(\vec{r})\right\rangle + \int \hat{V}_{ext}\rho(\vec{r})d\vec{r} + \frac{1}{2}\int\int \frac{\rho(\vec{r})\rho(\vec{r}')}{|\vec{r}-\vec{r}'|}d\vec{r}d\vec{r}' + \tilde{E}_{XC}. \end{aligned}$$

To obtain the Kohn-Sham orbitals, that satisfies equation (C.7), the reference potential is needed, which can be determined by a minimisation of the Kohn-Sham functional with respect to the electron density with the restriction that this density must be normalised to N electrons. Thus,

$$\begin{gathered} \frac{\delta}{\delta\rho(\vec{r})}\left(E_{KS}[\rho] - \mu\int \rho(\vec{r})d\vec{r}\right) = 0 \\ \Downarrow \\ \frac{\delta T_R[\rho]}{\delta\rho(\vec{r})} + \hat{V}_{ext} + \int \frac{\rho(\vec{r}')}{|\vec{r}-\vec{r}'|}d\vec{r}' + \frac{\delta\tilde{E}_{XC}[\rho]}{\delta\rho(\vec{r})} = \mu. \end{gathered} \tag{C.8}$$

Since the electrons in the reference system do not interact with each other but only with the reference potential, the Hamiltonian $\hat{H}_R$ corresponds to the following energy functional:

$$E_{V_R}[\rho_0] = T_R[\rho_0] + \int \rho_0(\vec{r})v_R(\vec{r})d\vec{r},$$

whose ground-state energy is the same as the interacting system due to the same electron density. The equality $E_{V_R}[\rho_0] \geq E_0$ is then only verified for the ground-state density leading to a vanishing functional derivative of $E_{V_R}[\rho_0]$ for the ground-state state density. Applying, yet again, the variational principle to $E_{V_R}[\rho_0]$ yields

$$\frac{\delta T_R[\rho]}{\delta\rho(\vec{r})} + v_R(\vec{r}) = \mu_R, \tag{C.9}$$

with the chemical potential of the reference system μ_R equal to that of the interacting system. Combining equation (C.8) and (C.9) enables the reference potential to be written as

$$v_R(\vec{r}) = \hat{V}_{ext} + \int \frac{\rho(\vec{r}')}{|\vec{r}-\vec{r}'|}d\vec{r}' + \mu_{XC}[\rho](\vec{r}), \quad \mu_{XC}[\rho](\vec{r}) = \frac{\delta\tilde{E}_{XC}[\rho]}{\delta\rho(\vec{r})}.$$

In order find the reference potential the Kohn-Sham orbitals must be obtained, through the electron density. Therefore these sets of equations must be solved self-consistently, making sure that equation (C.6) is obeyed.
[Kohanoff, 2006]

[5] The Hartree term V_H includes the interaction of the electron with itself, which is unphysical, but this can be corrected as explained in section C.3.1.

C.3.1 The exchange-correlation hole

It is desirable to interpret the exchange-correlation energy as a Coulomb interaction between the electron charge density and some displaced charge density, which can be done by defining the exchange-correlation hole as

$$\tilde{\rho}_{XC}(\vec{r},\vec{r}') = \rho(\vec{r}')[\tilde{g}(\vec{r},\vec{r}') - 1], \tag{C.10}$$

in order to write the exchange-correlation energy as

$$\tilde{E}_{XC}[\rho] = \frac{1}{2}\int\int \frac{\tilde{\rho}_{XC}(\vec{r},\vec{r}')\rho(\vec{r})}{|\vec{r}-\vec{r}'|} d\vec{r}d\vec{r}',$$

where if the pair correlation function $\tilde{g}(\vec{r},\vec{r}') = 1$ it amounts to uncorrelated electrons.
The exchange-correlation hole can thus be described by means of a fictitious charge depletion and corrects for the fact, that the Hartree contribution to the energy ignores that an electron around $\vec{r}$ reduces the probability of finding another electron around $\vec{r}$.
The implementation of equation (C.10) leads to some instructive properties of $\tilde{g}(\vec{r},\vec{r}')$ and $\tilde{\rho}_{XC}(\vec{r},\vec{r}')$, also known as the sum rules. First of all $\tilde{g}$ must be symmetric so that $\tilde{g}(\vec{r},\vec{r}') = \tilde{g}(\vec{r}',\vec{r})$. Second, the normalisation condition

$$\int \tilde{g}(\vec{r}',\vec{r})\rho(\vec{r}')d\vec{r}' = \int \tilde{g}(\vec{r},\vec{r}')\rho(\vec{r})d\vec{r} = N-1$$

must apply. Third,

$$\int \tilde{\rho}_{XC}(\vec{r},\vec{r}')d\vec{r}' = \int \tilde{\rho}_{XC}(\vec{r}',\vec{r})d\vec{r} = -1, \tag{C.11}$$

which means that the exchange-correlation hole only contains one displaced electron. That is, if one electron is at $\vec{r}$ then the remaining amount of electrons in all other space is $N-1$. Another important issue regarding equation (C.11) is the role of exchange. Equation (C.11) ensures that the self-interaction term from the Hartree term is cancelled out. [Kohanoff, 2006]

C.3.2 The adiabatic connection

The exact theory described above needs to be connected to the fully interacting system and therefore it must be investigated how good an approximation $T_R[\rho]$ is to $T[\rho]$ and how the exchange-correlation energy can take the correlation in the non-interacting system into account.
The non-interacting $T_R[\rho]$ contains no explicit electron-electron interaction[6], whereas $T[\rho]$ does. This leads, due to variational reasons, to $T_R[\rho] < T[\rho]$ meaning that the correlation term must contains a positive contribution caused by the kinetic correlation given by Pauli's principle. The error introduced by estimating the kinetic energy by a Slater determinant will then be included in the exchange-correlation

[6]The electron-electron interaction in form of the self-consistent dependence is included, though.

term, so the term is now

$$\tilde{E}_{XC} = T - T_R + E_{XC}.$$

This kinetic contribution introduces the adiabatic connection, with the idea being a gradual switch from the non-interacting system to the fully interacting system. To do this, a switching parameter λ is introduced that multiplies the interaction term in the full Hamiltonian

$$\hat{H}_\lambda = \hat{T}[\rho] + \hat{V}_{ext}[\rho] + \lambda \hat{U}_{ee}[\rho],$$

where $\lambda = 0$ corresponds to the non-interacting system and $\lambda = 1$ corresponds to the fully interacting system and the switching is done in such a way that the electron density is always the same.
By defining the ground-state wave function for a given λ by Φ_λ, the ground-state energy can be written as

$$E_\lambda = \langle \Phi_\lambda | \hat{T} | \Phi_\lambda \rangle + \langle \Phi_\lambda | \lambda \hat{V} | \Phi_\lambda \rangle + \int V_\lambda \rho_0(\vec{r}) d\vec{r}, \tag{C.12}$$

where $V_{\lambda=0} = V_R$ and $V_{\lambda=1} = V_{ext}$. Furthermore,

$$\begin{aligned} \frac{dE_\lambda}{d\lambda} =& \left\langle \frac{d\Phi_\lambda}{d\lambda} | \hat{H} | \Phi_\lambda \right\rangle + \langle \Phi_\lambda | \frac{d\hat{H}}{d\lambda} | \Phi_\lambda \rangle + \left\langle \Phi_\lambda | \hat{H} | \frac{d\Phi_\lambda}{d\lambda} \right\rangle \\ =& E_\lambda \frac{d}{d\lambda} \langle \Phi_\lambda | \Phi_\lambda \rangle + \langle \Phi_\lambda | \frac{d\hat{H}}{d\lambda} | \Phi_\lambda \rangle = \langle \Phi_\lambda | \frac{d\hat{H}}{d\lambda} | \Phi_\lambda \rangle, \end{aligned}$$

which is known as the Hellmann-Feynman theorem and applying it to equation (C.12) yields

$$\frac{dE_\lambda}{d\lambda} = \langle \Phi_\lambda | \hat{V}_H | \Phi_\lambda \rangle + \int \frac{dV_\lambda}{d\lambda} \rho_0(\vec{r}) d\vec{r},$$

after which an integration over λ leads to

$$E_{\lambda=1} = E_{\lambda=0} + \int_0^1 \langle \Phi_\lambda | \hat{V}_H | \Phi_\lambda \rangle d\lambda + \int [V_{ext} - V_R] \rho_0(\vec{r}) d\vec{r}.$$

The reference potential can be eliminated by the fact that $E_{\lambda=0} = T_R[\rho_0] + \int V_R(\vec{r}) \rho_0(\vec{r}) d\vec{r}$ and $E_{\lambda=1} = F[\rho_0] + \int V_{ext}(\vec{r}) \rho_0(\vec{r}) d\vec{r}$. Hence,

$$F[\rho_0] = T_R[\rho_0] + \int_0^1 \langle \Phi_\lambda | \hat{V}_H | \Phi_\lambda \rangle d\lambda = T_R[\rho_0] + V_H[\rho] + \frac{1}{2} \int_0^1 \left[\int \int \frac{\rho_0(\vec{r}) \rho_0(\vec{r}')}{|\vec{r} - \vec{r}'|} d\vec{r} d\vec{r}' \right] d\lambda$$

By introducing the average exchange-correlation pair correlation function $\tilde{g} = \int_0^1 g_\lambda d\lambda$ is can thus be concluded that the exchange-correlation energy in the Kohn-Sham system equals the Coulomb energy of the coupling-constant averaged pair-distribution:

$$\tilde{E}_{XC} = \frac{1}{2} \int \int \frac{\tilde{\rho}_{XC}}{|\vec{r} - \vec{r}'|} d\vec{r} d\vec{r}', \quad \tilde{\rho}_{XC} = \rho_0(\vec{r}) \rho_0(\vec{r}') [\tilde{g}(\vec{r}, \vec{r}') - 1]$$

which takes the kinetic correlations into account because $\tilde{\rho}_{XC}$ is the exchange-correlation hole average of the strength of interaction. [Kohanoff, 2006]

C.3.3 Approximations to the exhange-correlation functional

For DFT to be of any practical use an expression for the exchange-correlation functional is needed but it has not been achieved to obtain an exact expression. The task is then to find appropriate approximations for $\tilde{E}_{XC}[\rho]$ or the exchange-correlation potential $\mu_{XC}[\rho](\vec{r})$.

Local approximations

One of the most commonly used approximations is the so-called local density approximation (LDA), where the local exchange-correlation energy per electron is assumed to be that of a uniform electron gas with the local electron density from which the exchange-correlation functional can be written as

$$\tilde{E}_{XC}^{LDA}[\rho] = \int \rho(\vec{r})\tilde{\varepsilon}_{XC}^{LDA}(\rho(\vec{r}))d\vec{r},$$

where the exchange-correlation energy per electron in a uniform electron density is weighted with the electron density of the given system. From the exchange-correlation hole it is thus given that

$$\tilde{\varepsilon}_{XC}^{LDA} = \frac{1}{2}\int\int \frac{\tilde{\rho}_{XC}^{LDA}(\vec{r},\vec{r}')}{|\vec{r}-\vec{r}'|}d\vec{r}'.$$

An extension of the local density approximation is the local spin density approximation, which is a better fit for magnetic and open shell systems:

$$E_{XC}^{LSDA}[\rho] = \int \rho(\vec{r})\varepsilon_{XC}^{LSDA}(\rho_{\uparrow}(\vec{r}),\rho_{\downarrow}(\vec{r}))d\vec{r}.$$

The LDA approach s obviously only a perfect fit for systems with a homogeneous electron gas but to address the issue of inhomogeneous electron gases a quite forward approach is to expand the electron density in terms of the gradient and possibly terms of higher order. It turns out that this approach easily violates the sum rules and therefore a generalised gradient approximation (GGA) has been constructed, which assumes that ε_{XC}^{GGA} is a function of the electron density and its gradient, avoiding a gradient expansion of ε_{XC}^{GGA}. The GGA is thus given as

$$E_{XC}^{GGA}[\rho] = \int \rho(\vec{r})\varepsilon_{XC}^{GGA}(\rho(\vec{r}),\nabla\rho(\vec{r}))d\vec{r}.$$

The local approximations described mostly apply to the ground-state in metals and are therefore not a proper approach for evaluating the electronic band structure of semiconductors. More sophisticated approximations are thus needed. [Kohanoff, 2006]

C.4 Green's function approach: the GW-approximation

The starting point of solving an equation by the use of Green's function is by having an equation on the following form:

$$\mathcal{L}A(\vec{r}) = B(\vec{r}), \tag{C.13}$$

where $\mathcal{L}$ is a linear operator acting on $A(\vec{r})$. When equation (C.13) is too difficult to solve one can attend an equation with the special inhomogeneity $\delta(\vec{r}-\vec{r}')$, as follows

$$\mathcal{L}G(\vec{r},\vec{r}') = \delta(\vec{r}-\vec{r}'). \tag{C.14}$$

Now, if it is assumed that $G(\vec{r},\vec{r}')$ is known, then by multiplying equation (C.14) with $B(\vec{r}')$ and integrating over $\vec{r}'$, where $B \neq 0$, yields

$$\int \mathcal{L}G(\vec{r},\vec{r}')B(\vec{r}')d\vec{r}' = \int B(\vec{r}')\delta(\vec{r}-\vec{r}')d\vec{r}' = B(\vec{r}) = \mathcal{L}A(\vec{r}), \tag{C.15}$$

where the functions $G(\vec{r},\vec{r}')$ that obeys equation (C.15) are known as Green's functions. Assuming that the operator can be taken out of the integral it is then obtained that

$$A(\vec{r}) = \int G(\vec{r},\vec{r}')B(\vec{r}')d\vec{r}'.$$

Define the Greens function $G^e(\vec{r}t,\vec{r}'t')$ so that $i\hbar G^e(\vec{r}t,\vec{r}'t')$ is the probability amplitude for the propagation of an additional electron from $\vec{r}t$ to $\vec{r}'t'$ for a many-body electron system and adapt the field operators $\hat{\psi}(\vec{r})$ and $\hat{\psi}^\dagger(\vec{r})$ for the description of annihilation and creation of an electron at the position $\vec{r}$, respectively. The propagation process thus brings the N-electron system from the ground state $|\Psi_0(t')\rangle$ to a final state $\hat{\psi}(\vec{r})\hat{U}(t,t')\hat{\psi}^\dagger(\vec{r})\,|\Psi_0(t')\rangle$, with the evolution operator $\hat{U}(t,t') = e^{-i\hat{H}(t-t')/\hbar}$, where $t > t'$. The Greens function thereby becomes

$$\begin{aligned} G^e(\vec{r}t,\vec{r}'t') &= -\frac{i}{\hbar}\left\langle \Psi_0^N(t)\right|\hat{\psi}(\vec{r})\hat{U}(t,t')\hat{\psi}^\dagger(\vec{r}')\left|\Psi_0^N(t')\right\rangle\theta(t-t') \\ &= -\frac{i}{\hbar}\left\langle \Psi_0^N\right|\hat{\psi}(\vec{r}t)\hat{\psi}^\dagger(\vec{r}'t')\left|\Psi_0^N\right\rangle\theta(t-t'), \end{aligned} \tag{C.16}$$

where $\theta(t-t')$ is the Heaviside step function. The top part of equation (C.16) states the Green function in the Schrödinger picture[7], whereas the last part is stated in the Heisenberg picture[8].[9] The Green function

[7] The Schrödinger picture is appealing for systems with a time-independent Hamiltonian. Any other operator $\hat{A}$ may or may not be time-dependent. The state vectors do depend on time, which is governed by the Schrödinger equation. This leads to: $i\hbar\frac{\partial|\psi(t)\rangle}{\partial t} = \hat{H}|\psi(t)\rangle \Rightarrow |\psi(t)\rangle = e^{-\frac{i}{\hbar}\hat{H}t}|\psi_0\rangle$. [Bruus and Flensberg, 2004]

[8] The Heisenberg picture is to favour when all time dependence can be transferred to the operators, $\hat{A}(t)$, leaving the state vectors $|\psi_0\rangle$ time-independent. However, the Hamiltonian remains time-dependent. Hence, $\langle\psi'(t)|\hat{A}|\psi(t)\rangle = \langle\psi'_0|e^{\frac{i}{\hbar}t}\hat{A}e^{-\frac{i}{\hbar}t}|\psi_0\rangle \equiv \langle\psi'|\hat{A}(t)|\psi\rangle$. [Bruus and Flensberg, 2004]

[9] States and operators are in those two pictures related by $|\Psi_H\rangle = \hat{U}(0,t)\,|\Psi_S\rangle$ and $\hat{A}_H(t) = \hat{U}(0,t)\hat{A}_S(t)\hat{U}(0,t)$. It can be noticed that if the matrix elements of any operator between any states are the same, the two representations are equivalent.

for the propagation of an additional hole from $\vec{r}t$ to $\vec{r}'t'$ is given by

$$G^h(\vec{r}t,\vec{r}'t') = -\frac{i}{\hbar}\left\langle \Psi_0^N \middle| \hat{\psi}^\dagger(\vec{r}'t')\hat{\psi}(\vec{r}t) \middle| \Psi_0^N \right\rangle \theta(t'-t). \tag{C.17}$$

For convenience equation (C.16) and (C.17) is combined in one time ordered Green function as follows

$$G(\vec{r}t,\vec{r}'t') = G^e(\vec{r}t,\vec{r}'t') - G^h(\vec{r}t,\vec{r}'t') = -\frac{i}{\hbar}\left\langle \Psi_0^N \middle| \hat{T}\left[\hat{\psi}(\vec{r}t)\hat{\psi}^\dagger(\vec{r}'t')\right] \middle| \Psi_0^N \right\rangle, \tag{C.18}$$

where $\hat{T}$ is a time-ordering operator, that rearrange field operators in the order of rising time arguments from left to right with a factor of -1 for each pair permutation. Hence, equation (C.18) describes electron propagation if $t > t'$ or hole propagation if $t < t'$. Furthermore, the electron density can now be expressed using the Green function as

$$\rho(\vec{r}t) = \left\langle \Psi_0^N \middle| \hat{\psi}^\dagger(\vec{r}t)\hat{\psi}(\vec{r}'t') \middle| \Psi_0^N \right\rangle = -i\hbar G(\vec{r}t,\vec{r}t+\eta),$$

with η as an infinitesimal positive number, which enforces the correct order of the field operators.
Now, consider the time-ordered Green function of a stationary system $G(\vec{r},\vec{r}';\tau)$, where $\tau = t - t'$. Applying the closure relation $\sum_i \left|\Psi_i^{N\pm1}\right\rangle\left\langle\Psi_i^{N\pm1}\right| = 1$ to equation (C.18) with $\left|\Psi_i^{N\pm1}\right\rangle$ as a complete set of state vectors of the $N\pm1$-electron system. Utilising the Schrödinger picture and the definitions

$$\psi_i^{N-1}(\vec{r}) = \left\langle \Psi_i^{N-1} \middle| \hat{\psi}(\vec{r}) \middle| \Psi_0^N \right\rangle \quad \text{and} \quad \psi_i^{N+1}(\vec{r}) = \left\langle \Psi_0^N \middle| \hat{\psi}(\vec{r}) \middle| \Psi_i^{N+1} \right\rangle$$

with the excitation energies

$$\varepsilon_i^{N-1} = E_0^N - E_i^{N-1} \quad \text{and} \quad \varepsilon_i^{N+1} = E_i^{N+1} - E_0^N$$

the Green function can be written as

$$G(\vec{r}t,\vec{r};\tau) = -\frac{i}{\hbar}\sum_i \psi_i^{N+1}(\vec{r})\psi_i^{N+1}(\vec{r}')e^{-i\varepsilon_i^{N+1}\tau/\hbar}\theta(\tau) + \frac{i}{\hbar}\sum_i \psi_i^{N-1}(\vec{r})\psi_i^{N-1}(\vec{r}')e^{-i\varepsilon_i^{N-1}\tau/\hbar}\theta(-\tau), \tag{C.19}$$

where the sum runs over the ground state and excited states of the $N-1$- and $N+1$-particle system, respectively. Equation (C.19) thus states that after an addition of an electron, equivalent with $\tau > 0$, the state can be represented by a linear combination of excited states:

$$\hat{\psi}^\dagger(\vec{r}')\left|\Psi_0^N\right\rangle = \sum_i \psi_i^{N+1*}(\vec{r}')\left|\Psi_0^{N+1}\right\rangle,$$

where the case for hole propagation is analogous. Transforming into the frequency domain with the Fourier transform of the Heavyside step function given by

$$\theta(\omega) = \frac{1}{2\pi}\int_{-\infty}^{\infty}\theta(\tau)e^{i\omega\tau-\eta|\tau|}d\tau = \frac{i}{2\pi(\omega+i\eta)}$$

enables the so-called Lehmann representation of the Green function as

$$G(\vec{r},\vec{r}';\omega) = \sum_i \frac{\psi_i^{N+1}(\vec{r})\psi_i^{N+1*}(\vec{r})}{\hbar\omega-\varepsilon_i^{N+1}+i\eta} + \sum_i \frac{\psi_i^{N-1}(\vec{r})\psi_i^{N+1*}(\vec{r})}{\hbar\omega-\varepsilon_i^{N-1}-i\eta} \tag{C.20}$$

but in order not to overload the notation the $N\pm1$ superscripts are droped from now on.
It can be shown that the time-ordered Green function of the interacting system obeys an integral equation also known as the Dyson equation, which is given by

$$G(\vec{r},\vec{r}';\omega) = G_0(\vec{r},\vec{r}';\omega) + \iint G_0(\vec{r},\vec{r}'';\omega)\Sigma(\vec{r}'',\vec{r}''';\omega)G(\vec{r}''',\vec{r}';\omega)d\vec{r}''d\vec{r}''', \tag{C.21}$$

where $G_0(\vec{r},\vec{r}';\omega)$ is the Green function of a mean-field system defined by

$$\hat{h}_0\phi_i^0 = \varepsilon_i^0\phi_i^0, \tag{C.22}$$

with the single-electron Hamiltonian given as

$$\hat{h}_0 = -\frac{\hbar^2}{2m}\nabla^2 + V_{ext}(\vec{r}) + \frac{e^2}{4\pi\varepsilon_0}\int\frac{p(\vec{r}')}{|\vec{r}-\vec{r}'|}d\vec{r}'.$$

By solving equation (C.22) $G_0(\vec{r},\vec{r}';\omega)$ is obtained through equation (C.20). $\Sigma(\vec{r},\vec{r}';\omega)$ is the non-Hermitian and non-local self-energy operator, which contains the contribution from the many-body exchange and correlation energy. Equation (C.21) can, however, be reformulated from which this can easier be seen. By substituting equation (C.20) into the Green function of a stationary state yields

$$\left[\hbar\omega-\hat{h}_0\right]G(\vec{r},\vec{r}',\omega) - \int\Sigma(\vec{r},\vec{r}'';\omega)G(\vec{r}'',\vec{r}',\omega)d\vec{r}'' = \delta(\vec{r}-\vec{r}')$$

$$\Downarrow$$

$$\sum_i \frac{\psi_i^*(\vec{r}')}{\hbar\omega-\varepsilon_i\mp i\eta}\left(\left[\hbar\omega-\hat{h}_0\right]\psi_i(\vec{r}) - \int\Sigma(\vec{r},\vec{r}'';\omega)\psi_i(\vec{r}'')d\vec{r}''\right) = \delta(\vec{r}-\vec{r}')$$

If it is assumed that the system is non-degenerated and multiplying the equation with $\hbar\omega - \varepsilon_j$ followed by taking the limit $\omega \to \varepsilon_j/\hbar$ gives rise to

$$\lim_{\omega\to\varepsilon_j/\hbar}(\hbar\omega-\varepsilon_j)\sum_i \frac{\psi_i^*(\vec{r}')}{\hbar\omega-\varepsilon_i+i\eta}\left[\hbar\omega-\hat{h}_0\right]\psi_i(\vec{r}) - \int \Sigma(\vec{r},\vec{r}'';\omega)\psi_i(\vec{r}'')d\vec{r}'' = \lim_{\omega\to\varepsilon_j/\hbar}(\hbar\omega-\varepsilon_j)\delta(\vec{r}-\vec{r}')$$

$$\Downarrow$$

$$\psi_j^*(\vec{r}')\left(\left[\varepsilon_j-\hat{h}_0\right]\psi_j(\vec{r}) - \int \Sigma(\vec{r},\vec{r}'';\varepsilon_j/\hbar)\psi_j(\vec{r}'')d\vec{r}''\right) = 0$$

and because $\psi(\vec{r}')$ does not equal zero for all $\vec{r}'$ the parenthesis must be zero, which yields the following quasiparticle equation:

$$\hat{h}_0\psi_j(\vec{r}) - \int \Sigma(\vec{r},\vec{r}'';\varepsilon_j/\hbar)\psi_j(\vec{r}'')d\vec{r}'' = \varepsilon_j\psi_j(\vec{r}), \tag{C.23}$$

which is seen to be nonlinear in ε_j. Even though a non-degenerate system was assumed in order derive equation (C.23) it still holds for degenerate systems because if the solution to equation (C.23) leads to degenerated states $\psi_j(r)$ and energies ε_j an arbitrary perturbation can be introduced which breaks the symmetry in such a way that the degeneracy is lifted[10]. The validity of equation (C.23) for the degenerated system is thus established by taking the limit for which the perturbation going to zero.

Although equation (C.23) seems quite similar to a single particle equation, it is not a mean-field formulation because of the self-energy which takes all dynamic many-electron effects into account. Therefore, one can not interpret the functions $\psi_i(\vec{r})$ and energies ε_i as single-particle quantities but as properties of the many-electron system. Furthermore, due to the nonlinearity of equation (C.23) it follows that the $\psi_i(\vec{r})$s are not orthonormal, in contrast to single-particle functions but they do obey the closure relation.

In order to the solve equation (C.23) appropriate approximations must be used. Adapting the GW approximation enables the electron exchange and a large part of the electron correlation to be computed by approximating the self-energy to

$$\Sigma^{GW}(\vec{r},\vec{r}'';\tau) = i\hbar G_0(\vec{r},\vec{r}';\tau)W(\vec{r},\vec{r}';\tau+\eta), \tag{C.24}$$

which in frequency domain is given as

$$\Sigma^{GW}(\vec{r},\vec{r}';\omega) = \frac{i\hbar}{2\pi}\int_{-\infty}^{\infty} G_0(\vec{r},\vec{r}';\omega+\omega')W(\vec{r},\vec{r}';\omega')e^{i\omega'\eta}d\omega'. \tag{C.25}$$

$W(\vec{r},\vec{r}';\omega)$ represent the dynamically screened interaction from which one can relate to the bare Coulomb potential $v(\vec{r},\vec{r}') = \frac{e^2}{4\pi\varepsilon|\vec{r}-\vec{r}'|}$ through

$$W(\vec{r},\vec{r}';\omega) = \int \frac{1}{\varepsilon(\vec{r},\vec{r}'';\omega)}v(\vec{r},\vec{r}'')d\vec{r}'' = v(\vec{r},\vec{r}') + \int n_{ind}(\vec{r},\vec{r}'';\omega)v(\vec{r}'',\vec{r}')d\vec{r}''. \tag{C.26}$$

[10] This can e.g. be done by the means of an additional external potential in $\hat{h}_0$

Because electrons repel other electrons nearby an exchange correlation hole is created with the effective positive charge $n_{ind}(\vec{r},\vec{r}'';\omega)$, which screens the bare Coulomb potential $v(\vec{r},\vec{r}')$. This is illustrated on figure C.1. Likewise, the bare Coulomb potential will be screened by an effective negative charge.
Within the GW approximation the random-phase approximation (RPA) is applied from which the dielectric and polarisation functions can be shown to be

$$\begin{aligned}\varepsilon(\vec{r},\vec{r}';\omega) &= \delta(\vec{r}-\vec{r}') - \int v(\vec{r},\vec{r}'')P(\vec{r}'',\vec{r}';\omega)d\vec{r}'',\\ P(\vec{r},\vec{r}';\tau) &= -i\hbar G_0(\vec{r},\vec{r}';\tau)G_0(\vec{r}',\vec{r};-\tau)\end{aligned} \tag{C.27}$$

By the use of equation (C.20) the polarisation function can be rewritten to

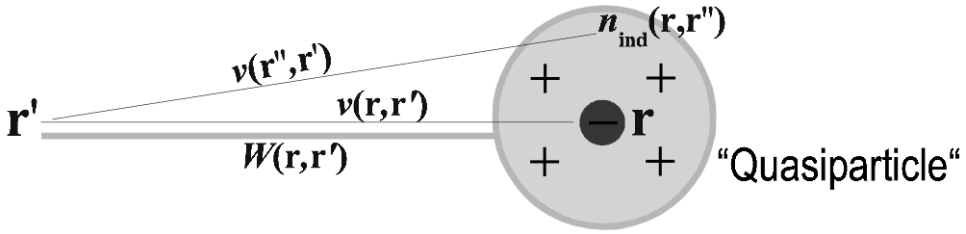

Figure C.1: The formation of a Coulomb hole around an electron placed at $\vec{r}$, which screens the electrons bare potential leading to the definition of $W(\vec{r},\vec{r}')$ that takes into account the combined potentials of the bare electron and its screened cloud n_{ind}. The word quasiparticle refer to the ensemble consisting of the electron and its polarisation cloud. [Friedrich and Schindlmayr, 2006]

$$P(\vec{r},\vec{r}';\omega) = \sum_{i}^{\text{occ.}}\sum_{j}^{\text{unocc.}} \varphi_i^0(\vec{r})\varphi_i^{0*}(\vec{r})\varphi_i^{0*}(\vec{r}')\varphi_i^0(\vec{r}')\left(\frac{1}{\hbar\omega+\varepsilon_i^0-\varepsilon_j^0+i\eta}-\frac{1}{\hbar\omega-\varepsilon_i^0+\varepsilon_j^0+i\eta}\right) \tag{C.28}$$

in terms of wave functions $\varphi_i^0(\vec{r})$ and energies ε_i^0.
[Novotny and Hecht, 2006; Friedrich and Schindlmayr, 2006]

C.4.1 Numerical implementation for band structure calculations

When doing band structure calculations it is more efficient to use the ε_is from equation (C.23) rather than equation (C.21) and search for the poles of the Green function. To do this, it is possible to use the Kohn-Sham equations because in many cases the Kohn-Sham eigenvalues ε_i^{KS} provide a reasonable estimate to the band structure and likewise the Kohn-Sham wave functions will provide an estimate for the quasiparticle wave functions. Therefore, with $V_{xc}(\vec{r})$ as the local exchange-correlation potential in the Kohn-Sham system the self-energy correction $\Sigma(\vec{r},\vec{r}';\varepsilon_i/\hbar)-V_{xc}(\vec{r})\delta(\vec{r}-\vec{r}')$ is small, enabling a first-order perturbation approach to obtain approximate energies as

$$\varepsilon_i \approx \varepsilon_i^{KS} + \langle\varphi_i^{KS}|\Sigma(\vec{r},\vec{r}';\varepsilon_i/\hbar)-V_{xc}|\varphi_i^{KS}\rangle.$$

In order to solve this equation information about the self-energy in the frequency domain is needed but this is generally not known leading to the following first-order expansion:

$$\Sigma(\vec{r},\vec{r}';\varepsilon_i/\hbar) \approx \Sigma(\vec{r},\vec{r}';\varepsilon_i^{KS}/\hbar) + \frac{\varepsilon_i - \varepsilon_i^{KS}}{\hbar}\frac{\partial\Sigma(\vec{r},\vec{r}';\varepsilon_i^{KS}/\hbar)}{\partial\omega},$$

which gives rise to

$$\varepsilon_i \approx \varepsilon_i^{KS} + Z_i\langle\varphi_i^{KS}|\Sigma(\vec{r},\vec{r}';\varepsilon_i^{KS}/\hbar) - V_{xc}|\varphi_i^{KS}\rangle, \tag{C.29}$$

where Z_i is a quasiparticle renormalisation factor given as

$$Z_i = \left(1 - \left\langle\varphi_i^{KS}\left|\frac{1}{\hbar}\frac{\partial\Sigma(\vec{r},\vec{r}';\varepsilon_i^{KS}/\hbar)}{\partial\omega}\right|\varphi_i^{KS}\right\rangle\right)^{-1}. \tag{C.30}$$

W can be decomposed into a bare Coulomb interaction v and the remainder $W - v$. Equation (C.24) then splits into an exchange part and a correlation part, symbolically written as

$$\Sigma^{GW} = i\hbar G_0^{KS} W = i\hbar G_0^{KS} v + i\hbar G_0^{KS}(W - v) = \Sigma_x^{GW} + \Sigma_c^{GW},$$

where G_0^{KS} has been used instead of G_0. The self-energy in the frequency domain then splits into

$$\Sigma_x^{GW}(\vec{r},\vec{r}';\omega) = \frac{i\hbar}{2\pi}\int_{-\infty}^{\infty} G_0^{KS}(\vec{r},\vec{r}';\omega+\omega')v(\vec{r},\vec{r}')e^{i\omega'\eta}d\omega' \tag{C.31}$$

and

$$\Sigma_c^{GW}(\vec{r},\vec{r}';\omega) = \frac{i\hbar}{2\pi}\int_{-\infty}^{\infty} G_0^{KS}(\vec{r},\vec{r}';\omega+\omega')\left[W(\vec{r},\vec{r}';\omega') - v(\vec{r},\vec{r}')\right]d\omega'. \tag{C.32}$$

The integral in equation (C.31) can be done analytically and leads to the well-known Hartree-Fock expression for the exchange:

$$\left\langle\varphi_j^{KS}\left|\Sigma_x^{GW}\right|\varphi_j^{KS}\right\rangle = -\frac{e^2}{4\pi\varepsilon_0}\sum_j^{occ.}\int\frac{\varphi_j^{KS*}(\vec{r})\varphi_j^{KS}(\vec{r})\varphi_j^{KS*}(\vec{r}')\varphi_j^{KS}(\vec{r}')}{|\vec{r}'-\vec{r}|}d\vec{r}d\vec{r}', \tag{C.33}$$

whereas equation (C.32) must be computed numerically.
With $\{\xi_\alpha(\vec{r})\}$ as a basis for the Kohn-Sham wave functions the polarisation function can be written as

$$P(\vec{r},\vec{r}';\omega) = \sum_{\mu,\nu} P_{\mu\nu}(\omega)\chi_\mu^*(\vec{r})\chi_\mu(\vec{r}'),$$

where $\chi_\mu = \xi_\alpha^*(\vec{r})\xi_\beta(\vec{r})$ with the composite index $\mu = (\alpha,\beta)$. Equation (C.24),(C.25), (C.26) and (C.27) are then solved by the following operations:

1. A self-consistent DFT loop to obtain the Kohn-Sham wave functions and energies. It is now possible to calculate equation (C.33).
2. The polarisation matrix $P_{\mu\nu}(\omega)$ is calculated from equation (C.28).

3. The dielectric matrix is obtained according to $\varepsilon_{\mu\nu} = \delta_{\mu\nu} - \sum_{\gamma} v_{\mu\gamma} P_{\mu\gamma}(\omega)$ and inverted.
4. One can now calculate the screened interaction $W_{\mu\nu} = \sum_{\gamma} \varepsilon^{-1}_{\mu\gamma}(\omega) v_{\gamma\nu}$ by a matrix multiplication of the inverse dielectric function and the Coulomb matrix.
5. The correlation term $\left\langle \varphi_i^{KS} \left| \Sigma_c^{GW} \right| \varphi_i^{KS} \right\rangle$ is computed using equation (C.33).
6. Now, the approximate quasiparticle energies is evaluated according to equation (C.29) and (C.30).

It is very time consuming to compute the dielectric function, its inversion and the correlation part of the self-energy. The inverse dielectric function is, therefore, sometimes approximated by a so-called plasmon-mode model. These models replace the imaginary component of $\varepsilon^{-1}(\omega)$, which has a peaked structure, by a sum of delta functions at the corresponding frequencies. This enables a reduction of the third step to a single matrix inversion of the static dielectric function, from which $\omega = 0$, and an analytic evaluation of the frequency integral.

[Friedrich and Schindlmayr, 2006]

Computational method for solving the electronic problem

D

There are many different approaches for solving the electronic problem in practice so throughout this appendix the theoretical foundation for the DFT approach, used to evaluate the electronic dispersions, will be presented.
Throughout this appendix Kohanoff [2006] will be used as reference.

D.1 Pseudopotential method

The main contribution to the electronic energies comes from the electron-nuclear interaction, which can be attended in a number of ways. An approach that has been proven quite accurate when considering the valence electrons without being too computationally demanding is the so-called pseudopotential method.
Because the inner core electrons do not participate in chemical bonding one can eliminate the corresponding degrees of freedom by replacing the atomic nuclei with a still, point-like, effective nucleus charge, which takes the screening of the core electrons into account. The bare Coulomb potential for the nuclei is then replaced by a screened Coulomb potential that takes into account the orthogonalisation of the valence and core states of the same angular momentum, producing valence wave functions with the required number of nodes.
Another approach is to assume that the valence wave functions inside the core region are irrelevant, if the main interest is the chemical bonding properties. In those cases the wave function inside the core radius is replaced by a smooth node less pseudo-wave function and therefore not an orbital representing the original atomic orbital. It is thus possible to construct a smooth valence wave function $\tilde{\varphi}_v$ that is not orthogonalised to the core state φ_c by combining the true valence state and core state as

$$|\tilde{\varphi}_v\rangle = |\varphi_v\rangle + \sum_c a_{cv}|\varphi_c\rangle$$

where $a_{cv} = \langle\varphi_c|\tilde{\varphi}_v\rangle \neq 0$. The pseudo-wave function satisfies the following modified Schrödinger equation:

$$\left(\hat{H} + \sum_c (\varepsilon_v - \varepsilon_c)|\varphi_c\rangle\langle\varphi_c|\right)|\tilde{\varphi}_v\rangle = \varepsilon_v|\tilde{\varphi}_v\rangle,$$

with $\hat{H} = \hat{T} + \hat{V}$ and $\hat{V} = \frac{Z_c}{r}\hat{I}$ as the nucleus potential and $\hat{I}$ as the identity operator. It is thus possible to construct a pseudo-Hamiltonian by the means of the eigenvalues of the original Hamiltonian but with a smooth, node less wave function:

$$\hat{H}_{PS} = \hat{H} + \sum_c (\varepsilon_v - \varepsilon_c)|\varphi_c\rangle\langle\varphi_c|,$$

with the associated so-called pseudopotential

$$\hat{V}_{PS} = \frac{Z_c}{r}\hat{I} + \sum_c (\varepsilon_v - \varepsilon_c)|\varphi_c\rangle\langle\varphi_c|.$$

D.1.1 Troullier-Martin pseudopotentials

Some of the smoothest norm-conserving pseudopotentials are those created by the recipe of Troullier and Martin (TM), who made an intense study of the convergence properties of the plane wave expansion (PW), of the pseudopotential, with the PW expansion explained in the section below. They proposed the following analytic form of the wave function inside the cutoff radius with respect to the core:

$$R^l_{TM} = r^l \mathrm{e}^{p(r)},$$

where $p(r) = c_0 + \sum_{i=2}^{n} c_i r^i$ and the behaviour of r^l for small r is included in order to avoid a hard-core pseudopotential with a singularity at the origin, demanding a large number of PWs for a sufficient basis. In their work they realised that the asymptotic, large wave number behaviour of the pseudopotential was influenced by the odd derivatives at the origin, which implied that a large degree of smoothness can be obtained by setting all of the odd coefficients in the polynomial to zero. Also they found that the smoothest pseudopotentials are flat at the origin. They chose a sixth order polynomial in r^2

$$p(r) = c_0 + c_2 r^2 + c_4 r^4 + c_6 r^6 + c_8 r^8 + c_{10} r^{10} + c_{12} r^{12},$$

where the coefficients are determined by norm-conservation of the charge within the cutoff radius r_c, continuity of the pseudo-wave function and its four derivatives at r_c, and demanding zero curvature of the pseudopotential at the origin.

D.2 Plane wave expansion

When attending solids Bloch's theorem is often applied, which states that the wave functions must be composed of a phase factor and a periodic function $u_{\vec{k}}(\vec{r})$ that satisfies $u_{\vec{k}}(\vec{r}) = u_{\vec{k}}(\vec{r} + \vec{a}_i)$, with $\vec{a}_i$ as any lattice vector. Inspired by the solutions of the Schrödinger equation for free electrons plane waves can

be used as basis functions but because the external potential is far from constant around the atomic sites the solution to the Schrödinger equations is no longer a single PW but a linear combination of PWs.
It is given, that the periodic function in real space can be written as the Fourier transform of a function in reciprocal space:

$$u_{\vec{k}}(\vec{r}) = \int \tilde{u}_{\vec{k}}(\vec{g}) e^{i\vec{g}\cdot\vec{r}} d\vec{g}.$$

From the periodicity it is required that $e^{i\vec{g}\cdot\vec{a}_j} = 1$ leading to $\vec{g}\cdot\vec{a}_j = n2\pi$, with j referring to one of the lattice vectors and n as an integer. The $\vec{g}$ vector can thus be written as $\vec{g} = n_1\vec{b}_1 + n_2\vec{b}_2 + n_3\vec{b}_3$, with $n_{1,2,3}$ as integers and

$$\vec{b}_i = 2\pi\frac{\vec{a}_j \times \vec{a}_k}{\Omega}, \tag{D.1}$$

with Ω as the volume of the supercell[1]. The $\vec{g}$ vectors are thus restricted to the reciprocal lattice vectors obtained by equation (D.1). The wave function can, due to the periodicity be expressed by the following Fourier series

$$\varphi^{(\vec{k})}(\vec{r}) = \frac{e^{i\vec{k}\cdot\vec{r}}}{\sqrt{\Omega}} \sum_{G=0}^{\infty} C_{\vec{k}}(\vec{G}) e^{i\vec{G}\cdot\vec{r}}$$

and the PW basis is now defined as

$$\phi_{\vec{G}}(\vec{r}) = \frac{1}{\sqrt{\Omega}} e^{i\vec{G}\cdot\vec{r}},$$

that is normalised to the supercell

$$\langle\phi_{\vec{G}}|\phi'_{\vec{G}}\rangle = \frac{1}{\Omega}\int_{\Omega} e^{i(\vec{G}-\vec{G}')\cdot\vec{r}} = \frac{1}{\Omega}(\Omega\delta_{\vec{G},\vec{G}'}) = \delta_{\vec{G},\vec{G}'}.$$

The different wave vectors thus corresponds to PWs while the wave functions can be written as

$$\varphi_j^{(\vec{k})}(\vec{r}) = e^{i\vec{k}\cdot\vec{r}} \sum_{\vec{G}=0}^{\infty} C_{j,\vec{k}}(\vec{G})\phi_{\vec{G}}(\vec{r})$$

or equivalently

$$\varphi_j^{(\vec{k})}(\vec{r}) = \sum_{\vec{G}=0}^{\infty} C_{j,\vec{k}}(\vec{G})\phi_{\vec{G}}^{\vec{k}}(\vec{r}),$$

with

$$\phi_{\vec{G}}^{\vec{k}}(\vec{r}) = \frac{1}{\sqrt{\Omega}} e^{i(\vec{G}+\vec{k})\cdot\vec{r}}$$

for the different eigenstates j while the PW coefficients take the form

$$C_{j,\vec{k}}(\vec{G}) = \int_{\Omega} \phi_{\vec{G}}^{\vec{k}*}(\vec{r})\varphi_j^{(\vec{k})}(\vec{r})d\vec{r} = \frac{1}{\sqrt{\Omega}}\int_{\Omega} e^{-i(\vec{G}+\vec{k})\cdot\vec{r}}\varphi_j^{(\vec{k})}(\vec{r})d\vec{r}.$$

[1] The supercell is a volume element, which represents the entire solid. The solid is thus build by infinitely many supercells.

One of the advantages of using the PW approach is that the Schrödinger equation can be rewritten to a rather simple and appealing eigenvalue problem. Firstly, the overlap integrals is, due to the orthogonality of the PWs, given as

$$S^{\vec{k}}_{\vec{G},\vec{G}'} = \delta_{\vec{G},\vec{G}'},$$

while the kinetic and potential contributions to the Hamiltonian matrix elements are given

$$T^{\vec{k}}_{\vec{G},\vec{G}'} = -\frac{\hbar^2}{2m}\langle\phi^{\vec{k}}_{\vec{G}}|\nabla^2|\phi^{\vec{k}}_{\vec{G}'}\rangle = \frac{\hbar^2}{2m}|\vec{k}+\vec{G}|^2\delta_{\vec{G},\vec{G}'},$$

and

$$V_{\vec{G},\vec{G}'} = \langle\phi^{\vec{k}}_{\vec{G}}|\hat{V}|\phi^{\vec{k}}_{\vec{G}'}\rangle = \frac{1}{\sqrt{\Omega}}\int_{\Omega} V(\vec{r})\mathrm{e}^{-i(\vec{G}-\vec{G}')\cdot\vec{r}}d\vec{r} = \tilde{V}(\vec{G}-\vec{G}'),$$

respectively. Using a PW basis set thereby enables the time-independent Schrödinger equation to be written as the following eigenvalue equation:

$$\sum_{\vec{G}'}\left(\frac{\hbar^2}{2m}|\vec{k}+\vec{G}|^2\delta_{\vec{G},\vec{G}'} + \tilde{V}(\vec{G}-\vec{G}')\right)C_{j,\vec{k}}(\vec{G}') = \varepsilon_{j,\vec{G}'}C_{j,\vec{k}}(\vec{G}). \tag{D.2}$$

D.2.1 PW energy cutoff

When solving the electronic problem in practice by the means of PW basis sets the sum in equation (D.2) is in principle infinitely many $\vec{G}$ vectors leading to wave functions of infinite accuracy which obviously is not doable. Therefore, in practice, this sum has to be limited to a finite number of terms in accordance to the precision of interest. The contribution from the Fourier coefficients to the wave functions decreases for increasing $|\vec{k}+\vec{G}|$, hence the PW expansion can be truncated by only allowing waves with a kinetic energy lower than some energy cutoff given by

$$E_{cut} > \frac{\hbar^2}{2m}|\vec{k}+\vec{G}|^2.$$

Because large $\vec{G}$ vectors are associated with small features in real space the restricting of the reciprocal space leads to a short scale restriction in real space. The cutoff energy is thereby determined from the pseudopotentials and the system geometry.

Computational procedure for solving the electronic problem

E

This appendix displays the computation procedure done with the ABINIT code to calculate the Kohn-Sham band structure of the polymers. This investigation is based on the plane wave expansion combined with the LDA Troullier-Martin pseudopotentials for hydrogen, carbon and oxygen.

E.1 PPP and PFO

The first thing done was to generate an initial guess for molecular structure which was done by the program Avogadro, followed by a convergence test of the cutoff energy with ABINIT. The convergence test was done by placing the PPP molecule in a $9\times20\times20$ Å^3 box and the PFO molecule in a $9\times20\times20$ Å^3 box with the backbone of the polymers placed along x-axis for which the box is 9 Å long. The total energy as a function cutoff energy for PPP and PFO is shown on figure E.1a) and E.1b), respectively. As a compromise between computation time and precision the cutoff energy for both polymers was chosen to 33 Ha. The molecular structure was then set to relax until the force on an atom did not differ more the

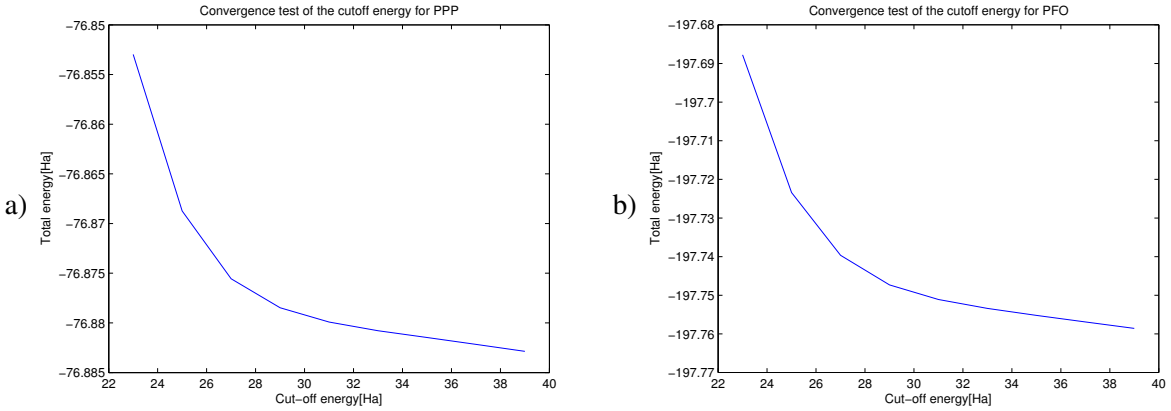

Figure E.1: The total energy versus cutoff energy for a) PPP and b) PFO.

$5{\cdot}10^{-5}$ Ha/Bohr, yielding the structure shown on figure 2.8 on page 12 for PPP and figure 2.9 on page 12 for PFO. Furthermore, the lattice constant for PPP was found to be l=8.6 Å and l=8.36 Å PFO.
With the relaxed structure, the Kohn-Sham structure could be computed. In order to verify that the

polymer did not couple to neighbouring polymers the Kohn-Sham structure was calculated along the k_y and k_z, as shown on figure E.2 for PPP and E.3 for PFO. It appears, from the figures, that the bands are completely flat and thereby no interchain coupling. This step was needed because the ABINIT is designed for three dimensional structures.

a) b)

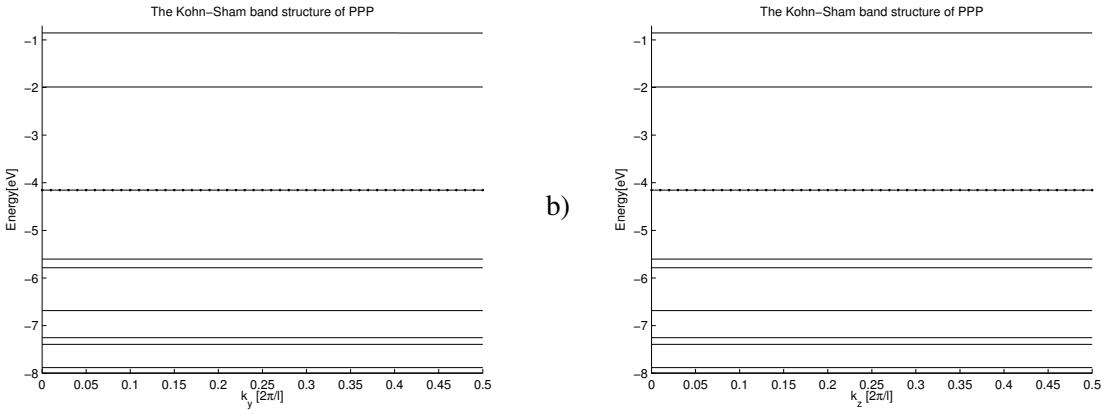

Figure E.2: The energy versus k_y a) and k_y b) for PPP with the dotted line as the Fermi level.

a) b)

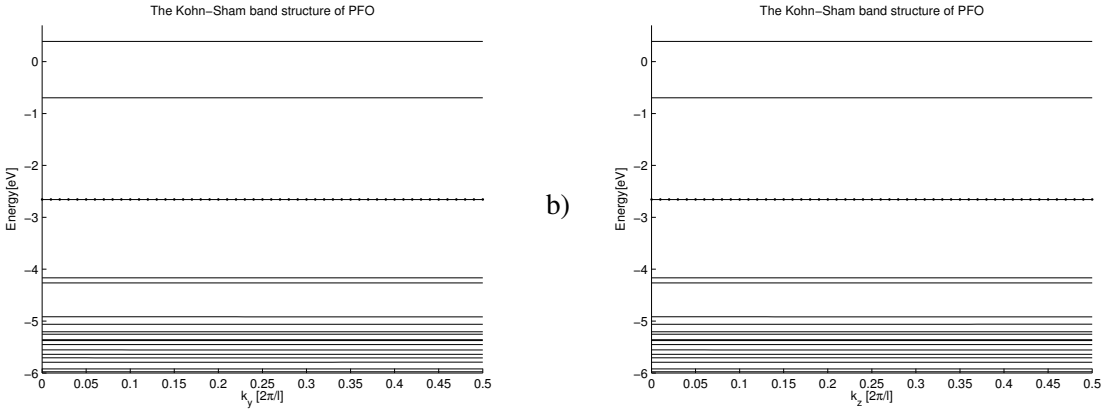

Figure E.3: The energy versus k_y a) and k_y b) for PFO with the dotted line as the Fermi level.

E.2 PPV and MEH-PPV

The molecular structures generated from Avogrado was also placed in a $9\times20\times20$ Å^3 box each in order to determine an appropriate cutoff energy. The total energy as a function of cutoff energy for PPV and MEH-PPV is shown on figure E.4a) and E.4b), respectively, from which the cutoff energy for PPV was set to 33 Ha for PPV and 38 Ha for MEH-PPV.

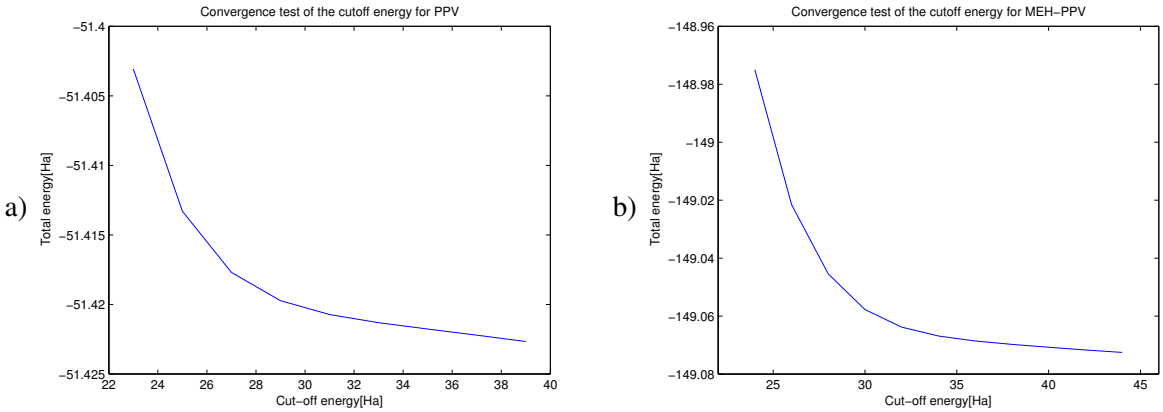

Figure E.4: The total energy versus cutoff energy for a) PPV and b) MEH-PPV.

The structures was then relaxed until the maximum difference in forces acting on an atom did not differ more than $5 \cdot 10^{-5}$ Ha/Bohr yielding the structure shown on figure 2.12 for PPV and figure 2.13 for MEH-PPV. Furthermore, the lattice constant for PPV was found to be l=6,62 Å and l=6,63 Å MEH-PPV.
The bands along k_y and k_z are shown on figure E.5 for PPV and E.6 for MEH-PPV showing no interchain coupling.

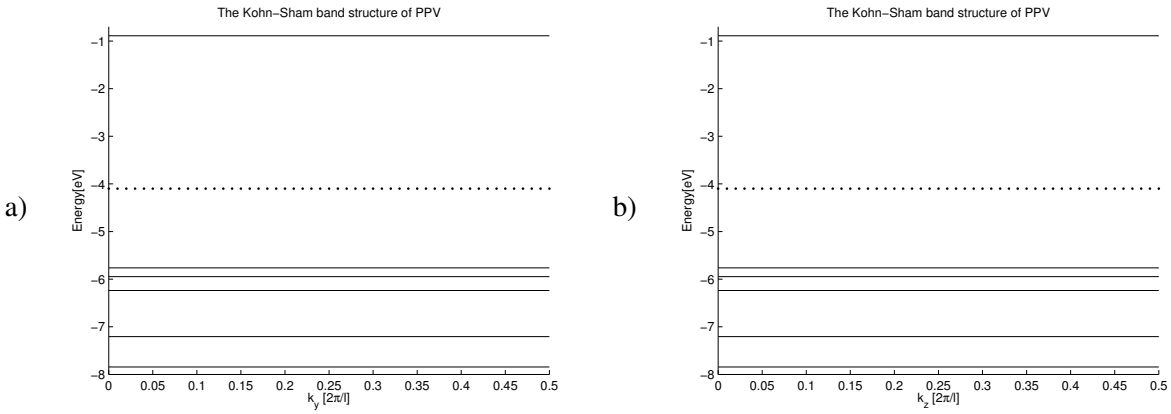

Figure E.5: The energy versus k_y a) and k_y b) for PPV with the dotted line as the Fermi level.

a)

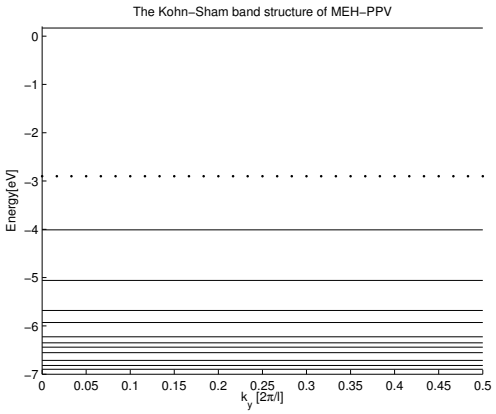

b)

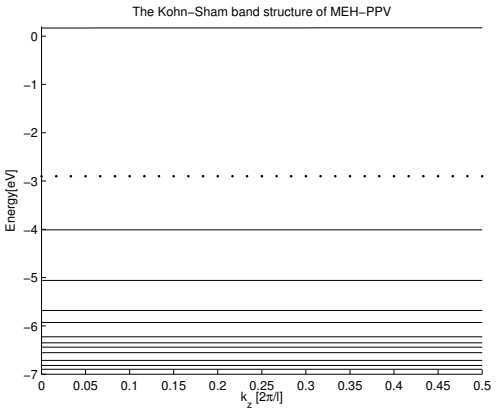

Figure E.6: The energy versus k_y a) and k_y b) for MEH-PPV with the dotted line as the Fermi level.

Production parameters

F

In the table below the layer structure for the fabricated OLEDs is displayed.

Structure / Sample no.	EBL/HTL	Emitting layer	HBL/ETL	Contact materials	Capping layer	Comment
1	PEDOT:PSS	PFO	N/A	Al	N/A	
2	PEDOT:PSS	MEH-PPV	N/A	Al	N/A	
3	PEDOT:PSS	PFO	Alq_3	LiF/Mg/Al	N/A	
4	PEDOT:PSS	MEH-PPV	Alq_3	LiF/Mg/Al	N/A	
5	PEDOT:PSS	PFO	Alq_3	LiF/Mg/Al	N/A	
6	PEDOT:PSS	PFO	Alq_3	LiF/Mg/Al	N/A	Contact dep. after 48 hours
7	TPD	PFO	Alq_3	LiF/Mg/Al	N/A	1.3mg/ml TPD spun at 500 RPM
8	TPD	PFO	Alq_3	LiF/Mg/Al	N/A	4mg/ml TPD spun at 1000 RPM
9	TPD	PFO	Alq_3	LiF/Mg/Al	N/A	4mg/ml TPD spun at 2000 RPM
10	TPD	PFO	Alq_3	LiF/Mg/Al	75 nm LiF	
11	TPD	PFO	Alq_3	LiF/Mg/Al	75 nm LiF	Degradation in N_2
12	TPD	PFO	Alq_3	LiF/Mg/Al	150 nm LiF	
13	TPD	PFO	Alq_3	LiF/Mg/Al	300 nm LiF	
14	TPD	PFO	Alq_3	LiF/Mg/Al	150 nm LiF	Spun under clean room conditions
15	TPD	MEH-PPV	Alq_3	LiF/Mg/Al	N/A	Spun MEH-PPV 4 times at 2000 RPM
16	TPD	MEH-PPV	Alq_3	LiF/Mg/Al	N/A	Spun MEH-PPV 6 times at 3000 RPM
17	TPD	MEH-PPV	Alq_3	LiF/Mg/Al	N/A	Spun MEH-PPV 6 times at 4000 RPM
18	TPD	MEH-PPV	Alq_3	LiF/Mg/Al	75 nm LiF	
19	TPD	MEH-PPV	Alq_3	LiF/Mg/Al	150 nm LiF	
20	TPD	MEH-PPV	Alq_3	LiF/Mg/Al	300 nm LiF	
21	TPD	MEH-PPV	Alq_3	LiF/Mg/Al	150 nm LiF	Spun under clean room conditions

Table F.1: Production parameters of the fabricated devices.